Stockholm University

Dissecting Supernovae through the Modeling of Nebular-Phase Spectra

Stan Barmentloo

Doctoral Thesis in Astronomy at Stockholm University, Sweden 2026

Dissecting Supernovae through the Modeling of Nebular-Phase Spectra

Stan Barmentloo

Academic dissertation for the Degree of Doctor of Philosophy in Astronomy at Stockholm University to be publicly defended on Tuesday 17 November 2026 at 10.00 in Lärosal 17, hus 2, Albano, Albano, Greta Arwidssons väg 8, 10.

Abstract

Core-collapse supernovae (CCSNe) are the explosive deaths of the most massive (with a Zero-Age Main Sequence mass above eight solar masses) stars. During these violent events the stars eject the elements which they synthesised during their lives via nuclear fusion. This way, they provide the majority of the metals present in the universe today. This makes studying CCSNe and consequently the stars that lead up to them of great interest.

The overwhelming majority of SNe occur too far away to detect their progenitors: as of today, there only exists direct progenitor images for a few dozen red supergiants (RSGs), the progenitors of hydrogen-rich Type II SNe. Images of yellow- and blue supergiants (YSGs/BSGs), which lead to stripped envelope SNe (SESNe) of the hydrogen-poor Types Ib, Ic and IIb, are much more rare, with only a handful confirmed progenitors to date. Learning about the progenitor stars of SESNe is thus most effectively done by studying the SNe themselves.

SN explosions are followed by a burst of light which lasts for a few years. Spectral observations during the nebular phase, the period of the SN when the ejecta have become mostly transparent to radiation all the way down to the core, provide an excellent opportunity to study the elements in the ejecta. From the luminosities of individual spectral lines, information on the synthesised masses of individual elements, as well as on the total mass of the progenitor star, can be obtained.

The main goal of this thesis is to provide novel methodologies to analyse these nebular phase spectra in greater detail. To do so, a main component is the modeling of synthetic nebular phase spectra based on ejecta models. These models inform us on the relevant physical conditions in the ejecta at a given epoch, necessary for proper interpretation of spectral line luminosities. In Paper I the diagnostic potential of a nebular nitrogen line seen in SESNe is investigated, and it is shown that this line, under specific conditions, directly probes the mass of the SN progenitor. Paper II instead focuses on two emission lines of carbon. A Monte Carlo radiative transfer code is developed to properly extract their luminosities, and it is shown that spectral models overproduce the strength of these lines when compared to a sample of SNe, suggesting too much carbon is produced in current stellar evolution models. Finally, Paper III provides a framework for analysing nebular-phase spectra from the James Webb Space Telescope (JWST). By applying this framework to observations of Type Ic SN 2024aecx, it is shown that a single JWST spectrum allows for estimation of elemental masses of Cl, Ar, Ni and Fe. The mass of Cl found in Type Ic SN 2024aecx decisively indicates that SNe are the main production sites of the intermediate odd-Z elements, but that ingredients are missing in stellar evolution modeling to reproduce the observed abundances. Furthermore, it is found that the Ni-bubble effect, an uncertain parameter in SN spectral modeling, for this SN is a lot weaker than typically assumed.

Keywords: *supernovae, radiative transfer, line formation, transients, stellar evolution, nucleosynthesis.*

Stockholm 2026
http://urn.kb.se/resolve?urn=urn:nbn:se:su:diva-259612

ISBN 978-91-8107-735-3
ISBN 978-91-8107-736-0

Department of Astronomy

Stockholm University, 106 91 Stockholm

DISSECTING SUPERNOVAE THROUGH THE MODELING OF NEBULAR-PHASE SPECTRA

Stan Barmentloo

Stockholm
University

Dissecting Supernovae through the Modeling of Nebular-Phase Spectra

Stan Barmentloo

©Stan Barmentloo, Stockholm University 2026

ISBN print 978-91-8107-735-3
ISBN PDF 978-91-8107-736-0

Cover image: Holy Roman Emperor Henry III pointing at a new star in the sky, likely SN 1054. Image credits: Bibliotheca Palatina - Digital, Cod. Pal. germ. 149

Printed in Sweden by Universitetsservice US-AB, Stockholm 2026

Abstract

Core-collapse supernovae (CCSNe) are the explosive deaths of the most massive ($M_{\rm ZAMS} \gtrsim 8\ M_{\odot}$) stars. During these violent events the stars eject the elements which they synthesised during their lives via nuclear fusion. This way, they provide the majority of the metals present in the universe today. This makes studying CCSNe and consequently the stars that lead up to them of great interest.

The overwhelming majority of SNe occur too far away to detect their progenitors: as of today, there only exists direct progenitor images for a few dozen red supergiants (RSGs), the progenitors of hydrogen-rich Type II SNe. Images of yellow- and blue supergiants (YSGs/BSGs), which lead to stripped envelope SNe (SESNe) of the hydrogen-poor Types Ib, Ic and IIb, are much more rare, with only a handful confirmed progenitors to date. Learning about the progenitor stars of SESNe is thus most effectively done by studying the SNe themselves.

SN explosions are followed by a burst of light which lasts for a few years. Spectral observations during the nebular phase, the period of the SN when the ejecta have become mostly transparent to radiation all the way down to the core, provide an excellent opportunity to study the elements in the ejecta. From the luminosities of individual spectral lines, information on the synthesised masses of individual elements, as well as on the total mass of the progenitor star, can be obtained.

The main goal of this thesis is to provide novel methodologies to analyse these nebular phase spectra in greater detail. To do so, a main component is the modeling of synthetic nebular phase spectra based on ejecta models. These models inform us on the relevant physical conditions in the ejecta at a given epoch, necessary for proper interpretation of spectral line luminosities. In **Paper I** the diagnostic potential of a nebular nitrogen line seen in SESNe is investigated, and it is shown that this line, under specific conditions, directly probes the mass of the SN progenitor. **Paper II** instead focuses on two emission

lines of carbon. A Monte Carlo radiative transfer code is developed to properly extract their luminosities, and it is shown that spectral models overproduce the strength of these lines when compared to a sample of SNe, suggesting too much carbon is produced in current stellar evolution models. Finally, **Paper III** provides a framework for analysing nebular-phase spectra from the James Webb Space Telescope (JWST). By applying this framework to observations of Type Ic SN 2024aecx, it is shown that a single JWST spectrum allows for estimation of elemental masses of Cl, Ar, Ni and Fe. The mass of Cl found in Type Ic SN 2024aecx decisively indicates that SNe are the main production sites of the intermediate odd-Z elements, but that ingredients are missing in stellar evolution modeling to reproduce the observed abundances. Furthermore, it is found that the Ni-bubble effect, an uncertain parameter in SN spectral modeling, for this SN is a lot weaker than typically assumed.

Abstrakt

Kärnimplosions Supernovor (CCSNe) är de explosiva dödsfallen för de mest massiva ($M \gtrsim 8\ M_{\odot}$) stjärnor. Under dessa kraftfyllda händelser kastar stjärnorna ut de grundämnen som de producerade under sina livstid via kärnfusion. Dessa samma grundämnen utgör majoriteten av de grundämnen som finns i varenda människa på jorden. Bara på grund av det här faktumet är det oerhört viktigt att forska i SNe och därmed deras föregångare.

Den överväldigande majoriteten av SNe inträffar för långt bort för att man ska kunna urskilja deras föregångare i teleskopbilder: hittills finns det endast direkta bilder av föregångarna för några dussin röda superjättar (RSGs), föregångarna till väte-rika Type II SNe. Bilder av gula och blåa superjättar (YSGs/BSGs), som leder till strippade envelopp-SNe (SESNe) av de väte-fattiga Typerna Ib, Ic och IIb, är mycket mer sällsynta, med endast ett fåtal bekräftade föregångare hittills. Att lära sig om föregångarstjärnorna till SESNe görs därmed mest effektivt genom att studera själva SNe.

SN-explosioner följs av en ljusshow som varar i några år. Spektrala observationer under den nebulära fasen, perioden då SN utkast har blivit genomskinliga för strålning ända ner till kärnan, ger ett utmärkt tillfälle att studera grundämnen i utkastet. Från ljusstyrkor av de individuella spektrallinjerna kan man få ut information om massorna av de producerade ämnena, samt om den totala massan av stjärnan som exploderade.

Huvudmålet med denna avhandling är att skapa nya metoder för att analysera dessa nebulära spektra i större omfattning. För att uppnå detta mål krävs det bland annat modellering av syntetiska nebulära spektra, baserad på detaljerade utkastmodeller. Modelleringen förser oss med viktig information kring densiteterna, temperaturerna och jonisationsbalansen i SN utkastet vid en särskilt tidpunkt, information som är nödvändig för en korrekt tolkning av spektral linjernas ljusstyrkor. I **Paper I** studeras den diagnostiska potentialen hos en spektrallinje orsakad av kväve i SESNe, och det visar sig att denna linje, under särskilda omständigheter, kan direkt relateras till den totala massan av SN

föregångaren. **Paper II** fokuserar istället på två spektrallinjer orsakade av kol. För att extrahera deras ljusstyrkor skapas en Monte Carlo strålningstransportkod, och det visar sig sedan att spektral modeller överproducerar linjestyrkorna när man jämför med observerade SNe. Denna observation pekar mot att det finns för mycket kol i de använda stjärnevolutionsmodellerna. Slutligen så presenteras det i **Paper III** en ny ram för att analysera spektra från James Webb rymdteleskopet (JWST). Genom tillämpning av denna ram på observationer av Type Ic SN 2024aecx, visar det sig att man utifrån ett enda JWST spektrum kan bestämma grundämnesmassorna av Cl, Ar, Ni och Fe. Massan av Cl som uppmäts i SN 2024aecx visar att SNe är den huvudsakliga platsen för Cl produktion i universum, samtidigt som det saknas ingredienser i stjärnevolutionsmodeller för att uppnå de observerade mängder. Utöver detta framgår det att Ni-bubble effekten, en osäker parameter i SN spektral modellering, är mycket svagare i denna SN än vad som ofta antas.

Samenvatting

Kernimplosie supernovae (CCSNe) vormen het explosieve eindpunt van de levens van de meest massieve sterren (massa bij geboorte groter dan acht zon's massas; $M_{\mathrm{ZAMS}} > 8$ $M_{\odot}$). Tijdens deze krachtige explosies worden de elementen die de ster, door middel van kernfusie, tijdens zijn leven vormde het heelal ingeslingerd. Op deze manier staan supernovae voor de productie van de meerderheid van de elementen die vandaag de dag in het heelal aanwezig zijn. Dit maakt de studie van CCSNe en de sterren die uiteindelijk tot CCSNe leiden ('voorgangers') essentieel.

De overgrote meerderheid van SNe vindt plaats op zo'n grote afstand dat het niet mogelijk is om de voorganger van de ontploffing waar te nemen: vandaag de dag hebben we directe waarnemingen van slechts enkele tientallen rode superreuzen (RSGs), de voorgangers van waterstofrijke Type II SNe. Waarnemingen van gele- en blauwe superreuzen (YSGs/BSGs), die leiden tot stripped envelope SNe (SESNe; supernovae van sterren die hun buitenste waterstof- (en eventueel helium-) schaal zijn verloren), zijn zeldzamer, met slechts een handvol bevestigde voorgangers. Om meer over de voorgangers van SNe te weten komen is het daarom eenvoudiger om de SNe zelf te bestuderen.

SN explosies worden gevolgd door lichtstraling die honderden jaren zichtbaar blijft. Spectrale waarnemingen tijdens de nebulaire fase, de periode waarin het uitgeworpen materiaal tot in de kern transparant is voor licht, bieden een ideale mogelijkheid om de nieuwgevormde elementen te onderzoeken. Door de lichtsterkte van individuele spectraallijnen te meten, kan informatie worden vergaard over de aanwezige massa van een specifiek element, zowel als over de totale massa van de ster die ontplofte.

Het doel van dit proefschrift is om nieuwe methodes te verstrekken voor het analyseren van nebulaire spectra. Een belangrijke component tot de ontwikkeling van deze methodes is het simuleren van model spectra gebasseerd op realistische explosiemodellen. Zulke modellen informeren ons over de relevante fysieke omstandigheden in het uitgeworpen

materiaal op een bepaald tijdpunt, informatie die noodzakelijk is voor een correcte interpretatie van lichtsterkte van spectraallijnen. In **Paper I** wordt het diagnostieke potentieel van een nebulaire stikstof lijn in SESNe onderzocht en wordt getoond dat de sterkte van deze lijn, onder specifieke omstandigheden, een maat is voor de totale massa van de voorganger. In **Paper II** zijn het koolstoflijnen die worden geanalyseerd. Een Monte Carlo stralingstransport code, ontwikkeld om de lichtsterkte van deze lijnen te meten, wordt gepresenteerd en toegepast. Dankzij deze toepassing wordt laten zien dat de sterkte van koolstoflijnen in modelspectra te sterk is vergeleken met waargenomen SNe, wat suggereert dat hedendaagse sterrenevolutie modellen te veel koolstof produceren. Ten slotte wordt in **Paper III** een kader gepresenteerd voor het analyseren van nebulaire spectra verworven met de James Webb ruimetelescoop (JWST), een telescoop die niet optische maar infrarode golflengtes waarneemt. Het kader wordt toegepast op de Type Ic supernova 2024aecx, waarmee wordt laten zien dat een enkel JWST spectrum voldoende is voor de bepaling van de massa's van de elementen chloor (Cl), argon (Ar), nikkel (Ni) en ijzer (Fe). De geschatte Cl massa in SN 2024aecx bevestigt dat SNe de hoofdlocatie vormen van de 'middelste oneven-Z elementen' (fosfor (P), chloor, kalium (K) en scandium (Sc)) in het universum, maar dat er onderdelen ontbreken in sterrenevolutie codes om de juiste hoeveelheden van deze materialen te produceren. Verder wordt aangetoond dat het nikkel-bubbel effect, een onzekere variable in SN spectraalmodellering, voor deze supernova een stuk zwakker is dan in het algemeen voor SNe wordt aangenomen.

List of Papers

Paper I: ***"Nebular nitrogen line emission in stripped-envelope supernovae - a new progenitor mass diagnostic"***
S. Barmentloo, A. Jerkstrand, K. Iwamoto, I. Hachisu, K. Nomoto, J. Sollerman and S. Woosley, 2024, *Monthly Notices of the Royal Astronomical Society*, Volume 533, Issue 2, pp.1251-1280 DOI:10.1093/mnras/stae1811

Paper II: ***"Formation and diagnostic use of carbon lines in stripped-envelope supernovae"***
S. Barmentloo and A. Jerkstrand, 2026, *Monthly Notices of the Royal Astronomical Society*, Volume 545, Issue 1, 31 pp DOI:10.1093/mnras/staf2033

Paper III: ***"A Framework for Analysing Nebular-Phase JWST Supernova Spectra with Application to Type Ic SN 2024aecx"***
S. Barmentloo and A. Jerkstrand, 2026, *Monthly Notices of the Royal Astronomical Society*, submitted

A summary of these papers can be found in Chapter 8. The papers are attached at the end of this thesis, in chronological order of publication.

Papers that are not included in the Doctoral Thesis

"Dramatic Rebrightening of the Type-changing Stripped-envelope Supernova SN 2023aew"
Y. Sharma, J. Sollerman, S.R. Kulkarni et al., including **S. Barmentloo**, 2024, *The Astrophysical Journal*, Volume 966, Issue 2, id.199, 16 pp.
DOI:10.3847/1538-4357/ad3758

"Luminous Type II Short-plateau SN 2023ufx: Asymmetric Explosion of a Partially Stripped Massive Progenitor"
A.P. Ravi, S. Valenti, Y. Dong et al., including **S. Barmentloo**, 2025, *The Astrophysical Journal*, Volume 982, Issue 1, id.12, 22 pp. DOI:10.3847/1538-4357/adb0bb

"Precursor Activity Preceding Interacting Supernovae I: Bridging the Gap with SN 2022mop"
S.J. Brennan, **S. Barmentloo**, S. Schulze et al., 2025, *ArXiV pre-print*, DOI:10.48550/arXiv.2503.08768

"Charge transfer in C + O+ collisions and its impact on supernova spectra"
D. Reja, P.S. Barklem, **S. Barmentloo** et al., 2025, *Astronomy & Astrophysics*, Volume 704, id.A80, 6 pp. DOI:10.1051/0004-6361/202557288

"Nebular Phase Evolution of SN 2023ixf (I): From Circumstellar Infrared Echo to the onset of in-situ Dust Formation in a Type II Supernova"
A. Singh, S. Goto, A. Sarangi et al., including **S. Barmentloo**, 2026, *ArXiV pre-print*, DOI:10.48550/arXiv.2603.14137

"JWST observations of SN 2024abup: First Detection of CO in a broad-lined Type Ic Supernova and Constraints on r-process Nucleosynthesis"
M. Shrestha, L.A. Kwok, D.J. Sand et al., including **S. Barmentloo**., 2026, *ArXiV pre-print*,
DOI:10.48550/arXiv.2606.28561

"NLTE Spectral Modelling of the Nearby Stripped-Envelope Supernova 2024ehs"
W. Sand Hellman, S.J. Brennan, **S. Barmentloo** et al., 2026, *ArXiV pre-print*, DOI:10.48550/arXiv.2606.30796

"SN 2024afyu interpreted as a Pair Instability Supernova"
P.J. Pessi, **S. Barmentloo**, L. Wyrzykowski et al., 2026, *ArXiV pre-print*, DOI:10.48550/arXiv.2609.07931

Author Contributions

Contribution to **Paper I**:

- I obtained the sample of SESN spectra through WISeREP
- I created the fitting algorithm used to determine the strength of [N II] $\lambda\lambda$6548, 6583 emission, which formed the basis of the results.
- I wrote a script to translate the explosion models into zoned input files understandable by `SUMO`. These models (also used in **Paper II** and **Paper III**) were kindly provided by D. Kresse and the Garching group.
- The 2D hydrodynamical simulations were performed by K. Iwamoto, I. Hachisu and K. Nomoto, and they wrote two paragraphs on the modeling details in section 3.1.2.
- All `SUMO` runs presented in the work were run on the supercomputer Dardel by me.
- I wrote the bulk of the text. A. Jerkstrand reworded and rewrote a number of paragraphs. Two paragraphs in section 3.1.2 were written by K. Iwamoto.
- All figures and tables in the work were produced by me, except for figure 9 (Created by S. Woosley).

Contribution to **Paper II**:

- The sample of SESN spectra was taken mostly from **Paper I**, with spectra for two SNe kindly provided upon request by S. Valenti.
- All `SUMO` runs presented in the work were run on the supercomputer Dardel by me.
- The CaNARY code was written by me, starting from the radiative transfer treatment present in `SUMO`, which was originally written by A. Jerkstrand.
- I wrote the bulk of the text. A. Jerkstrand reworded and rewrote a number of paragraphs.
- All figures and tables in the work were produced by me.

Contribution to **Paper III**:

- The JWST spectrum analysed in this work was obtained through program 9233, by a team led by PI Melissa Shahbandeh. We thank this team for developing their observing program with a zero-exclusive-access period.

- The code for obtaining luminosity measurements from the JWST spectrum was written and applied by me.
- Both the analytical framework presented in this work as well as the code to apply it were written by me.
- I wrote the bulk of the text. A. Jerkstrand reworded and rewrote a number of paragraphs.
- All figures and tables in the work were produced by me.

New and Reused Material

This Doctoral thesis is based on the Licentiate thesis titled *"Nebular Nitrogen Emission in Stripped Envelope Supernovae"* (S. Barmentloo, 2024[1]), defended on October 23rd, 2024, and written by the same author. The text has been revised, updated and restructured to include topics relevant for **Paper II** and **Paper III**. All changes compared to the Licentiate thesis is are given below.

- **Abstract**: Partially copied, but with multiple additions relevant for **Papers II and III**
- **Chapter 1**: Partially copied, but with multiple additions relevant for **Papers II and III**, as well as the newly added chapters.
- **Chapter 2**: Mostly copied, with some additions regarding the nucleosynthesis of carbon and the elements studied in **Paper III**.
- **Chapter 3**: Mostly copied, except for the completely new Section 3.4 on the Ni-bubble effect important for **Papers II and III**.
- **Chapter 4**: Mostly copied, except for the completely new Section 4.5 on SNe in the NIR and MIR, relevant for **Papers II and III**.
- **Chapter 5**: A completely new chapter introducing the reader to the basics of spectral line formation theory, essential for **Paper III** and to lesser extent **Paper II**.
- **Chapter 6**: Completely Copied.
- **Chapter 7**: A completely new chapter on galactic chemical evolution, providing the bigger picture to the nucleosynthesis of elements in SNe, relevant for all three papers.
- **Chapter 8**: A completely new chapter summarising the three papers in this thesis.
- **Chapter 9**: A completely new chapter presenting an outlook on future directions for the research presented in this thesis.

[1]Available on the DiVA portal: `https://urn.kb.se/resolve?urn=urn:nbn:se:su:diva-234078`

Contents

Abstract – English **i**

Abstract – Swedish **iii**

Abstract – Dutch **v**

List of Papers **vii**

Author Contributions **ix**

New and Reused Material **xi**

Acronyms **xvii**

List of Figures **xviii**

1 Introduction **1**

2 Massive Stellar Evolution **5**

2.1 Nuclear Burning Stages 5

2.1.1 Hydrogen Burning 5

2.1.2 Helium Burning 9

2.1.3 Advanced Burning Stages 12

2.2 Mass Loss 13

2.2.1 Stellar Winds 13

2.2.2 Binary Interaction 14

3 Core Collapse **18**

3.1 From Star to Explosion 18

3.1.1 Loss of Outward Pressure . . . 18
3.1.2 Collapse, Bounce and Shock . . . 19
3.1.3 Explosion . . . 19
3.2 Explosive Nucleosynthesis . . . 20
3.3 The Role of Mixing . . . 21
3.4 The Ni-bubble Effect . . . 24

4 The Supernova **26**
4.1 History and Classification . . . 26
4.2 Light curve . . . 28
4.3 Photospheric Phase . . . 32
4.4 Nebular Phase . . . 34
4.4.1 Line Strengths . . . 34
4.4.2 Line Profiles . . . 38
4.5 Beyond the Optical: SNe in the NIR and MIR . . . 40
4.5.1 Molecules . . . 40
4.5.2 Dust . . . 41
4.5.3 Ejecta . . . 42

5 Line Formation Theory **43**
5.1 Atomic Structure . . . 43
5.1.1 Local Thermodynamic Equilibrium . . . 45
5.1.2 Optical Depth . . . 46
5.2 Line Luminosity . . . 46
5.2.1 LTE . . . 47
5.2.2 NLTE . . . 53

6 Modeling Supernova Spectra **55**
6.1 History . . . 55
6.2 Creating a Model Spectrum . . . 57
6.2.1 Energy Deposition . . . 57
6.2.2 Non-thermal Processes . . . 58
6.2.3 Level Populations . . . 58
6.2.4 Temperature Structure . . . 59

6.2.5 Radiative Transfer 60
6.3 SUMO 61

7 The Role of Supernovae in Galactic Chemical Evolution 62

8 Paper Summary 67
8.1 Paper I: Nebular Nitrogen Line Emission in Stripped-Envelope Supernovae - a New Progenitor Mass Diagnostic 67
8.2 Paper II: Formation and Diagnostic Use of Carbon Lines in Stripped-Envelope Supernovae 69
8.3 Paper III: A Framework for Analysing Nebular-Phase JWST Supernova Spectra with Application to Type Ic SN 2024aecx 70

9 Closing Words 73

Acknowledgements 75

Acronyms

AGB	Asymptotic Giant Branch
BH	Black Hole
CCSN	Core-Collapse Supernova
CCSN	CSM
ECSN	Electron-Capture Supernova
GCE	Galactic Chemical Evolution
HN	Hypernova
IR	Infrared
JWST	James Webb Space Telescope
LTE	Local Thermodynamic Equilibrium
MIR	Mid Infrared
MRSN	Magneto-Rotational Supernova
MS	Main Sequence
NIR	Near Infrared
NLTE	Non-Local Thermodynamic Equilibrium
NS	Neutron Star
RLOF	Roche Lobe Overflow
SESN	Stripped-Envelope Supernova
SN	Supernova
SNR	Supernova Remnant
WD	White Dwarf
WR	Wolf-Rayet

List of Figures

2.1 Compositional profiles for two model stars evolved to the end of silicon burning, including mass loss. Note how these models still contain their outer hydrogen envelopes, and that they would therefore not explode as SESNe. However, the final composition of the layers interior to the hydrogen envelope ($M_{He-core} \sim 4$ and 8 $M_{\odot}$) will be (barring mass loss) qualitatively the same (Arnett 1996). The fraction of nitrogen mass to total mass of these helium cores is seen to be larger for the lower-mass star, a finding that will be reaffirmed in **Paper I** and will form the basis for the nitrogen diagnostic developed there. One should also note that the iron core (which will collapse to a neutron star) is included in these profiles: the SN ejecta start around 1.4 and 1.6 $M_{\odot}$. *Image credit: figure 9 in Woosley et al. (2002).* 6

2.2 Schematic representation of the four cold CNO cycles (cold meaning the rate of proton captures is slower than beta-decay, as is typical in the cores of massive stars). A cycle is finished once an α-particle (i.e. a ^{4}He nucleus) is released. The slowest reaction in the dominant CNO-I cycle is $^{14}\mathrm{N}(p,\gamma)^{15}\mathrm{O}$, leading to a build up of ^{14}N in processed hydrogen layers. *Image credit: adaptation of figure 6 in Bertulani & Kajino (2016).* 7

2.3 Comparison of the evolution of the central ^{14}N abundance for eight different stars. The x-axis shows the central ^{1}H abundance, which decreases with time during the MS through CNO burning of ^{1}H into ^{4}He. Each model is named by M_{ZAMS} in units of $M_{\odot}$, the $^{14}\mathrm{N}(p,\gamma)^{15}\mathrm{O}$ reaction rate in units of the new, slower rate (see Section 2.1.1) and the initial metallicity in units of $Z_{\odot}$. As becomes clear from the figure, the ^{14}N abundance reaches equilibrium on the MS in all models, so that the reaction rate does not strongly influence the final nitrogen mass in the star. Rather, the initial metallicity is the dominant factor in determining the final central ^{14}N abundance. . . . 8

2.4 Compositional profiles for a model excluding wind mass loss (he4p50MdZ) and including wind mass loss (he6p0; this is the same he6p0 model used in **Papers I, II and III**). The size and composition of the He/N layer (the rightmost blue-shaded region in each subplot) is practically equal in both stars. On the other hand, the He/C layers (the layer left to the He/N layer) differ strongly, especially in abundance of ^{14}N ($\sim 2 \times 10^{-5}$ vs $\sim$ a few $\times 10^{-3}$) and ^{12}C (a few $\times 10^{-2}$ vs a few $\times 10^{-1}$). The mixing models in **Paper I** found that inmixing of the He/N layer is negligible, but that the He/C layer can mix in significantly at up to 40%, making these differences significant. *Image credit: figure 1 in Dessart et al. (2023).* 11

2.5 Schematic representation of Roche Lobe Overflow. The primary (the star on the left) expands at the end of the MS, filling its Roche Lobe and transferring mass to the secondary (step 2 in the figure). If the stripping is complete, it leaves the primary as a bare helium star, to finally explode as a Type Ib SN. *Image credit: adaptation of figure 3 in Lazarus et al. (2014).* 15

3.1 Schematic of microscopic- and macroscopic mixing during a SN. Each coloured circle represents material originating from one specific compositional zone. The continuous colours in the microscopic mixing case represent a smooth transition in compositions. As described in Section 3.3, macroscopic mixing of the five core regions is required to reproduce observations. The dedicated mixing simulations in **Paper I** find that for the lighter progenitors, also the He/C layer is partially macroscopically mixed into the core. For a detailed description of how macroscopic mixing is treated in the spherically symmetric `SUMO` code, see section 2.1.1 in Jerkstrand et al. (2011). 22

4.1 Schematic light curves of the different SN types. Note that Type Ib and Type Ic SNe have similar LC shapes, so that only Type Ib is included. When the figure was first published, Type IIb had not been recognised as a class yet. Figure 4.2 showcases a typical Type IIb LC. *Image credit: figure 3 in Filippenko (1997).* 28

4.2 A model light curve of a SESN. The dashed line indicates the LC in case of no ^{56}Ni powering taking place. The shock breakout and shock cooling phases are representative of a Type IIb, with it being much shorter or totally absent in most Type Ib and Ic SNe. As mentioned in Section 4.2, the width and luminosity of the ^{56}Ni peak can be used to estimate key properties of the SN, such as $M_{\rm ej}$ and $M_{^{56}\rm Ni}$. *Image credit: figure 1 in Bersten & Mazzali (2017).* 29

4.3 Photospheric spectra for five different types of SNe, taken around maximum light. The ions causing the strongest absorption features are indicated in the plot. Note how the location of the minimum of the Ca II feature shifts to redder wavelengths down the plot, indicating the successively lower velocities for the different types of SNe (as discussed in Section 4.3). In Paper I, we focus solely on Type Ib, Ic and IIb SNe. *Image credit: figure 1 in Vinkó et al. (2023).* 31

4.4 Schematic representation of P Cygni line formation (for more details, see Section 4.3). The top panel shows the outer gas shell in white and the photosphere in green. The observer is to the left of the plot. The bottom panel shows the line profile as seen by the observer, with blueshifted wavelengths to the left and redshifted to the right. For SNe, typical conditions are eps $\sim$ 0, with 'eps' the probability of a photon being absorbed in an interaction). *Image credit: A. Jerkstrand.* 33

4.5 Spectral sequence of the Type IIb SN 2011dh (Ergon et al. 2015), evolving from the photospheric to the nebular phase. Each panel shows in red an epoch of SN 2011dh, starting at 99 days post explosion (end of the photospheric phase) and ending at 415 days post explosion (firmly in the nebular phase). In black, a model spectrum is shown for that epoch. Identified lines are indicated in each plot. From the last epoch, it becomes clear that the spectrum is line-dominated by mostly forbidden lines. *Image credit: figure 4 in Jerkstrand et al. (2015a).* 35

4.6 Model $L_{\rm norm}$ curves for the model grid in Jerkstrand et al. (2015a). The observations of SNe 2011dh, 2008ax and 1993J are indicated by circles, diamonds and squares, respectively. While the 17A model ($M_{\rm ZAMS} = 17 M_{\odot}$) is clearly separated, the models for $M_{\rm ZAMS} = 12$ and 13 $M_{\odot}$ show overlap. This overlap is caused by different settings for the treatment of e.g. molecules and mixing. In Paper I, we were able to constrain the mixing with dedicated models (see section 3.1.2 in paper I), and molecules are known to not play a role (see Section 4.4.1). *Image credit: figure 15 in Jerkstrand et al. (2015a).* 37

4.7 Six different theoretical line profiles for nebular supernova spectra. In Paper I, we allowed the line profiles to be modeled with either Gaussian or thin shell profiles, with Gaussians being the most common. Note that these line profiles all assume spherically symmetric ejecta. *Image credit: figure 2 in Jerkstrand (2017).* 39

5.1 A Grotrian diagram for the first five levels in neutral carbon, the atom investigated in **Paper II**. Each horizontal line represents an energy level, with lines between levels indicating transitions. As the ground state is a triplet (not visible due to small energy separation), transitions connecting to it are multiplets. Transitions connected to one of the triplet states are so weak that they are not indicated. 44

5.2 Reproduction of the Line Regime Plot (LRP) for [Ni II] 6.636 μm form **Paper III**. Inspired by figures in Jerkstrand et al. (2025), it presents the Sobolev optical depth τ_S and the ratio between current and critical electron densities, $n_e/n_{e,crit}$, for a grid of helium star models of different masses and different Ni-bubble strengths. For visual purposes, $n_e/n_{e,crit} > 1000$ was set to 1000. 48

5.3 A reproduction of Figure 14 from **Paper III**: The theoretical luminosity ratio $L_{\text{[Ni II] 6.636 }\mu\text{m}}/L_{\text{[Co II] 10.52 }\mu\text{m}}$ as a function of $\tau_{\text{[Ni II] 6.636 }\mu\text{m}}$, for different temperatures and three cases of the Ni/Fe ratio. The 16th – 84th percentile bounds on the observed $L_{\text{[Ni II] 6.636 }\mu\text{m}}/L_{\text{[Co II] 10.52 }\mu\text{m}}$ ratio for SN 2024aecx are shown in horizontal, black dashed lines. For all three cases, $\tau_{\text{[Ni II] 6.636 }\mu\text{m}}$ is tightly constrained by the observed ratio, with the allowed range indicated in orange. 52

6.1 Model spectrum for an 8 $M_\odot$ helium core at 300 days after explosion (Fransson & Chevalier 1989). The authors note that the line profiles are too flat topped due to the fact that their stellar models have kept the onion shell structure intact, putting the material of each element at a too narrow velocity range. The code used for spectral modeling in Paper I, `SUMO`, solves this issue through complete macroscopic mixing in the core (see Section 3.3). *Image credit: figure 12 in Fransson & Chevalier (1989).* 56

6.2 Plot showing the part of the energy from non-thermal electrons going into the ionisation, excitation and heating for a pure oxygen nebula. *Image credit: figure 4 in Kozma & Fransson (1992).* 58

7.1 A figure showcasing the nucleosynthesis assumptions for stars of different masses in an early GCE model. *Image credit: figure 1 in Truran & Cameron (1971).* 63

7.2 Modeled contributions of the different enrichment processes to observed elemental abundances. The names of the different processes are given in the top center of the figure. The solar values (time as a vertical dotted line, abundance as in Asplund et al. (2009) as a horizontal dotted line) are indicated for each element. Note that the yields from ECSNe and MRSNe are included in the yields of Core-collapse Supernovae. *Image credit: figure 39 in Kobayashi et al. (2020).* 64

Figures without explicit attribution were created by the author of this thesis.

1 Introduction

The year is 1987, the day February 24th. Thin clouds bring moderate amounts of snow to Stockholm, where temperatures are just below freezing. Nothing seemed out of the ordinary. And then suddenly, on the other side of the world, there it was: a new star in the night sky. After traveling through the universe for 168000 years, light emitted during the explosion of the massive star Sanduleak -69 202 reached the eyes of hundreds of millions of people in the southern hemisphere. Many of them may not have even realised it was there, hidden among the thousands of other stars visible to the naked eye. But these photons originated from something more profound than all the others: the expulsion of large amounts of heavy elements such as carbon, oxygen and calcium. The ensemble of past similar explosions, known as supernovae, provided the very building blocks of the bodies of the happy observers, as well as the oxygen that they breathed. In fact, all of the elements in the periodic table from oxygen to rubidium are mainly produced in these violent deaths of stars (Kobayashi et al. 2020). This makes the study of these events a necessity to understanding where we, and everything around us, come from.

To be able to understand these explosive deaths, it is paramount to understand what those twinkling specks we see at night actually are. It all starts with a giant cloud of cool ($\sim$ 10 K) molecular gas. The force of gravity will slowly increase the density of these clouds, until the gas pressure in (part of) the cloud is no longer strong enough to counter gravity. At this point, this (part of the) cloud will start to collapse onto a central point[1]. The density and temperature around this central point will continue increasing (disassociating the molecules into individual atoms), until the temperature becomes high enough to start fusing four protons (basically stripped hydrogen nuclei) together to form a helium nucleus. The merging of protons into helium turns some of the proton's mass into energy, creating an outward pressure that finally stabilises the star hydrodynamically

[1]Surely not for the last time ...

and stops it from collapsing any further.

Throughout its life, the star will go through a handful more such burning stages, each time burning the ashes of the previous stage to even heavier nuclei. Exactly which burning stages the star goes through depends on its mass: for star similar to the sun, the star will burn the helium in its core into carbon and oxygen. Once it has run out of helium to burn, the temperatures will be too low to start any further burning. Such a star will slowly cool down as a White dwarf, supported against gravity through degeneracy pressure of electrons. However, if the mass is above $\sim 8\ M_\odot$ (Heger et al. 2003), it will continue to burn heavier elements, going through carbon-, neon-, oxygen- and finally silicon burning. At this point, the core of the star is made up of iron nuclei. Fusing iron nuclei costs energy instead of producing it, so that nuclear fusion stops and the outward pressure is lost. Run-away electron captures and/or thermal photodisintegration can lead to the core collapsing. As the effective Chandrasekhar mass is lower than the Fe core masses, white dwarf formation is not possible but collapse continues until formation of a neutron star or a black hole, with the outer layers of the star instead ejected into space, visible as a supernova event.

These supernovae, of which more than a dozen different classes have been identified (Gal-Yam 2017), provide us with a wealth of information. Through the evolution of their light curves (the evolution of the SN luminosity with time), we can constrain their explosion energy, ejecta mass and the extent of mixing, all of which further our understanding of how stars evolve and eventually explode. Spectra in the early (up to $\sim 100 - 200$ days), optically thick *photospheric* phase are difficult to interpret due to the blending of a forest of broad emission and absorption lines. However, during the later ($\gtrsim 200$ days), optically thin *nebular* phase, spectra are dominated by much fewer, mostly isolated emission lines. These lines allow for detailed study of how the elements producing them are created in stars, and consequently expelled into the universe.

So far, studies on the formation of lines from individual elements, combined with examination of their presence in a sample of observed nebular spectra, have been lacking. Today, with sufficiently advanced modeling codes, atomic data and more than a hundred high quality nebular spectra of stripped-envelope SNe, such a study can finally be undertaken. These SESNe are particularly well suited for such a study, as their lack of hydrogen envelopes means that spectra will not be dominated by a multitude of hydrogen lines, they provide a comparatively large part of the nucleosynthesis of SNe and recently multiple

grids of hydrodynamical and nucleosynthesis models for SESNe have been released (e.g. Woosley 2019; Ertl et al. 2020; Farmer et al. 2021). Finally, the arrival of the James Webb Space Telescope opens up the IR wavelength window for these nebular spectral analyses, a window in which the spectral lines are typically even fewer and more easily interpretable than in the optical.

It is precisely the study of these nebular spectra that forms the basis to the work presented in this thesis. Distributed over three papers, I have developed methodologies for analysing nebular spectra of SNe, and I have then tested these methodologies against both observed, as well as simulated SN spectra. These simulated spectra I created using the `SUMO` spectral synthesis code, a code without which this work could not have been possible. Each of the developed methodologies tells us something about the star that exploded, as well as about how the universe is enriched in the elements that are created by these stars. In **Paper I**, we investigated the diagnostic potential of the nebular nitrogen line [N II] $\lambda\lambda$6548, 6583, showcasing that its strength may directly be used to infer the progenitor mass of the star that exploded. To study the formation of carbon lines was the main goal of **Paper II**. Among other things, we find that the two most prominent carbon lines, [C I] λ8727 and [C I] $\lambda\lambda$9824, 9850, are weaker in an observed sample than expected from our model grid, suggestive of too large carbon masses in stellar evolution models. Finally, **Paper III** presents an analytical formalism for the study of nebular IR spectra as increasingly obtained by the JWST. With this formalism, one may obtain elemental masses, emitting volumes and temperatures, allowing for a deeper understanding than typically possible from optical spectra. In the paper, we apply the formalism to a JWST spectrum of Type Ic SN 2024aecx, and obtain results on its nucleosynthesis of Cl, Ar and Ni, as well as constraints on the explosion physics of the SN.

Before we can fully understand the results presented in these papers, this thesis provides the reader with the necessary background. In Chapter 2, an overview is presented of the nucleosynthesis and chemical enrichment occurring in massive stars during their lifetimes, with a particular focus on nitrogen and carbon, relevant to **Paper I** and **Paper II**. Next, Chapter 3 goes through the eventual collapse and explosion of the star. In this chapter, I also discuss the important but often uncertain role that mixing of the ejecta during the explosion has in shaping the emergent supernova spectrum. Chapter 4 then describes the supernova event in its entirety, as well as presenting a brief historical overview of the study of SNe. In this chapter, the focus will be mainly on Stripped-envelope SNe, as

these SNe are the main characters in the papers presented here. Chapter 5 goes through the theoretical background on spectral line formation in SNe, as well as in which regimes line luminosities can tell us about elemental masses, emitting volumes and temperatures in the ejecta, essential for understanding the results in **Paper III**. Chapter 6 goes over the basic ingredients necessary to model a supernova spectrum, as well as how this is done in `SUMO`, the code used for simulating model spectra in the three papers. In Chapter 7 I then describe the current understanding of the role that supernovae play in the chemical enrichment of our galaxy. Chapter 8 provides a short summary of the papers included in this thesis, and then Chapter 9 provides an outlook on future directions for the work presented here. Right after Chapter 9, the three papers are reproduced.

2 Massive Stellar Evolution

During a star's life, it fuses light elements into heavier elements, also known as 'nuclear burning'. This fusion releases energy, preventing the star from collapsing under its own weight. Six different burning phases occur, which will be discussed in this chapter. What one is left with after the final silicon burning phase, is an onion-like shell structure in the star, where each shell has an almost homogeneous composition throughout (see Figure 2.1). Each shell's composition is the result of one of the burning phases. For Type II SN progenitors, the shells that can be distinguished from the outside inward are the *envelope*-layers H, He/N, and He/C (Type Ib SNe lack the H-layer, Type Ic SNe also the He/N and He/C layers), and the *core*-layers O/C, O/Ne/Mg, O/Si/S, Si/S and Fe/He. These layers are named after the most abundant elements, again see Figure 2.1. Section 2.1 goes through the processes relevant during the various burning phases, with a particular focus on the effects on the nitrogen and carbon abundances, relevant for **Paper I** and **Paper II**. Section 2.2 then discusses how stars lose mass already during their lives, which has a large influence on the amount of eventually ejected nitrogen, and for some SNe even the amount of ejected carbon (as well as the final type of SN).

2.1 Nuclear Burning Stages

2.1.1 Hydrogen Burning

For the majority (~ 90 %) of its lifetime, a star is slowly burning away its primordial hydrogen and turning it into helium. While for low-mass ($M_{\mathrm{ZAMS}} \lesssim 1.5\ M_{\odot}$) stars this mainly occurs via the proton-proton chain (LeBlanc 2010), high-mass stars burn their hydrogen for the most part via the carbon-nitrogen-oxygen-cycle (CNO-cycle). In this reaction chain, protons attach to C, N and O nuclei, until eventually one of these releases a ^{4}He

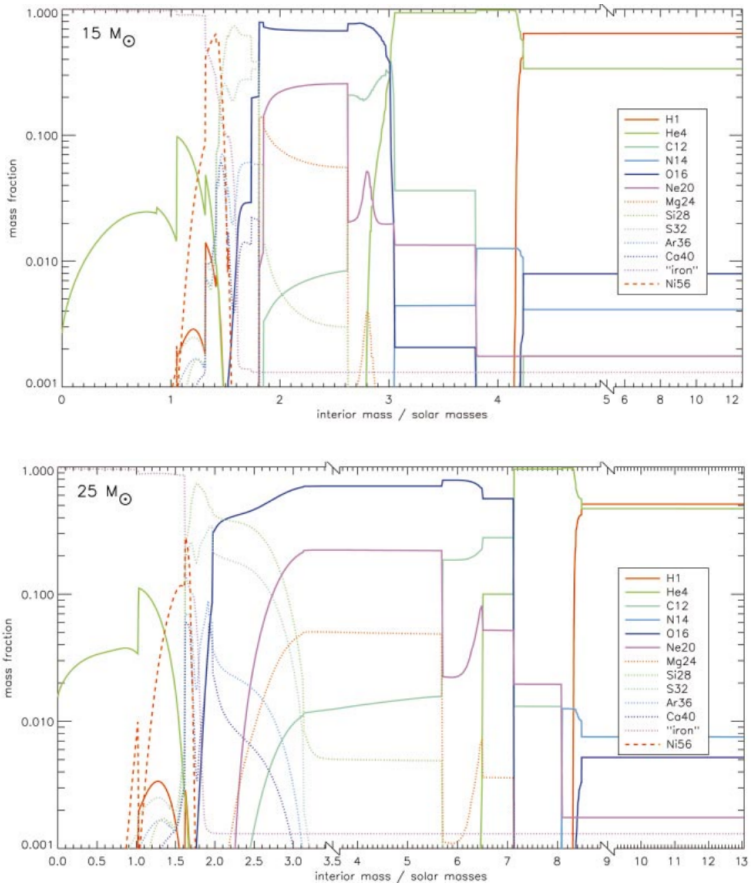

Figure 2.1: Compositional profiles for two model stars evolved to the end of silicon burning, including mass loss. Note how these models still contain their outer hydrogen envelopes, and that they would therefore not explode as SESNe. However, the final composition of the layers interior to the hydrogen envelope ($M_{He-core} \sim 4$ and 8 $M_{\odot}$) will be (barring mass loss) qualitatively the same (Arnett 1996). The fraction of nitrogen mass to total mass of these helium cores is seen to be larger for the lower-mass star, a finding that will be reaffirmed in **Paper I** and will form the basis for the nitrogen diagnostic developed there. One should also note that the iron core (which will collapse to a neutron star) is included in these profiles: the SN ejecta start around 1.4 and 1.6 $M_{\odot}$. *Image credit: figure 9 in Woosley et al. (2002).*

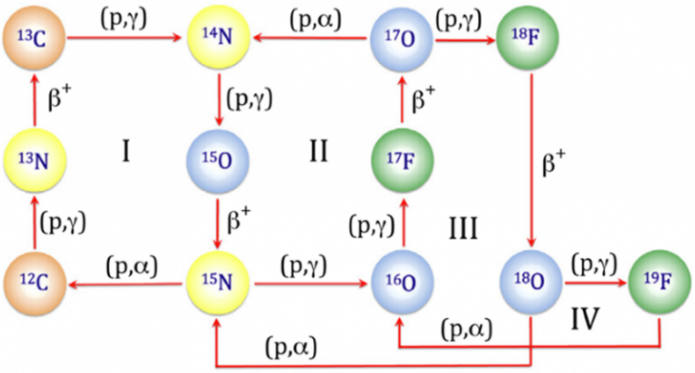

Figure 2.2: Schematic representation of the four cold CNO cycles (cold meaning the rate of proton captures is slower than beta-decay, as is typical in the cores of massive stars). A cycle is finished once an α-particle (i.e. a ^{4}He nucleus) is released. The slowest reaction in the dominant CNO-I cycle is $^{14}\mathrm{N}(p,\gamma)^{15}\mathrm{O}$, leading to a build up of ^{14}N in processed hydrogen layers. *Image credit: adaptation of figure 6 in Bertulani & Kajino (2016).*

nucleus. Three variations exist to the cycle, the most important one being CNO-I (see Figure 2.2). This cycle can be written in short form as $^{12}\mathrm{C}(p,\gamma)^{13}\mathrm{N}(e^+,\nu)^{13}\mathrm{C}(p,\gamma)^{14}\mathrm{N}(p,\gamma)$ $^{15}\mathrm{O}(e^+,\nu)^{15}\mathrm{N}(p,\alpha)^{12}\mathrm{C}$, where e.g. $^{12}\mathrm{C}(p,\gamma)^{13}\mathrm{N}$ means that one proton attaches onto a ^{12}C nucleus, creating a ^{13}N nucleus and releasing a photon.

While these cycles by themselves do not create or destroy any C, N or O nuclei, they do adjust the relative abundances of these elements due to each reaction occurring at different rates. More specifically, the reaction $^{14}\mathrm{N}(p,\gamma)^{15}\mathrm{O}$ is found to be significantly (a factor $\sim 10^2$, Adelberger et al. 1998) slower than any of the others in the CNO-I cycle, forming a bottleneck for the reaction. Because of this, the abundance of ^{14}N will increase with time in layers dominated by CNO-burning, until a steady-state is reached (Caughlan & Fowler 1962). In numbers, an initially solar metallicity region will have C, N and O abundances of 2.5×10^{-3}, 7.3×10^{-4} and 6.1×10^{-3}, respectively. At the end of CNO burning, these abundances will have changed to 2.1×10^{-4}, 8.7×10^{-3} and 1.2×10^{-4} (for our standard model '13Msun_r1_z1', see below), so that effectively all initial C, N and O is locked up into nitrogen.

Exactly what the final abundance of ^{14}N after CNO burning is, depends among other things on the reaction rate of $^{14}\mathrm{N}(p,\gamma)^{15}\mathrm{O}$. The accepted rate of this reaction has in recent

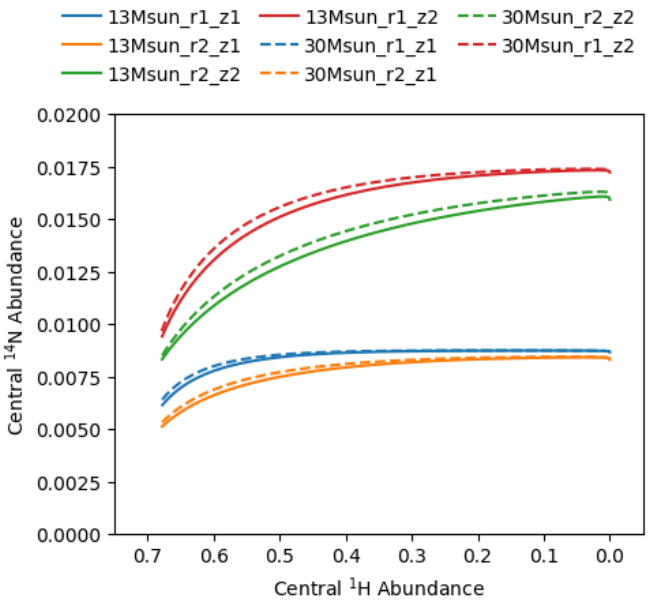

Figure 2.3: Comparison of the evolution of the central ^{14}N abundance for eight different stars. The x-axis shows the central ^{1}H abundance, which decreases with time during the MS through CNO burning of ^{1}H into ^{4}He. Each model is named by M_{ZAMS} in units of $M_{\odot}$, the $^{14}\mathrm{N}(p,\gamma)^{15}\mathrm{O}$ reaction rate in units of the new, slower rate (see Section 2.1.1) and the initial metallicity in units of $Z_{\odot}$. As becomes clear from the figure, the ^{14}N abundance reaches equilibrium on the MS in all models, so that the reaction rate does not strongly influence the final nitrogen mass in the star. Rather, the initial metallicity is the dominant factor in determining the final central ^{14}N abundance.

years been lowered by a factor of two (Frentz et al. 2022), as compared to the previous standard value from Schröder et al. (1987) that is still present in many stellar evolutionary modeling codes (including the one used by Woosley (2019), of whom the SN progenitor models in **Papers I, II and III** are adopted). While this change in rate is an important result, the fact that the rate was already so slow that it effectively converted all C and O into N means that the expected final abundances with a slower rate do not change drastically.

To emphasize this fact, I simulated a grid of eight stars using the stellar evolution code MESA (Paxton et al. 2011, 2013, 2015, 2018, 2019; Jermyn et al. 2023). The grid encompasses two masses (13 $M_{\odot}$ and 30 $M_{\odot}$), two metallicities (1 $Z_{\odot}$ and 2 $Z_{\odot}$) and two

reaction rates for $^{14}N(p,\gamma)^{15}O$ (the newer, slower rate (Frentz et al. 2022) and the old rate from Schröder et al. 1987). The evolution of the ^{14}N abundance in the helium core as a function of the central ^{1}H abundance is plotted for each model in Figure 2.3. The take away from this figure is that the largest difference in ^{14}N abundance between models that only differ in reaction rate is $\lesssim 10\%$ for the $Z = 2\ Z_{\odot}$ models. For solar metallicity (which is more typical for SESNe, see Section 2.2.1), the difference is $\lesssim 5\%$. On the contrary, the final central ^{14}N abundance can be seen to scale roughly linearly with the star's initial metallicity. In summary, the adopted rate $^{14}N(p,\gamma)^{15}O$ in **Paper I** is not expected to influence our main results.

2.1.2 Helium Burning

During the burning of hydrogen into helium, the increased molecular weight leads to a gradual decrease of outward gas pressure. This results in a contraction of the core layers, and thereby an increase in temperature and pressure. Once the temperature surpasses 10^8 K, helium itself will start to burn, mainly by the so-called triple-alpha reaction. In this reaction, three ^{4}He nuclei are consumed to form a single ^{12}C nucleus. Once enough ^{12}C has started to form, a second reaction that burns ^{4}He commences, namely $^{12}C(\alpha,\gamma)^{16}O$. The rate of this reaction determines the ratio of C/O at the end of helium burning, and influences the compactness of the stellar core (Ekström 2021), which is essential to the star's explodability (Chieffi & Limongi 2020). However, the reaction rate of $^{12}C(\alpha,\gamma)^{16}O$ is as of today still highly uncertain (see e.g. figure 1 in El Eid et al. (2009) or the reviews by deBoer et al. (2017) and Pepper et al. 2022).

Besides the $^{12}C(\alpha,\gamma)^{16}O$ reaction rate, we also discuss other processes in **Paper II** that influence the star's final carbon mass. One of these processes is a so-called shell merger. In short, a shell merger is the ingestion of material from one chemical layer into another. In e.g. a C-O shell merger, C and Ne enriched material is ingested into the O-burning shell below and consequently burned away, removing a significant fraction of the total C and Ne in the ejecta (Rauscher et al. 2002; Meakin & Arnett 2006). A recent literature study by Roberti et al. (2025) of single star stellar evolution models found that around $\sim 20\%$ of models experience such mergers (preferably in models with small CO cores and low ($X_{^{12}C} \lesssim 0.28$) central carbon abundances), while observational evidence remains lacking.

Another process influencing carbon mass in a star is binarity. Recent works (Woosley 2019; Laplace et al. 2021; Schneider et al. 2021) have found that binary-stripped stars retain a larger central carbon *abundance* $X_{^{12}\mathrm{C}}$ at central carbon-ignition compared to effectively single stars, thus making C-O shell mergers less likely (see above). However, work by Farmer et al. (2021) shows that for stars with final He-core masses $\lesssim 4.5\ M_\odot$ (expected to be typical progenitors for SESNe), the final carbon *mass* in the ejecta does not differ significantly between single and binary stars.

In summary, besides the rates of nuclear burning reactions, there are multiple other processes influencing the final C mass in SN ejecta. This results e.g. in a difference of up to a factor 3 in predicted carbon mass in the ejecta of stars with equal pre-SN masses from two different stellar evolution codes (see Section 6.1 in **Paper II**). This fact emphasizes the importance of directly obtaining estimates of carbon masses from SN spectra to constrain our stellar evolution models, which is the main goal of **Paper II**.

We now return to reactions involving nitrogen. Before any of the reactions involving carbon pick up speed, it is around $T \sim 7 \times 10^7$ K that the reaction $^{14}\mathrm{N}(\alpha,\gamma)^{18}\mathrm{F}(\beta^+\nu)^{18}\mathrm{O}$ first burns up the $\sim 1\%$ of ^{14}N in the convective core (Kotok 1967; Woosley et al. 2002). This destruction of ^{14}N happens on a time scale much shorter than that of core helium burning (Kotok 1967), and its reaction rate is quite well determined (Woosley et al. 2002; Ekström 2021).

Because the size of the convective burning core during this burning phase is smaller than during core CNO burning, not all nitrogen in the star is destroyed; a He/N layer remains right outside the convective core. For the simulated MESA models, this He/N layer decreased in size in two more episodes. The first is during a non-convective phase of nitrogen shell burning, in between central helium depletion and central carbon ignition, and transforms about 1/3 of the remaining He/N layer into a O/C layer. The second episode occurs quite late, right after central oxygen depletion, and is a convective phase which replaces a further 1/3 of the initial He/N layer with a He/C layer. This He/C layer is formed between the CO core and the He/N layer, and has a nitrogen abundance of $\sim 10^{-3}$.

Curiously, stellar evolution models obtain He/C layers of significantly varying sizes and abundances: comparing the two models of figure 1 in Dessart et al. (2023) (reproduced

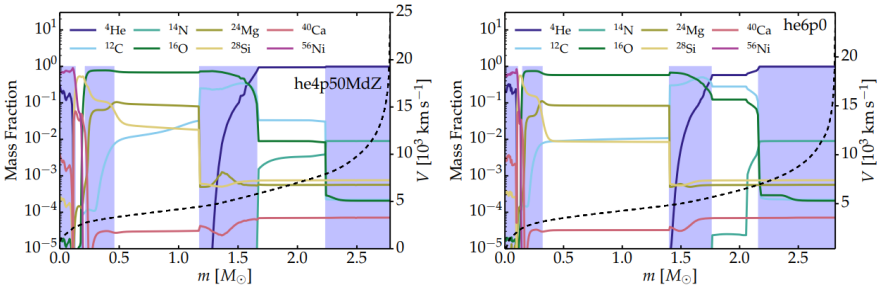

Figure 2.4: Compositional profiles for a model excluding wind mass loss (he4p50MdZ) and including wind mass loss (he6p0; this is the same he6p0 model used in **Papers I, II and III**). The size and composition of the He/N layer (the rightmost blue-shaded region in each subplot) is practically equal in both stars. On the other hand, the He/C layers (the layer left to the He/N layer) differ strongly, especially in abundance of ^{14}N ($\sim 2\times10^{-5}$ vs $\sim$ a few $\times10^{-3}$) and ^{12}C (a few $\times10^{-2}$ vs a few $\times10^{-1}$). The mixing models in **Paper I** found that inmixing of the He/N layer is negligible, but that the He/C layer can mix in significantly at up to 40%, making these differences significant. *Image credit: figure 1 in Dessart et al. (2023).*

here in Figure 2.4), which are from the same model grid by Woosley (2019) used in the papers presented in the thesis, the model without mass loss[1] (he4p50MZ) has a He/C layer with a ^{14}N abundance of $\sim$ a few $\times10^{-3}$, while the model *with* mass loss (he6p0) only has a ^{14}N abundance of $\sim 2\times10^{-5}$. Furthermore, the ^{12}C abundance in this layer increases by roughly an order of magnitude between the former and the latter model. Our MESA simulations did include mass loss, but do have a He/C layer with appreciable abundance of ^{14}N. Especially in models where the He/C layer has similar or more mass than the He/N layer (as e.g. in the Nomoto & Hashimoto (1988) hydrodynamical models in **Paper I**), this additional nitrogen may lead to significant emission, especially when considering that part of it mixes with the core and is thereby closer to the ^{56}Ni power source (see Section 3.3 and section 3.1.2 in **Paper I**). Exactly why the size of the He/C layer varies so appreciably between models is a difficult but relevant question to answer. However, in the literature there is little to no research on the formation of the He/C layer, so we have to leave this to future works.

[1]While no mass loss might sound unrealistic, it is actually a reasonable approximation to a Type IIb progenitor that loses its hydrogen envelope just before explosion.

2.1.3 Advanced Burning Stages

Once central helium is depleted, four more burning stages occur for stars with $M_{\rm ZAMS} \gtrsim 8$ – 11 $M_\odot$ (Heger et al. 2003): carbon, neon, oxygen and silicon burning, respectively. These final stages happen on a much shorter timescale than the previous two: central hydrogen and helium burn for roughly 10 and 2 Myr respectively for an $M_{\rm ZAMS} = 15$ $M_\odot$ star, with the remaining four stages combined taking a mere ~ 3 kyr (Woosley et al. 2002). As the thermal timescale for RSGs is around 10 kyr, this means that from the end of helium burning up to explosion, the observed properties of the star do not change[2].

These final burning stages are not particularly important for the nitrogen abundance (except potentially through the He/C zone formation, see Section 2.1.2). For carbon, the carbon-burning phase is naturally of importance; it burns two ^{12}C into unstable ^{24}Mg, which then decays into either ^{23}Mg, ^{20}Ne or ^{23}Na (see e.g. Woosley et al. 2002). At the completion of this carbon-burning phase, the core has a residual C abundance on the order of $\sim 1\%$, which in the core is burned away further in the remaining burning phases. Besides the effects of reaction rates, binarity and shell mergers discussed in the previous subsection, Figure 2.4 shows again that in different models, the carbon abundance in the He/C layer can vary strongly, affecting the total carbon mass in the ejecta.

Looking beyond carbon and nitrogen, the final burning stages are essential for the soon to be SN as a whole. They are the main production stages of the elements with the strongest lines in the optical during the nebular phase, such as O, Mg, Ca and Fe. Also, they produce the elements with strong emission lines in the NIR and MIR studied in **Paper III**, such as Ne, Cl, Ar, Co and Ni. In particular, Cl is believed to be formed in hydrostatic oxygen-burning, but as discussed in Chapter 7 and **Paper III**, may in fact be formed mostly during O-C shell mergers. Ar is created both hydrostatically and explosively, in both cases during oxygen- and silicon-burning. The final burning stages also lead to a build up of ^{28}Si, which through explosive burning (see Section 3.2) will produce the ^{56}Ni that will be the most important power source for the SN luminosity (see Chapter 4).

[2]This is also the reason why predicting when a star will explode as a SN is notoriously difficult; the star will not show on the outside that it is now burning silicon in its core, which would be the smoking gun for oncoming ($t \lesssim 10$ days) core collapse. However, recent observations of flash spectroscopy (Bruch et al. 2023) and progenitor activity (e.g. Brennan et al. 2024) indicate that a large fraction of stars experience enhanced mass loss only a few months prior to explosion, which if observed in nearby stars could provide the smoking gun.

2.2 Mass Loss

2.2.1 Stellar Winds

Observational evidence that stars lose mass to the environment through stellar winds started to pile up around the 1950s-1960s (Beals 1951; Deutsch 1956; Underhill 1962; Morton 1967). For massive OB stars specifically, Morton (1967) found absorption lines in the UV blueshifted by $\sim 2000 - 3000$ km s^{-1}. As typical escape velocities for such stars are ~ 500 km s^{-1} (Morton 1967), this means that the ions emitting these UV photons are escaping the star. By coupling of these ions to other particles through scattering and electrostatic forces, significant mass loss can occur (Lucy & Solomon 1970). Despite this relatively long history of observations, quantitative estimates for mass loss by winds are still uncertain up to this date (Langer 2012; Vink 2022), with theory in some regimes predicting two orders of magnitude more mass loss than observed (Martins et al. 2005), and an uncertainty of a factor 2-3 in the mass-loss rate being rule rather than exception (Smith 2014; Björklund et al. 2021). Observationally, this uncertainty arises partially due to the wind being clumped (Hillier 1991; Moffat 2008), meaning that a smooth, average mass-loss rate is hard to determine. Theoretically, accurate modeling of the wind requires treatment of tens of thousands of spectral lines (Abbott & Lucy 1985; Vink et al. 2001; Puls et al. 2020), which is a non-trivial task.

In more qualitative terms, the understanding of winds is a lot better: stars that are more massive and more metal-rich, experience stronger mass loss. It is also understood that for stars with solar metallicity[3], a mass of $M_{\rm ZAMS} \gtrsim 25 - 30\ M_\odot$ is sufficient to remove the entire hydrogen envelope before explosion (Smith et al. 2011; Zapartas et al. 2021). For such stars, the remaining mass loss will eat away at the He/N-layer from above. Whether this leads to a lower final nitrogen mass in the SN ejecta than without mass loss is a non-trivial question, as the presence of mass loss on the surface can alter the extent of e.g. the nitrogen shell burning (see Section 2.1.2), partially compensating for the surface mass loss.

It can not be overstated how uncertain the absolute strength of stellar winds is. As is discussed by Woosley (2019), the mass-loss prescription from Vink (2017) for a $M_{\rm He,\ init} =$

[3]The spread of initial metallicity in observed SNe is moderate: for a sample of 74 CCSNe, Anderson et al. (2010) found the minimum and maximum metallicity to be 0.29 $Z_\odot$ and 1.62 $Z_\odot$. Therefore, the mass at solar metallicity is a good indication.

6.0 $M_\odot$ helium star predicts a mass-loss rate 10 times lower than the prescription from Yoon (2017) for the exact same star, which would lead to an entirely different evolution of the He/N-envelope. The impact of this uncertainty on our results in **Paper I** is discussed in the paper in section 5.4.

In summary, the question of how important mass loss by winds is for the evolution of SN progenitors is yet unanswered, but what is clear is that for some stars stellar winds can play a decisive role in their (envelope-) evolution.

2.2.2 Binary Interaction

Stars form by the collapse of molecular clouds. By processes such as disk instability, core fragmentation and N-body interactions, some of these stars[4] will end up in a binary (or higher-order multiple) system (for a review, see e.g. Tokovinin 2021). Depending on their initial separation, the *primary*, the most massive star in the system, may fill its *Roche lobe*, the region in space in which material is gravitationally bound to the star, and spill over into the Roche lobe of the secondary (Roche Lobe Over Flow (RLOF); see Figure 2.5). From this point on, material leaving the Roche lobe of the primary will accrete onto the secondary and/or be ejected from the system, thus causing mass loss to occur.

Many variations of the picture painted above exist. Following the classification scheme adopted in Kippenhahn & Weigert (1967) and Lauterborn (1970), the main distinction is the evolutionary state of the primary. Case A refers to mass transfer while the primary is still on the MS, with case B mass-transfer occurring when the primary experiences hydrogen shell-burning but has not ignited central helium, and case C mass-transfer when central helium has been ignited. A whole spectrum of further subdivisions exists (Podsiadlowski et al. 1992; Nelson & Eggleton 2001; Mennekens & Vanbeveren 2014), but for their specific conditions the reader is referred to the mentioned references. What is of particular interest to us, is the rate at which mass is transferred. Typically quoted values for the faster cases are on the order of 10^{-3} $M_\odot$ yr^{-1} (Taam & Sandquist 2000; Langer 2012; Smith 2014; Petrović 2020), but this is only an order of magnitude estimate. Nonetheless, at these mass-loss rates, removing the entire hydrogen envelope of a massive star occurs in $\sim 10^4$ years only, i.e. in the blink of an eye for typical massive star lifetimes (10^7 years). Typically, a small residual hydrogen layer will be left at the end of RLOF, as

[4] in fact most of these, as we will see later on in this section.

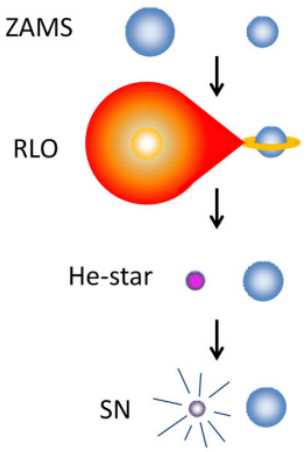

Figure 2.5: Schematic representation of Roche Lobe Overflow. The primary (the star on the left) expands at the end of the MS, filling its Roche Lobe and transferring mass to the secondary (step 2 in the figure). If the stripping is complete, it leaves the primary as a bare helium star, to finally explode as a Type Ib SN. *Image credit: adaptation of figure 3 in Lazarus et al. (2014).*

the star's radius shrinks significantly once the envelope mass becomes too low to support an extended configuration (Petrovic et al. 2005).

One of the prevailing questions in the field of massive star research, is which mass-loss channel is the most common in nature: mass loss by winds or by binary interaction? Up until about 1970, the dominant paradigm was that binary interaction was the dominant factor (Paczyński 1971). This paradigm flipped with the advent of UV astronomy, when it was found that most luminous stars actually have sufficiently strong stellar winds to remove the entire hydrogen envelope before explosion (Morton 1967; Carruthers 1968), the so-called Conti scenario (Conti 1975). More recently, around 2010, the paradigm has shifted once more to binaries being dominant, which is still the most popular theory today (Langer 2012; Smith 2014).

This most recent shift was motivated by two findings. Firstly, the fraction of massive stars in binaries has been firmly determined to be high (Mason et al. 1998, 2009; Sana et al. 2012; Kobulnicky et al. 2014; Sana 2017; Moe & Di Stefano 2017), with around 50 – 75% of them having orbital periods short enough to engage in mass transfer events. Secondly, the rapid increase in the number of observed SNe allowed to start doing proper

statistics on the relative occurrence of the different SN types. The sample observed by the Lick Observatory Supernova Search (Smith et al. 2011; Li et al. 2011) finds that $\sim 36\%$ of all CCSNe are SESNe (Types IIb, Ib and Ic), i.e. SNe that have lost (practically) their entire hydrogen envelope. Assuming a Salpeter Initial Mass Function (IMF), the authors find that if one assumes all Type Ibc SNe to come from Wolf-Rayet (WR) progenitors (single stars that lose their entire hydrogen envelope through stellar winds) the minimum initial mass of WR stars has to be 22 $M_{\odot}$. If one requires Type IIb SNe (which only have ~ 0.1 $M_{\odot}$ of hydrogen left (Podsiadlowski et al. 1993; Woosley et al. 1994; Gilkis & Arcavi 2022)) to also come from WR stars, this initial mass drops by a few $M_{\odot}$. From the modelling side, the theoretical minimum mass to lose the entire hydrogen envelope for solar metallicity stars by winds ranges from $\sim 20 - 25$ (Sander et al. 2012) to ~ 35 $M_{\odot}$ (Heger et al. 2003), depending on what mass-loss recipe is adopted. With the uncertainty still present in stellar wind mass-loss rates (see Section 2.2.1), this argument alone would not suffice to argue for either stellar winds or RLOF as the dominant mechanism for hydrogen envelope removal. The additional argument that points towards RLOF is the distribution of observed ejecta masses for SESNe. While the lowest mass WR stars would end their lives as helium stars of $\gtrsim 8 - 9$ $M_{\odot}$ (and thus $M_{\rm ej} \gtrsim 5 - 6$ $M_{\odot}$) (Yoon et al. 2017), the observed distribution for SESNe is centered around $M_{\rm ej} \sim 2 - 3$ $M_{\odot}$ (Lyman et al. 2016; Taddia et al. 2018; Prentice et al. 2019a; Barbarino et al. 2021; Karamehmetoglu et al. 2023), with only a hand full SESNe with $M_{\rm ej} \gtrsim 5 - 6$ $M_{\odot}$. Based on these arguments, RLOF is now believed to be the most important process by which massive stars are stripped of their hydrogen envelopes. It is because of this, and the fact that most stars are believed to lose their envelopes through Case B mass-transfer, that most stellar evolution models for SESN progenitors start their evolution as bare helium cores.

Returning once more to carbon and nitrogen, our main interest is in the mechanism removing the He/N-and He/C envelopes. Most models (Yoon et al. 2010; Claeys et al. 2011) suggest that RLOF, while the dominant mechanism for hydrogen envelope removal, will always leave a residual hydrogen layer. This means that it will be the stellar winds doing the work in actually removing the helium dominated layers. Such a scenario is supported by the observed metallicity dependence of SN types: it is found that compared to average-metallicity hosts, lower-metallicity galaxies produce both more Type II SNe and less Type Ibc SNe (Prieto et al. (2008); Boissier & Prantzos (2009), but see also Anderson et al. 2015). This can be explained through stellar winds, as these are stronger with

increasing metallicity. Therefore, removing the final part of the hydrogen envelope will be more difficult for lower-metallicity, so that they more likely explode as Type IIb. In **Paper I**, we find clear indications that Type IIb SN progenitors are lower mass than Type Ibc progenitors, which again would match with the scenario that lower-mass stars experience weaker winds, as discussed earlier in this section. All in all then, improvements in stellar wind prescriptions will be of most importance for obtaining a better understanding of the exact nitrogen abundances one should expect for SN progenitors.

3 Core Collapse

At the end of the Si-burning phase, the newly synthesised Fe can not be fused into heavier elements to gain energy. This removes the outward pressure that kept the star in hydrostatic equilibrium, leading to core collapse and the eventual SN explosion. In this chapter, Section 3.1 discusses how this inward collapse is eventually turned into an outward explosion. Section 3.2 covers the nucleosynthesis taking place during the explosion (as opposed to the nucleosynthesis during the star's life; Section 2.1). Section 3.3 closes off the chapter by considering macroscopic chemical mixing during the explosion, which, among other things, determines the proximity of the radioactive power source ^{56}Ni to the different elements in the ejecta.

3.1 From Star to Explosion

3.1.1 Loss of Outward Pressure

The massive star has now entered the final burning stages and is quickly approaching core collapse. Burning of the central Si/S region leads to the formation of an iron core. Iron is the most tightly bound nucleus of all elements, and can therefore not be burned to heavier elements to release energy. Furthermore, once the central temperature reaches $\sim 10^{10}$ K, Nuclear Statistical Equilibrium (NSE, when all nuclear burning reactions occur at the same rate as their inverse) favors the photo-dissociation of the iron-group nuclei into α-particles, leading to further loss of outward pressure. This lack of thermal pressure that balances the gravitational force makes the star gravitationally unstable to the layers above the core. Initially some form of stability is still provided, not by nuclear burning but by degeneracy pressure of the electrons in the core. However, this pressure can only support a core up to a certain limit: the Chandrasekhar mass (Stoner 1930; Chandrasekhar 1931).

While classically this mass has been put around $M \sim 1.4\ M_\odot$, this value originates from many simplifying assumptions, such as zero entropy in the core, absence of electrostatic interactions and no surface boundary pressure (Timmes et al. 1996). Applying appropriate corrections for these leads to a range of possible explosion- and consequently Neutron Star (NS) masses between ~ 1.2 and $2.0\ M_\odot$ (Woosley et al. 2002). As the core starts to contract, the increasing density causes free electrons (which provide the pressure) to capture onto nuclei and free protons, lowering the effective Chandrasekhar mass. In stars with $8\ M_\odot \lesssim M_{\mathrm{ZAMS}} \lesssim 9.5\ M_\odot$ (Janka 2012; Woosley & Heger 2015), rapid electron captures already occur when the star has a O/Ne/Mg-core, causing core collapse and a so-called electron-capture SN (ECSN). As soon as the effective Chandrasekhar mass has been surpassed and the last active burning shell in the core dies out, gravity wins the battle (but not the war!) and collapse commences (Woosley et al. 2002).

3.1.2 Collapse, Bounce and Shock

The collapse that has now started happens fast, on the order of 1 s. Once the density reaches $\rho \gtrsim 2.7 \times 10^{14}$ g cm^{-3}, the material experiences a phase change to homogeneous nuclear matter (Janka 2012). With protons and neutrons so tightly packed together, the strong force's repulsive effect becomes relevant, stiffening the material against further collapse. This material now functions as a spring, storing the gravitational energy provided by the infall of the upper layers. Eventually, the 'spring' starts to rebound. As the upper layers are still falling in, a shock front is created at the interface of the rebounding and infalling material (at 10 km above the core, roughly the final NS radius). Initial models found that this bounce-shock was sufficient to completely blow up the star in a SN (Baron et al. 1985). However, when one considers the loss of energy of the shock through photo disintegration of the infalling material (roughly 10^{51} erg per $0.1\ M_\odot$, Bethe (1990)), one finds that the shock is only able to extend to $\sim 10^2$ km, before stagnating (Janka et al. 2007).

3.1.3 Explosion

How then does the star eventually explode? The answer must be sought in the famously hard-to-interact-with neutrinos ν. Ever since the start of core carbon burning, these particles have been the major emission source in terms of energy of the massive star.

However, as the cross-sections for interaction are so low, the neutrinos leave the star without any interactions. It is only during the collapse phase, when core densities reach nuclear levels, that the optical depth τ_ν reaches $\sim 0.01 - 0.1$, and some neutrinos interact in the core (Janka 2012). The majority of these interactions are the absorption of ν_e and $\bar{\nu_e}$ on free neutrons and protons. Even with only several percent of the neutrino energy being absorbed by the matter in the shock, the neutrino luminosity of $L_\nu \sim$ a few 10^{52} erg s^{-1} assures that the necessary explosion energy of $\sim 10^{51}$ erg is provided through these interactions, and the star can successfully explode.

Multi-D Effects

The picture painted in Section 3.1.3 is missing a crucial part: non-spherical effects. When simulating the neutrino-heating mechanism in 1D, only ECSN-progenitors (and not iron cores) led to successful explosions (Kitaura et al. 2006), mostly due to a very steep density gradient directly outside the core. Two multi-D effects turn out to be essential for successful explosions in more massive stars. The first of these is convective overturn, i.e. the process in which 'cold' infalling matter is funneled into the gain layer and neutrino-heated bubbles expand into the region just outside of the shock (Herant et al. 1994; Burrows et al. 1995). The second is the Standing Accretion Shock Instability (SASI) (Blondin et al. 2003; Fernández et al. 2014), which is an instability of oscillatory nature at the shock front, caused by perturbations in the region between the shock and the underlying neutrino sphere. The main difference between these processes are the scales on which they operate: convective overturn works on scales smaller than the gain region, while the SASI works on global scales. While there is no consensus yet on the relative importances of convective overturn and SASI, both processes are deemed essential ingredients for the successful CCSNe observed in the universe (Janka 2012; Burrows & Vartanyan 2021).

3.2 Explosive Nucleosynthesis

The temperature increase caused by the shock ushers in one of the most important phases of a SN: explosive nucleosynthesis[1]. More specifically, it is during this phase that the majority of the radioactive ^{56}Ni, which is the main power source for SESNe (see Section

[1]The results discussed in this section are obtained mostly from Burbidge et al. (1957), Woosley et al. (1973) and Woosley et al. (2002), which themselves are compilations of a large amount of works.

4.2), is created. The final compositional profiles after explosive nucleosynthesis most strongly depend on the temperatures reached. Under the assumption of an isothermal shock, the shock temperature at radius r may be estimated via equation 3.1.

$$T_s(r) = 1.33 \times 10^{10} \left(\frac{E_{\rm kin}}{10^{51}{\rm erg}} \right)^{1/4} \left(\frac{r}{10^8 \text{ cm}} \right)^{-3/4} \text{ K.} \tag{3.1}$$

Here, $E_{\rm kin}$ is the explosion energy of the SN. For temperatures $> 5 \times 10^9$ K, obtained in the most inner regions, NSE is reached and the composition is fully reprocessed through silicon burning into iron-group elements. The most important of these, ^{56}Ni, is aided in its production by a lower neutron excess η than during hydrostatic silicon burning in the core (0.002 in the explosively burning shell versus $\sim$ 0.024 – 0.05 during core burning), favoring production of ^{56}Ni over ^{56}Fe. At the end of this explosive burning phase, the other main product for these layers is ^{4}He (freed up by photodisintegration of ^{28}Si: see Section 2.1.3), which due to the fast expansion of the ejecta does not have time to reassemble onto heavier elements.

Another explosive burning process of particular interest for nebular SESN spectra is explosive oxygen burning. Occurring between $3 \times 10^9 < T < 4 \times 10^9$ K, it is responsible for the creation of a significant part of the ejected ^{40}Ca (and ^{36}Ar, see Chapter 2 and **Paper III**). This calcium is a strong and important coolant during the nebular phase, which already at small abundances can take over large parts of the cooling from oxygen through the [Ca II] $\lambda\lambda$7291, 7323 and Ca NIR triplet lines (Fransson & Chevalier 1989; Dessart et al. 2020). Therefore, the mixing of calcium and oxygen clumps can greatly influence the line strengths of a nebular spectrum.

3.3 The Role of Mixing

The importance of macroscopic mixing for the evolution of SESNe was realised during the turn of the 1980s-90s, shortly after the modeling of the observations of SN 1987A (Ebisuzaki et al. 1989; Kumagai et al. 1989). Here, macroscopic mixing (see Figure 3.1) is the movement of clumps with a chemical composition of e.g. the He/N zone to another zone, say the Fe/He zone, while keeping its original He/N composition (microscopic mixing would mean the He/N clumps diffusing inside the Fe/He zone, so that the end situation is a Fe/He zone with only slightly different abundances). Shigeyama et al. (1990) simulated

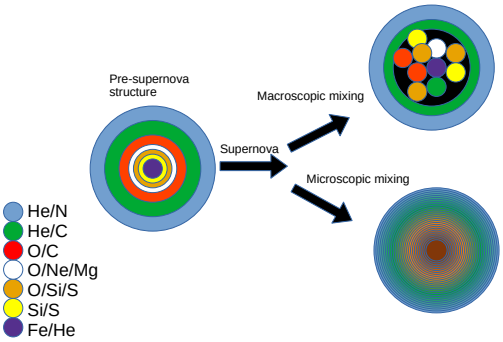

Figure 3.1: Schematic of microscopic- and macroscopic mixing during a SN. Each coloured circle represents material originating from one specific compositional zone. The continuous colours in the microscopic mixing case represent a smooth transition in compositions. As described in Section 3.3, macroscopic mixing of the five core regions is required to reproduce observations. The dedicated mixing simulations in **Paper I** find that for the lighter progenitors, also the He/C layer is partially macroscopically mixed into the core. For a detailed description of how macroscopic mixing is treated in the spherically symmetric `SUMO` code, see section 2.1.1 in Jerkstrand et al. (2011).

the light curve evolution of the explosion of three helium stars of masses M = 3.3, 4.0 and 6.0 $M_{\odot}$, both with and without macroscopic mixing of the envelope with the core (see Section 2.1 for the definitions). The main differences caused by the mixing were found to be a decrease in the rise time of a few days, as well as a steeper decline of the lightcurve post-peak. By comparing the resulting light curves to observations of SNe Ib 1983I, 1983N and 1984L, it was found that extensive mixing of ^{56}Ni is necessary to explain the light curves. The same conclusion was reached for the light curve of Type IIb SN 1993J (Woosley et al. 1994; Shigeyama et al. 1994), with the added note that the mixing there also is restricted to the helium layers, leaving the outer hydrogen layer unmixed. Also when trying to reproduce nebular phase spectra, it is required that at least the five core zones are macroscopically mixed (Jerkstrand et al. 2015a; Dessart & Hillier 2020; Dessart et al. 2021).

In SNe, the physical process causing the macroscopic mixing is the Rayleigh-Taylor instability (Rayleigh 1882; Taylor 1950). This instability occurs once the initial shock wave passes through the interface between two different compositional layers. For SESNe,

the most important interface is that between the O/C and He/C layer. Once the shock hits the He/C layer, the expansion of the core is decelerated strongly, leading to a reverse shock. Between the reverse and forward shock, a pressure inversion occurs (pressure increases outward). Combining this with the steep density gradient at the interface, this leads to the emergence of an instability of the material between the shock waves, causing mixing of the different layers (Nagasawa et al. 1988; Shigeyama et al. 1990). This shock wave continues to grow until the forward shock reaches the surface, and a stabilising rarefaction wave is launched.

For SESNe, the relative importance of mixing is expected to increase with decreasing mass of the progenitor (Shigeyama et al. 1990). The physical explanation for this is that the helium envelope increases in relative size compared to the core for decreasing mass, which means that the pressure inversion is larger and that the instability can grow for longer, as the radius of the star is larger due to the larger envelope. These theoretical expectations were confirmed using 2D hydrodynamical simulations; Hachisu et al. (1991) found that for a progenitor of $M = 3.3\ M_{\odot}$, ^{56}Ni is mixed out to 0.4 $M_{\odot}$ below the surface (or 1.7 $M_{\odot}$ above the neutron star surface). For $M = 4.0\ M_{\odot}$ this decreases already to 1.6 $M_{\odot}$ below the surface (barely into the He/C layer which ends at 1.9 $M_{\odot}$), and for $M = 6.0$ $M_{\odot}$ the mixing is restricted purely to the core regions. Qualitatively similar results were obtained for simulations of Type IIb progenitors by Nomoto et al. (1995) and Iwamoto et al. (1997), as well as in 3D simulations of RSG and BSG progenitors (Wongwathanarat et al. 2015). It should be noted that in hydrogen-rich progenitors, it is instead the reverse shock originating between the the He- and H-layers that dominates the mixing.

For carbon and nitrogen specifically, it is of particular interest whether or not the He/C- and He/N-layers experience strong enough mixing to come close to the radioactive powering material. However, due to nitrogen not being part of the α-chain of elements, it is often omitted from mixing simulations (even in modern 3D simulations, e.g. Hammer et al. (2010) and Ono et al. 2020), leaving them without a distinction between the He/C and He/N layers. To this end, new mixing models including this distinction were simulated by our co-authors in **Paper I** (see section 3.1.2 in **Paper I**). In these models, it is found that even for the lowest mass model ($M = 3.3\ M_{\odot}$), the He/N zone experiences no significant mixing. For the He/C layer, 40% of its mass does get mixed into the completely mixed metal core, but this inmixing decreases quickly with mass, down to 18% for $M = 4.0\ M_{\odot}$. By this first detailed investigation of the mixing of C- and N-rich layers, we effectively

eliminated a free parameter in spectral modeling and are thus able to make much more accurate model spectra, in particular of C and N lines.

3.4 The Ni-bubble Effect

An additional process related to the macroscopic mixing of compositional zones that has been found to occur is the so-called "Ni-bubble" effect. During the first few days/weeks after the explosion, the radioactive decay of ^{56}Ni and ^{56}Co causes the Fe/He layers to expand relative to the other layers. The end result is that, while only containing a few percent of its mass, the Fe/He blobs/bubbles cover a few dozen percent of the volume in the macroscopically mixed core, making them comparatively low density while simultaneously increasing the density of the other core layers. This volume coverage fraction is in literature often called the 'filling factor' (a number between 0 and 1) of a particular compositional layer.

The Ni-bubble effect has been identified in hydrodynamical simulations of SNe (Herant & Benz 1991; Wang 2005; Gabler et al. 2021), as well as in supernova remnants (Hendrick et al. 2005). Besides these, observations of the optically thick line [Co II] 10.52 μm in SN 1987A were used to derive a filling factor of $f \gtrsim 0.3$ for the Fe/He layers (Chugai 1988a; Li et al. 1993), again indicating expansion through the Ni-bubble effect. In similar fashion, Jerkstrand et al. (2012) studied multiple optically thick MIR lines in Type IIP SN 2004et, finding $f \sim 0.15$ for these layers, whereas Ergon et al. (2015) found strong compression of the O-rich layers for SN 2011dh.

Based on these results, the spectral modeling community often parametrises the Ni-bubble effect in unmixed ejecta models (e.g. Mazzali et al. 2010; Jerkstrand et al. 2015a; Dessart et al. 2018; Liljegren et al. 2023), thereby altering the densities of the model ejecta layers, consequently having a large impact on the output model spectrum. An example of such an impact is the compression of the O/C layer, leading to increased CO formation (see discussion in **Paper III**). Interestingly enough, our studies of optically thick MIR Co lines in the Type Ic SN 2024aecx in **Paper III** yield a filling factor of only $f = 0.059^{+0.013}_{-0.012}$. For our best fit spectral models, this low filling factor is in fact consistent with a very weak or even completely absent Ni-bubble effect. We note that a weaker Ni-bubble effect in SESNe (compared to Type II SNe) was predicted by Dessart (2025), with SN 2024aecx providing the first proof of this hypothesis. With less than a handful of observed SNe

having well-determined Fe/He layer filling factors, this finding seriously challenges the common practice of assuming a significant Ni-bubble effect for spectral modeling.

4 The Supernova

With the shock-wave reaching the surface and the brightness increasing by multiple orders of magnitude, the SN event has truly begun. In this chapter, the event is followed from those earliest moments until the nebular phase. Section 4.1 introduces the reader to the history of SN research, as well as to the classification scheme that is used to distinguish between the different types of SNe. Section 4.2 tackles the evolution of the light curve and what this tells us about the powering of the SN. The spectral evolution during the photospheric and nebular phase are covered in Sections 4.3 and 4.4, respectively.

4.1 History and Classification

The history of humans observing SNe goes back two millenia in time. The first confirmed SN recorded occurred in 185 A.D., and was described in *The Book of Later Han* as a 'guest star', half the size of a bamboo mat, which disappeared within half a year. Other well documented examples include SN 1054, which produced the Crab Nebula, SN 1572 and SN 1604, which were observed and described in great detail by Tycho Brahe and Johannes Kepler, respectively.

The field commenced in earnest once the first spectroscopic observations became available. However, exactly what a SN was, remained unknown. Furthermore, the technology of the time required to observe spectra visually, i.e. without them being imprinted on photographic plates. In 1895, 10 years after the first extragalactic SN (SN 1885A) was observed, SN 1895B was discovered in NGC 5253. Referred to as 'the Harvard star', W.W. Campbel describes[1] its spectrum as follows:

"The spectrum of the Harvard star was continuous, though very peculiar. The maximum

[1]As cited in Minkowski (1939).

visual intensity was in the yellow-green, the green-blue was very faint, while the blue was surprisingly strong. In fact, the blue was very much brighter visually than the green-blue. The spectrum was relatively very faint from about λ 5200 to λ 4600. There was no trace of the nebular lines visible, nor of the Hβ line. There was some evidence of bright lines or of irregularities in the brightest portions of the spectrum, but the light was too weak to enable me to decide."

While technology progressed, progress on SNe was relatively slow. It was only in 1925 that SNe were first recognised as different from 'regular' novae (Lundmark 1925), and it took until after The Great Debate in the 1920s that the sheer distance to and amount of energy of SNe was realised, which led to the coinage of the term 'supernova' and the realisation that *"the phenomenon of a super-nova represents the transition of an ordinary star into a body of considerably smaller mass."* (Baade & Zwicky 1934). Under the 1940s, when the amount of spectroscopic observations started to increase, it was further realised that not all SNe look the same. In 1939, Minkowski still noted based on spectral series of five SNe that *"The following discussion of the spectra of former supernovae shows that, with the possible exception of S Andromedae, the spectra of all supernovae are similar and differ only in minor details."* (Minkowski 1939). Only two years later, a sample of 14 SNe led that same Minkowski to conclude that *"Spectroscopic observations indicate at least two types of supernovae"* (Minkowski 1941), which were dubbed Type I (no hydrogen lines) and Type II (broad hydrogen lines). Again, the further increase in the number of discovered SNe led to new classes being defined by multiple groups, most notably the Type III, IV and V SNe in Zwicky (1962) and Zwicky (1964) (classes that were eventually included in the Type II class).

In the current day, about a dozen of SN classes are identified. Type I SNe are only since $\sim$ 1985 recognised to be divided in multiple subclasses. The most common of these (80% of all SNe in a magnitude-limited sample (Li et al. 2011)) is the Type Ia, the original Type I, which is caused by a thermonuclear explosion of a WD, and is recognised in spectra by strong Si lines. The other Type I subclasses are Type Ib (He- but no Si-lines; Wheeler & Levreault 1985; Elias et al. 1985; Uomoto & Kirshner 1985), Type Ic (Neither He or Si lines; Wheeler et al. 1987) & Type Ic-BL (broad line). Type II SNe are subdivided into Type IIn (spectra with narrow lines; Schlegel 1990), Type II-L and Type II-P (based on whether their light curve shows a plateau or a linear decline; Barbon et al. 1979), and Type IIb (spectra that contain hydrogen lines initially, which disappear after a few

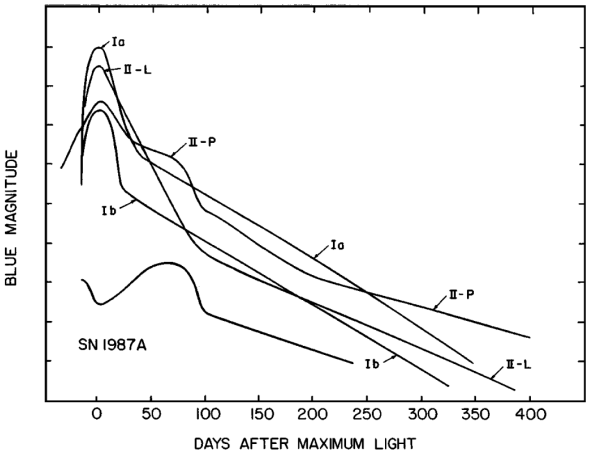

Figure 4.1: Schematic light curves of the different SN types. Note that Type Ib and Type Ic SNe have similar LC shapes, so that only Type Ib is included. When the figure was first published, Type IIb had not been recognised as a class yet. Figure 4.2 showcases a typical Type IIb LC. *Image credit: figure 3 in Filippenko (1997).*

weeks, so that the later spectra look exactly like Type Ib spectra Podsiadlowski et al. 1993; Filippenko et al. 1993; Nomoto et al. 1993). Recent additions to the above scheme are the Type Ibn (Pastorello et al. 2007, 2008), Type Icn (Fraser et al. 2021; Perley et al. 2022; Gal-Yam et al. 2022), and even a case of a Type Ien (Schulze et al. 2025) (spectra with narrow Si and S lines).

The classification scheme was canonised in Filippenko (1997), from which Figure 4.1 is reproduced here, showcasing the typical light curves for the different types. For the typical spectra, the reader is referred to Figure 4.3, reproduced from Vinkó et al. (2023).

4.2 Light curve

The light curve of a SN reveals through its shape what process powers it. For SESNe, the most important power source by far is the radioactive decay chain $^{56}\mathrm{Ni} \rightarrow {}^{56}\mathrm{Co} \rightarrow {}^{56}\mathrm{Fe}$. The way that this energy is deposited, leads to a light curve for a SESN (see Figure 4.2) that can typically be divided into two phases (three for Type IIb SNe; see later in this section).

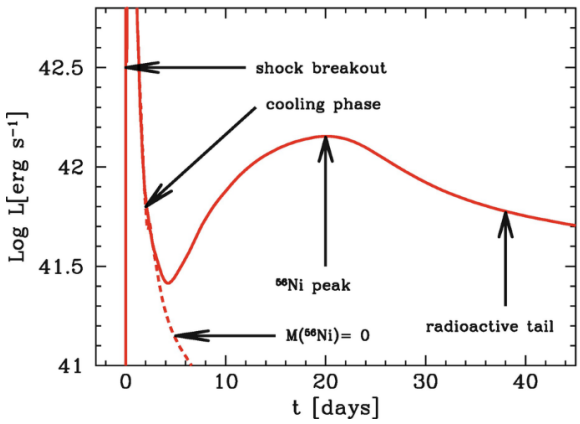

Figure 4.2: A model light curve of a SESN. The dashed line indicates the LC in case of no ^{56}Ni powering taking place. The shock breakout and shock cooling phases are representative of a Type IIb, with it being much shorter or totally absent in most Type Ib and Ic SNe. As mentioned in Section 4.2, the width and luminosity of the ^{56}Ni peak can be used to estimate key properties of the SN, such as $M_{\rm ej}$ and $M_{^{56}\rm Ni}$. *Image credit: figure 1 in Bersten & Mazzali (2017).*

The first of these is the diffusion phase, which can be subdivided in a rising and a declining phase. During the rising diffusion phase, the ejecta are still optically thick, so that the energy deposited in the explosion does not instantly come out as luminosity, but it takes some time for this energy to diffuse out and consequently be observable. This results in a light curve resembling a rising parabola in log luminosity, rising typically for some $\sim$ 15 – 30 days (Valenti et al. 2011; Taddia et al. 2015). However, by the time the peak is reached, the luminosity of radioactive decays has become dominant over the remaining energy from diffusion. From then on, a similar shaped declining diffusion phase sets in, where the powering is a blend of gamma-rays from ^{56}Ni and ^{56}Co.

The second phase of the light curve is often referred to as the radioactive tail, as the light curve now crosses an inflection point, where it changes from parabolic decline to approximately linear decline in log space. This linear decline has, at least in Type II SNe, a slope close to the exponential decay time of ^{56}Co, which during this phase is the dominant power source. In SESNe, the decline tends to be faster ($\sim$ 0.017 mag/d vs. 0.098 mag/d for ^{56}Co decay; see Prentice et al. 2019b), due to incomplete gamma-ray trapping (see later on in this section).

In some Type IIb SNe, there is an additional phase before the diffusion phase, which

is known as the shock breakout phase (again, see Figure 4.2). In these cases, its initially dominant source of luminosity is the heating of the progenitor's surface by the shock-wave (Schmidt et al. 1993). This burst of luminosity usually lasts too short for the peak to be observed, but the peak energy is so large ($\sim 5 \times 10^{44}$ erg s^{-1} (Ensman & Burrows 1992; Blinnikov et al. 2002), compared to the ^{56}Ni peak in Figure 4.2) that for some SNe the decline from this peak is observed before the eventual rise of the diffusion phase. The cooling of the shock-heated surface scales as $R_0/R(t)$ (with R_0 the radius at explosion), so that stars with larger R_0 (e.g. Type II SNe) will enjoy a longer burst of luminosity. The smaller radii of Type IIb progenitors ($\lesssim 200$ – $500\ R_\odot$ vs $\sim 1000\ R_\odot$ for Type II SNe) means that for most of them this power source is very short lived and is not observed in time. Some famous examples of Type IIb SNe where shock breakout was indeed observed are SN 1993J (the prototypical Type IIb (Woosley et al. 1994)), SN 2011dh (Arcavi et al. 2011; Ergon et al. 2015) and SN 2013df (Van Dyk et al. 2014).

The theory on lightcurve evolution as described above was of course not instantly realised. The accumulation of late time SN light curves led to the finding that many have an exponential tail (Baade 1945). Radioactivity seemed like the most probable cause, and in the 1950s multiple elements were proposed with half-lifes around 55 days, such as ^{7}Be (Borst 1950) and the exotic ^{254}Cf (Burbidge et al. 1956). ^{56}Ni and ^{56}Co were only proposed in 1969 (Colgate & McKee 1969), once it had shown up as the dominant end product of silicon burning in nucleosynthesis computations (Truran et al. 1967). The longer than observed half-life of 77 days for ^{56}Co is reconciled with observations once one realises that in many SNe, not all γ-rays are trapped in the ejecta[2], so that some escape without depositing energy, leading to faster observed decline times.

An analytical framework to describe the ^{56}Ni powered light curves which is still popular today was developed in the early 1980s by Arnett (1980) and Arnett (1982), i.e. even before the realisation that Type I SNe comprised of both thermonuclear SNe (Type Ia) and CCSNe (Type Ib and Type Ic). It can be considered as a cosmic irony that these two different explosion mechanisms result in light curves that are very similar and that can be described analytically in the same formalism. Using this analytical framework, key parameters of the SN may be obtained from both the peak luminosity and the light curve

[2]Indeed, the fraction of trapped γ rays goes down with time, see e.g. Fig. 1 in Jerkstrand et al. (2015a).

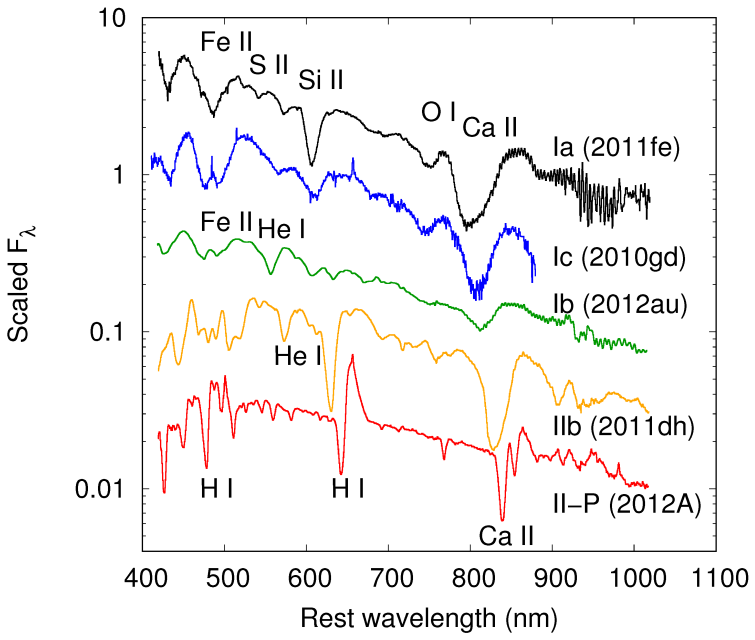

Figure 4.3: Photospheric spectra for five different types of SNe, taken around maximum light. The ions causing the strongest absorption features are indicated in the plot. Note how the location of the minimum of the Ca II feature shifts to redder wavelengths down the plot, indicating the successively lower velocities for the different types of SNe (as discussed in Section 4.3). In Paper I, we focus solely on Type Ib, Ic and IIb SNe. *Image credit: figure 1 in Vinkó et al. (2023).*

width. For SESNe, the short diffusion times due to the small ejecta masses mean that the entire luminosity at light curve peak may be assumed to come from the radioactive decay of ^{56}Ni and ^{56}Co, allowing for the direct determination of the mass of ^{56}Ni synthesised in the explosion (within a factor ~ 1.5, see Khatami & Kasen (2019)). The characteristic diffusion time Δt is in the Arnett-framework found to scale as $\propto E_{\rm exp}^{-1/4} M_{\rm ej}^{3/4} \kappa^{1/2}$. Estimating Δt from light curves, many studies provide estimates for $M_{\rm ej}$, using the weak dependency on explosion energy E and assuming that the opacity κ can be reasonably well estimated. Examples of recent works using this formalism to determine $M_{\rm ej}$ and $M_{^{56}\rm Ni}$ for SESNe include Richardson et al. (2006), Drout et al. (2011), Cano (2013), Prentice et al. (2016), Taddia et al. (2018), Barbarino et al. (2021) and Karamehmetoglu et al. (2023). It should however be noted that for SESNe, the assumption of constant κ is rather poor (Dessart

et al. 2016), and that varying its value within reasonable bounds may lead to values a factor 3 lower for $E_{\rm exp}$ and $M_{\rm ej}$ (Taddia et al. 2018). Therefore, estimates of these values with the Arnett framework should be taken with a grain of salt.

4.3 Photospheric Phase

The first few days after the supernova explosion, the ejecta are optically thick and the density is high enough to approximate the material by local thermodynamic equilibrium (LTE), meaning that there are sufficient collisions in the gas to maintain a Boltzmann distribution for the particle energies. For spectra, a Boltzmann distribution and optically thick conditions translate to a blackbody spectrum. By fitting a blackbody function to these early spectra (or, when available, to a Spectral Energy Distribution (SED) constructed from multi-band photometry), the photospheric temperature and radius of the ejecta can be determined (as was done in e.g. Arcavi et al. (2011), Ho et al. (2019), Gkini et al. (2024), among others).

Only a few days later, this blackbody is overlaid with lines of the most common elements in the SN envelope, i.e. hydrogen for Type IIb, helium for Type Ib and oxygen for Type Ic (see Figure 4.3). At this time, these lines have the shape of the classical P Cygni profile (McCrea 1929; Beals 1930) (named after the star P Cygni, in which it was first observed).

Analysing P Cygni profiles using a simplified framework known as the Schuster-Schwarzschild model (Schuster 1905; Schwarzschild 1906) or the two-flux approximation, from Figure 4.4 one can infer from a P Cygni line both the element that causes it (by comparing the rest-wavelength) and the velocity at which the photosphere of this element moves (by measuring the blueshift of the absorption minimum).

The main difficulty faced when performing this analysis in SNe is that, contrary to in e.g. the atmospheres of stars, the velocities of the ejecta are so high ($v \sim 1-2\times10^4$ km s^{-1} for the fastest material) that lines become broad enough to frequently blend with neighbouring lines. This results in complex combinations of P Cygni absorption and emission segments from different elements, superimposed on a time changing blackbody spectrum, so that it in most cases becomes difficult to determine how much of the line should be attributed to each element. One of the best examples of this difficulty is distinguishing low-velocity Si II λ6355 from high-velocity Hα, which complicates the distinction between

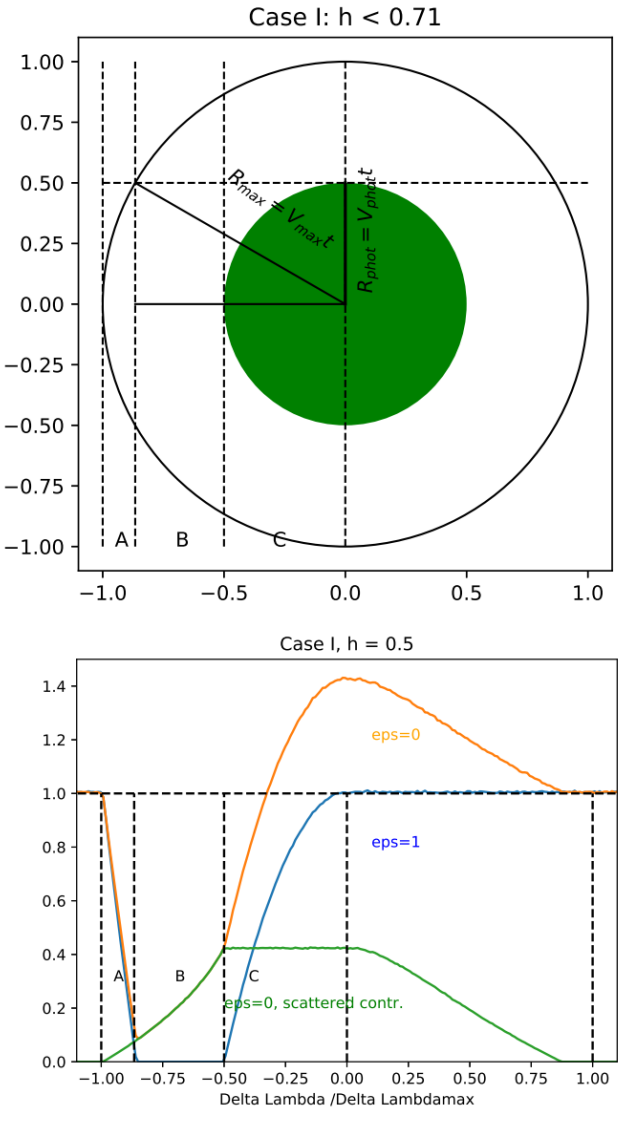

Figure 4.4: Schematic representation of P Cygni line formation (for more details, see Section 4.3). The top panel shows the outer gas shell in white and the photosphere in green. The observer is to the left of the plot. The bottom panel shows the line profile as seen by the observer, with blueshifted wavelengths to the left and redshifted to the right. For SNe, typical conditions are eps ~ 0, with 'eps' the probability of a photon being absorbed in an interaction). *Image credit: A. Jerkstrand.*

a Type IIb and Type Ib classification (Stritzinger et al. 2009; Liu et al. 2016). These problems become smaller once the SN reaches the nebular phase, in which the blackbody- and absorption components have disappeared.

4.4 Nebular Phase

With the supernova ejecta expanding continuously, the physical conditions inside change appreciably between $\sim$ 100 – 200 days after explosion. The decreasing density leads to fewer collisions, so that LTE no longer correctly describes most of the nebula. This leads to the disappearance of the aforementioned blackbody component of its spectrum. Furthermore, the decreasing density leads to less photoexcitations, photoionisations and the nebula becoming optically thin. Consequently, more and more atoms return to their ground states, also reducing the emission strength of most strong and quasi continuum lines. These two effects lead to the spectrum of the supernova becoming line dominated, with many of the strongest lines originating from (semi-) forbidden transitions (see e.g. Figure 4.5).

The physics behind how exactly these emission lines are formed, as well as what quantitative constraints one may obtain from their luminosities is discussed in its own chapter, namely Chapter 5. In the remainder of this subsection, the focus is specifically on more indirect relations between line luminosity and the ejecta/progenitor mass. The subsection is closed off with a consideration of line profiles.

4.4.1 Line Strengths

By far the most important parameter to determine when it comes to stars is their mass, as this value will directly influence their life span, luminosity, temperature, nucleosynthesis, and how they die. For stars that die with a supernova, the nebular phase is the optimal time for determining this mass. As mentioned above, during this phase the spectrum is dominated by isolated lines, allowing for much less ambiguous identifications than during the photospheric phase. The power of this, is that it becomes possible to determine the total power emitted by the single ion producing the line. Translating this energy to a mass and comparing it to results from detailed stellar evolution models then allows to determine the progenitor mass.

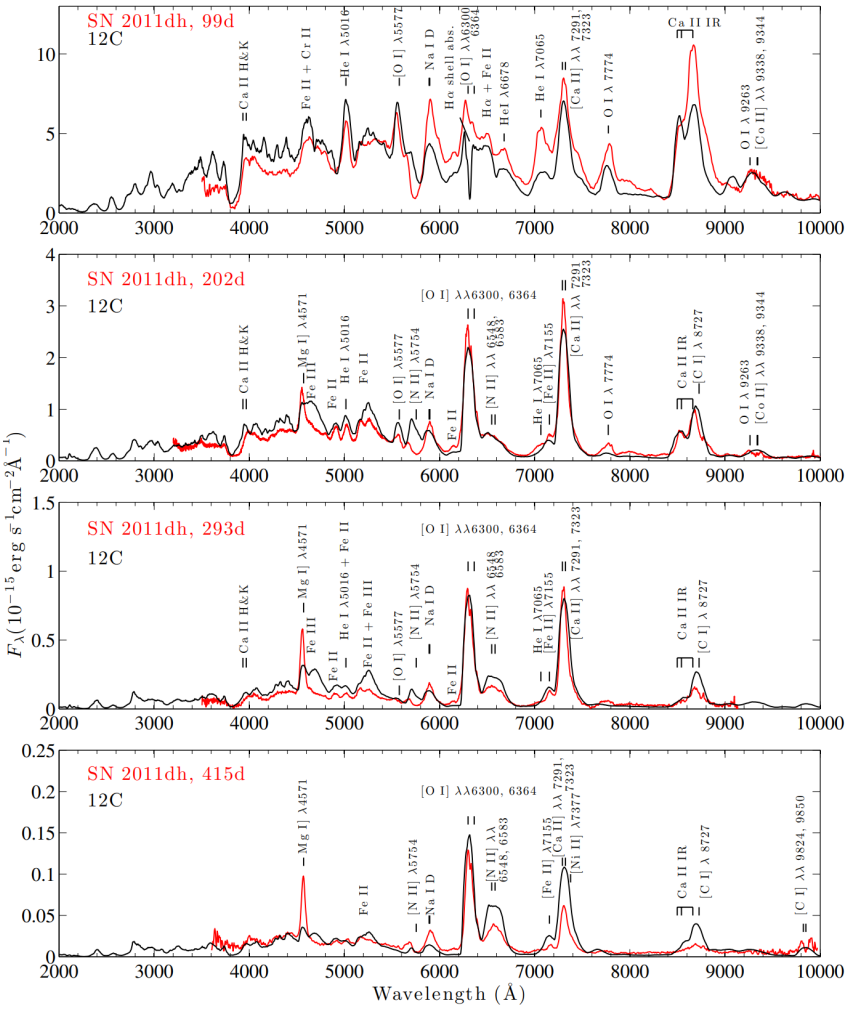

Figure 4.5: Spectral sequence of the Type IIb SN 2011dh (Ergon et al. 2015), evolving from the photospheric to the nebular phase. Each panel shows in red an epoch of SN 2011dh, starting at 99 days post explosion (end of the photospheric phase) and ending at 415 days post explosion (firmly in the nebular phase). In black, a model spectrum is shown for that epoch. Identified lines are indicated in each plot. From the last epoch, it becomes clear that the spectrum is line-dominated by mostly forbidden lines. *Image credit: figure 4 in Jerkstrand et al. (2015a).*

One of the first nebular phase diagnostics for progenitor mass was introduced in Fransson & Chevalier (1989), who found that the ratio [Ca II] $\lambda\lambda$7291, 7323 / [O I] $\lambda\lambda$6300, 6364 is strongly dependent on progenitor mass, and this fact has since then been used as an indication of said mass (Maeda et al. 2007; Pastorello et al. 2009). However, the authors already noted that mixing of calcium into oxygen-dominated zones may lead to calcium taking over much of the cooling, making the link of the ratio to progenitor mass less obvious. Additionally, the calcium is created in an explosively made region, introducing a dependency of the ratio on the explosion energy as well (Jerkstrand 2017).

A more recent but related diagnostic was provided by Jerkstrand et al. (2012) and Jerkstrand et al. (2014) (for Type II SNe; for SESNe, see Jerkstrand et al. (2015b)). Their diagnostic uses the fact that as the oxygen mass monotonically increases with the progenitor mass (Woosley & Weaver 1995), so does the total emission of [O I] $\lambda\lambda$6300, 6364 (Uomoto 1986). For each spectrum, they determine the quantity L_{norm} as defined in Equation 4.1.

$$L_{\mathrm{norm}}\left(t\right) = \frac{L_{\mathrm{line}}\left(t\right)}{1.06 \times 10^{42} \frac{M_{^{56}\mathrm{Ni}}}{0.075 M_{\odot}} \left(\mathrm{e}^{-t/111.4d} - \mathrm{e}^{-t/8.8d}\right) \mathrm{ergs}^{-1}} \tag{4.1}$$

With $L_{\mathrm{line}}\left(t\right)$ the integrated emission from [O I] $\lambda\lambda$6300, 6364. Comparing the L_{norm} curves through time for a given SN with a grid of spectral models, one can obtain an estimate for the progenitor mass. Figure 4.6 shows a comparison of SNe 1993J, 2008ax and 2011dh to a model grid, which among other things led the authors to discard the $M_{\mathrm{ZAMS}} = 17\ M_{\odot}$ model as being too massive to explain the observed [O I] $\lambda\lambda$6300, 6364 emission. This method has since been applied by many different groups (Fremling et al. 2014; Morales-Garoffolo et al. 2015; Valenti et al. 2016; Schweyer et al. 2023) and has become the main method for determining progenitor masses from nebular spectra up to this day.

Nonetheless, there are a few caveats also to this methodology. First of all, the fact that the diagnostic requires knowledge of the absolute [O I] $\lambda\lambda$6300, 6364 luminosity in erg s^{-1}, means that only properly flux-calibrated spectra can be used. As this is not a given for the majority of spectra, this narrows the applicable range of the diagnostic. Second, there are strong indications that molecules such as CO and SiO formed in oxygen-dominated zones can take over a significant part of the cooling which is otherwise done by [O I] $\lambda\lambda$6300, 6364 (Liu & Dalgarno 1995; Liljegren et al. 2020, 2023), reducing the emission from [O I]

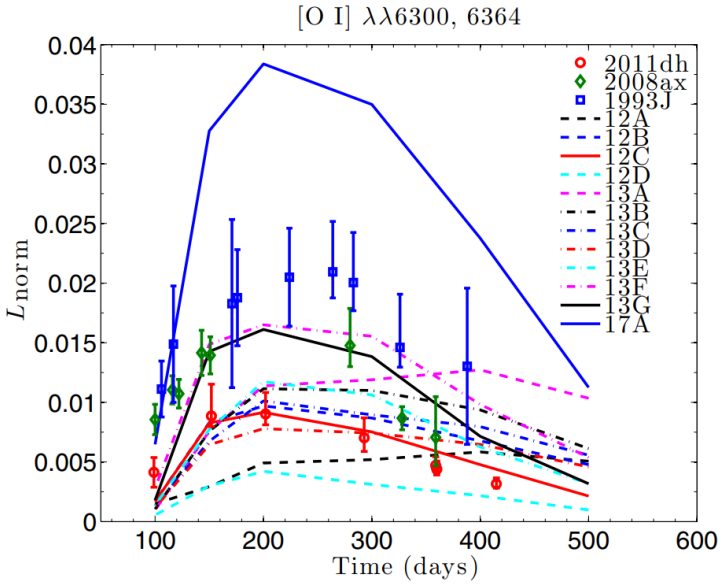

Figure 4.6: Model $L_{\rm norm}$ curves for the model grid in Jerkstrand et al. (2015a). The observations of SNe 2011dh, 2008ax and 1993J are indicated by circles, diamonds and squares, respectively. While the 17A model ($M_{\rm ZAMS} = 17 M_{\odot}$) is clearly separated, the models for $M_{\rm ZAMS} = 12$ and 13 $M_{\odot}$ show overlap. This overlap is caused by different settings for the treatment of e.g. molecules and mixing. In Paper I, we were able to constrain the mixing with dedicated models (see section 3.1.2 in paper I), and molecules are known to not play a role (see Section 4.4.1). *Image credit: figure 15 in Jerkstrand et al. (2015a).*

$\lambda\lambda$6300, 6364 and making the mappings from emission to mass made in Jerkstrand et al. (2015a) much less trivial (as they themselves also noted, see their section 7.4).

The [N II] $\lambda\lambda$6548, 6583 diagnostic ($f_{\rm [N\,II]}$) presented in **Paper I** does not suffer from these aforementioned difficulties. This diagnostic is defined as a ratio of luminosities rather than an absolute luminosity, so that no accurate flux calibration or extinction corrections are necessary. Furthermore, formation of molecules containing nitrogen is negligible during the nebular phase (Liljegren et al. 2023). Other strengths of the diagnostic include that the nitrogen emission originates from a single compositional zone (the He/N zone), and that nitrogen is almost exclusively present in its singly ionised form N II (Paper I, Jerkstrand et al. 2015a; Dessart et al. 2021), so that the modeled emission is robust to the ionisation balance (as opposed to e.g. Mg I] λ4571 (Jerkstrand et al. 2015a)). This is not to say that

the $f_{[\mathrm{N\,II}]}$ diagnostic is perfect. Its main caveat is the uncertainty in mass-loss strength of the SN-progenitors and thus how much of the He/N envelope remains at explosion (see Section 2.2). Furthermore, it is found that the progenitor mass range to which it is sensitive is limited to below $\sim 5\ M_{\odot}$, so that it can not be used for the highest mass SESNe.

In any case, the paragraphs in this subsection show that the existing progenitor mass diagnostics are not as trivial and unambiguous as they may seem at first glance. Combined with the paramount importance of progenitor mass for understanding the stellar evolution before the supernova, it is clear that studying the potential of [N II] $\lambda\lambda$6548, 6583 as a new progenitor mass diagnostic, as was done in **Paper I**, is a useful undertaking.

4.4.2 Line Profiles

The second use of the isolated lines is in analysis of the line profiles. The line width and shape gives information on the velocity distribution of the material emitting the line, which may be used to determine which elements are in what locations in the ejecta. If an element is unmixed and only resides in the outer layer of the ejecta, resembling a thin or thick shell, one would expect the line profile to be flat topped. If on the other hand, the element is fully mixed, emitting from a uniform sphere, a parabolic shape is expected. A schematic representation of line profiles from six example ejecta distributions is given in Figure 4.7.

An early example of a line profile study was the study of line widths by Fransson & Chevalier (1989). They found that Mg I] λ4571, [O I] $\lambda\lambda$6300, 6364 and [Ca II] $\lambda\lambda$7291, 7323 usually have similar observed line widths, despite originating from different compositional zones. This fact forms a strong argument for the theory that the five core compositional zones (as defined in Section 2.1, see also Section 3.3 and Figure 2.1) are macroscopically mixed.

Later on, the asymmetry observed in line profiles of various types of SNe proved to be a smoking gun for understanding that aspherical explosions are common (Modjaz et al. 2008; Maeda et al. 2008; van Baal et al. 2023). This was essential information, as the breaking of spherical symmetry turned out to be decisive for simulating successful explosions with the neutrino-heating mechanism (Janka (2012); see Section 3.1.3).

Another example of a study of line profiles is that performed by Fang et al. (2024).

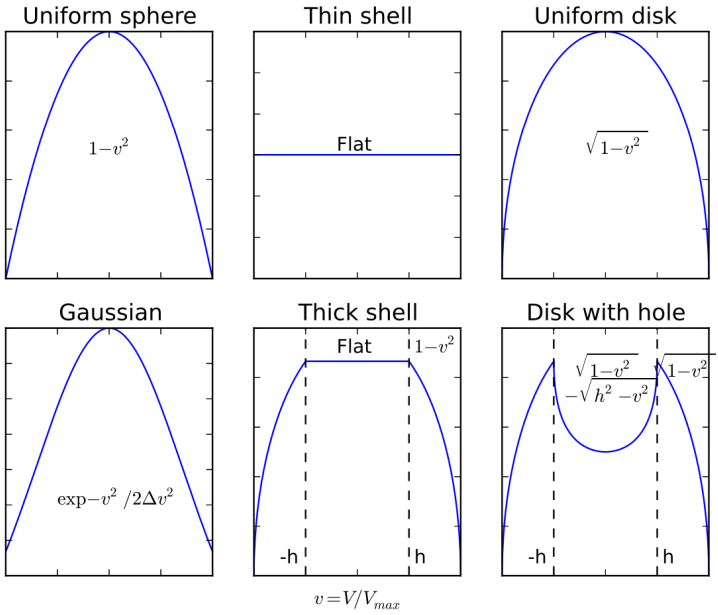

Figure 4.7: Six different theoretical line profiles for nebular supernova spectra. In Paper I, we allowed the line profiles to be modeled with either Gaussian or thin shell profiles, with Gaussians being the most common. Note that these line profiles all assume spherically symmetric ejecta. *Image credit: figure 2 in Jerkstrand (2017).*

Here, the authors studied a sample of 80 SESNe, focusing on whether the line profiles of [O I] $\lambda\lambda$6300, 6364 and [Ca II] $\lambda\lambda$7291, 7323 consisted of a single peak or a double peak (indicating an aspherical explosion). They find that 41 objects have both single peaked [O I] and [Ca II], while the other 39 have one of the two as a single peak and the other as a double. From this study, one can learn that a) half of the SESNe resulted from asymmetric explosions and b) there is an anti-correlation in the spatial distribution of the layers emitting [O I] and those emitting [Ca II].

As a final example, our study of carbon line profiles in **Paper II** can be considered. As already alluded to in Fransson & Chevalier (1989), the carbon present in the mostly unmixed He/C layer leads to carbon lines in spectral models being slightly broader than lines that solely form in the macroscopically mixed core. However, the extent, mass and relative abundances of the He/C layer vary significantly between stellar evolution models (see Section 2.1.2), depending on assumptions made in the stellar evolution code. A study

of carbon line widths in observed SNe may thus provide important constraints for these codes. In **Paper II** we performed such a study on the line width of [C I] $\lambda\lambda$9824, 9850, and for some SNe we find that carbon line widths are consistent with smaller He/C zones than present in the Woosley (2019) + Ertl et al. (2020) stellar evolution models. Our sample of [C I] $\lambda\lambda$9824, 9850 observations is however currently too small to draw any general conclusions, so that we encourage targeted observing campaigns of this line specifically.

4.5 Beyond the Optical: SNe in the NIR and MIR

So far, all discussion of the SN spectra has been restricted to the optical wavelength regimes ($0.3 \lesssim \lambda \lesssim 1.0$ μm). However, the advent of the JWST (Gardner et al. 2023) has strongly revived interest in the spectral regions redward of the optical, i.e. the NIR and MIR wavelength ranges ($1.0 \lesssim \lambda \lesssim 30$ μm). In this subsection, I will discuss some important physical processes influencing the SN spectrum in these wavelength ranges.

4.5.1 Molecules

The continued cooling of the SN ejecta with time eventually allows for the formation of molecules during the nebular phase. Through their countless rotational and vibrational transitions, these molecules cool the surrounding ejecta very efficiently. While emitting mostly in IR wavelengths, they thus also influence all other wavelength regimes. The formation of molecules was first observed in SN 1987A (Aitken et al. 1988; Catchpole et al. 1988; Rank et al. 1988; Spyromilio et al. 1988; Meikle et al. 1989), and has since then been observed in dozens of SNe (see Table 1 in Matsuura 2017), forming about 100 – 200 days post explosion, with the earliest signatures as early as $\sim$ 50 d (Drout et al. 2016; Banerjee et al. 2018; Shrestha et al. 2026).

The most commonly formed and observed molecule is CO. It is usually identified through its first overtone emission around 2.3 μm (just within the typical range of earth-based spectrographs with $\lambda \lesssim 2.5$ μm), but its strongest emission is in the fundamental band, typically observed between $\sim$ 4.3 to 5.5 μm. CO is mostly formed in the inner parts of the O/C layer, with the increasing He abundance in the outer parts of the zone inhibiting molecule formation (Liu et al. 1992; Liu & Dalgarno 1995; Liljegren et al. 2020)). Through its strong cooling properties, CO formation in the O/C layer directly influences

emission from carbon in the optical wavelength ranges, which was the main topic of study in **Paper II**. Recent work by Liljegren et al. (2023) has shown that the CO mass formed is roughly linearly dependent on the density of the surrounding material. For spectral modeling, this means that accurate treatment of the Ni-bubble effect (see Section 3.4), which directly sets the O/C zone density, is of utmost importance for obtaining accurate estimates of the CO mass formed. In Liljegren et al. (2023), the authors studied molecule formation for a Type Ic model assuming overdensities $\chi = 50 - 800$, compatible with overdensities studied in Type IIb models by Jerkstrand et al. (2015a) ($\chi = 30 - 210$). For these overdensities, Liljegren et al. (2023) find $\sim 10^{-4} - 10^{-3}$ $M_{\odot}$ of CO to have formed by 150 days post explosion. In their spectral models, they find the lower end of this range to match the luminosity in the first overtone for e.g. Type IIb SN 2011dh and Type Ic SN 2007gr. Interestingly, as already mentioned in Section 3.4, we obtain a much lower overdensity of $\chi = 1 - 3$ for the Type Ic SN 2024aecx in **Paper III**, and we are able to match the luminosity in the fundamental band with only $\sim 5 \times 10^{-6}$ $M_{\odot}$ at 167 d post explosion. While the sample size is still small, these findings suggest that there might be a large range of molecule masses formed in SNe, even within a single class (e.g. the Type Ic class in this case).

After CO, SiO is the most detected molecule. With only strong emission in the MIR at 8.0 and 4.1 μm (fundamental- and first overtone bands, respectively), it has however been more difficult to detect than CO. In SN 1987A, the disappearance of SiO was almost coincidental with the appearance of thermal dust emission, which has been interpreted as the SiO having condensed into dust (Wooden et al. 1993).

4.5.2 Dust

Once the ejecta have cooled even further, down to the 1000 – 2000 K range, dust grains can start to form. Just as molecules, these dust grains in SNe emit mostly in the MIR, typically showing up as a thermal blackbody peaking at a few hundreds of K. Besides forming in the ejecta, dust may also form in the collision of the ejecta with a CSM, or have already been present prior to explosion (Matsuura 2017).

One of the main effects of dust formation on SNe is in the lightcurve; about 500 days since the explosion SN 1987A, the optical lightcurve suddenly declined much faster than expected from ^{56}Co and ^{57}Co decay (Whitelock et al. 1989), coincidental with the

disappearance of SiO emission mentioned in the previous section. This has since been interpreted as the formation of optically thick dust, shifting the emission from the optical to the IR wavelengths. A second effect is on the spectra; with the photons in red wings of optical spectral lines now being blocked by dust, these lines become blueshifted (Lucy et al. 1989).

4.5.3 Ejecta

Compared to the optical wavelength range, emission from the SN ejecta in the NIR and especially MIR is even less blended and more dominated by a handful of strong emission lines. Most of these strongest lines are M1-forbidden transitions within the ground multiplets of ions. These transitions therefore have low upper level energies ($E_u \lesssim 0.2$ eV), and they have low critical electron densities, meaning that they are well approximated by an LTE approximation. The details on the implications of these properties are discussed extensively in Chapter 5, but in short, these NIR and MIR transitions can provide elemental masses, emission volumes, zone temperatures and ionisation fractions with much smaller uncertainties than most optical lines. We show this in **Paper III** by analysing the MIR JWST spectrum for Type Ic SN 2024aecx, obtaining e.g. tight constraints on the masses of Cl, Ar, radioactive ^{56}Ni and stable Ni.

5 Line Formation Theory

During the nebular phase, the amount of spectral lines in the supernova spectrum with significant optical depth or large luminosities drops drastically. This leads to a transition from a quasi-continuum of hundreds of blended spectral lines to a spectrum dominated by at most a few dozen, mostly isolated emission lines. In the nebular phase then, it becomes possible to more securely identify each individual spectral line, and perhaps more importantly, to measure its luminosity. From these line luminosity measurements, one can obtain a wealth of information on the elements present in the supernova ejecta, as well as on its structure. Examples of constraints one may obtain are masses of ions, electron temperatures and emission volumes. Multiple of these constraints may be combined to also obtain ionisation fractions and densities. All this information can be used to further our understanding of, among other things, nucleosynthesis in massive stars, explosion physics and galactic chemical evolution.

In this chapter, the necessary theory for obtaining the aforementioned constraints is discussed. Let us begin at the beginning: where do spectral lines come from?

5.1 Atomic Structure

In supernovae, the ejecta are full of electrons. These electrons can be either moving freely through the ejecta, or they can be 'bound' to an ion. In the case that they are bound, they populate distinct energy levels within this atom. When an electron changes from one energy level to another, the energy difference between these two levels is thus always the same value, so that the photon being absorbed or emitted always has the same exact

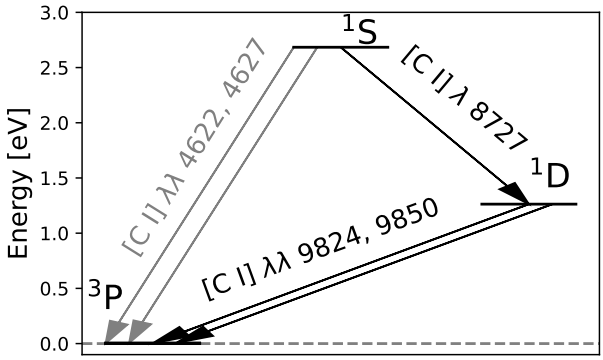

Figure 5.1: A Grotrian diagram for the first five levels in neutral carbon, the atom investigated in **Paper II**. Each horizontal line represents an energy level, with lines between levels indicating transitions. As the ground state is a triplet (not visible due to small energy separation), transitions connecting to it are multiplets. Transitions connected to one of the triplet states are so weak that they are not indicated.

wavelength, giving rise to an absorption or emission line, respectively[1]

Each ion has a unique set of energy levels (see e.g. Figure 5.1), so that they have their own spectral 'fingerprint'.

There are many ways through which a bound electron can change the energy level it occupies. Examples include the spontaneous or stimulated emission of a photon, collision with a free electron, and in some cases even collisions with free protons. Besides changing energy level, the bound electron may also be freed from its parent ion completely, in which case we speak of either photoionisation or electron impact ionisation, or a free electron may bind with an ion, known as recombination. All these processes occur simultaneously throughout the expanding supernova ejecta, resulting in a population distribution for the different states in a given ion. Finding the equilibrium between all these processes and the resulting level-populations is one of the key outputs that an NLTE spectral synthesis code provides. However, for certain physical regimes, finding the population distribution is greatly simplified and can be done analytically.

[1]Due to e.g. Heisenberg's uncertainty principle, this energy difference has some uncertainty related to it, so that in fact these lines have a non-zero width (natural broadening) around the centroid wavelength. In SNe, these broadening processes (also inlcuding e.g. pressure broadening and thermal broadening) result in widths orders of magnitude smaller than line widths due to the expansion of the SN ejecta, so that they are ignored in the remainder of this work

5.1.1 Local Thermodynamic Equilibrium

For the early phases ($t \lesssim$ a few hundred days) of supernovae, there are typically only two atomic processes that dominate the rates for populating levels in ions; these are spontaneous emission and electron collisions. Examples of exceptions include levels in ions experiencing a large recombination inflow (e.g. Ni I and Co I in SN 2024aecx; see **Paper III**), as well as high-lying levels excited by non-thermal electrons in e.g. He I (Dessart et al. 2021). In case collisions are dominant, the amount of electrons in a given level, N_i, is given by Maxwell-Boltzmann statistics as

$$N_i = N_{\text{ion}} \frac{g_i}{Z(T)} e^{-E_i/kT}, \tag{5.1}$$

Where g_i is the upper level's statistical weight, E_i is the upper level's energy above the ground state, and $Z(T)$ is the partition function ($Z(T) = \sum_i g_i e^{-E_i/kT}$). In this regime, which can be valid for an entire ion or for a subset of its levels (typically the lowest energy levels), we speak of Local Thermodynamic Equilibrium. In LTE, knowing the level population thus only requires knowing the local temperature, greatly simplifying calculations.

To know whether a given atomic level is in LTE, one can consider the competition between spontaneous emission and collisions. In the literature (e.g. Jerkstrand 2017; Simotas et al. 2025; Jacobson-Galán et al. 2026), it is typically the competition for the specific transition (rather than all transitions to the upper level in question) that is considered. In this case, for a transition from upper level u to lower level l, the spontaneous emission rate is given by $A_{ul}\beta_{S,ul}$, and the collision rate is given by $Q_{ul}n_e$, with $Q_{ul} = 8.6 \times 10^{-6}\Upsilon_{ul}/(T^{1/2}g_u)$ (Osterbrock & Ferland 2006), where $\Upsilon_{ul} = \Upsilon_{lu}$ is the effective collision strength[2]. One can then define a critical electron density where these two rates are equal as

$$n_{e,\text{crit}} = \frac{A_{ul}\beta_S}{Q_{ul}}. \tag{5.2}$$

In case $n_e \gg n_{e,\text{crit}}$, collisions dominate and the level population is given by Equation 5.1. The reader is cautioned to take the requirement $n_e \gg n_{e,\text{crit}}$ strictly. In **Paper III**, we show that the departure coefficient $b \equiv N_i/N_i^{\text{LTE}}$ behaves roughly as $n_e/(n_e + n_{e,\text{crit}})$.

[2]While effective collision strengths do have temperature dependence, this is usually $\lesssim 10\%$ over the temperature range relevant for SNe, so that we in the remainder of this work will assume them to be temperature independent.

For example, if $n_e = 2n_{e,\mathrm{crit}}$, Equation 5.1 would overestimate N_i by a factor $1/b = 1.5$, translating to an overestimate in ion mass of 50% (see Section 5.2.1).

Now, Equation 5.2 only considers two out of the typically dozens of radiative and collisional transitions connected to the given energy level. In **Paper III**, we provide a formalism where we consider almost all these transitions, while simultaneously retaining the analytic nature of estimating $n_{e,\mathrm{crit}}$ that makes it a much less expensive estimate than a full NLTE spectral model.

5.1.2 Optical Depth

The concept of optical depth is well understood through different types of clouds; some clouds or mist are partially see-through, with some light from behind still reaching your eyes, whereas others completely block all light from the sky above. These two clouds have different optical depths; the first has a low optical depth and can be said to be optically thin, while the latter has a high optical depth and is optically thick. Just as for clouds, transitions in ions have optical depth.

It was shown by Sobolev (1957) that for a homologously expanding medium (such as a supernova), the optical depth τ_S of a transition is given by

$$\tau_S = \frac{1}{8\pi}\frac{g_u}{g_l}A\lambda^3 n_l \left(1 - \frac{g_l}{g_u}\frac{n_u}{n_l}\right) t. \tag{5.3}$$

Here, n_u and n_l are the number densities of the upper and lower levels, A is the Einstein coefficient and t is the time since explosion. Assuming that photons from the transition meet no other optically thick lines, the fraction of emitted photons that escapes the nebula and reaches the observer is given by $\beta_S = \frac{1-e^{-\tau_S}}{\tau_S}$, with the remaining photons being self-absorbed.

5.2 Line Luminosity

In words, the luminosity of an emission line from a given ion is simply the number of electrons in the transition's upper level (N_u), multiplied with the transition's energy ($E = h\nu = hc/\lambda$), the rate of this transition occurring spontaneously (the Einstein coefficient A), and the fraction of photons escaping the ejecta ($\beta_S = \frac{1-e^{-\tau_S}}{\tau_S}$). In formulaic form,

$$L = N_u \frac{hc}{\lambda} A \beta_S. \tag{5.4}$$

While generally true, this description of the luminosity does not yet allow us to infer too much useful information. To increase its usefulness, we can study some particular regimes.

5.2.1 LTE

Arguably the most useful regime is the LTE regime, in which the populating and depopulating processes of the upper level of the transition are dominated by collisions (see Section 5.1.1). Writing the amount of particles in this ion N_{ion} as $N_{\text{ion}} = M_{\text{ion}}/\mu m_p$ (with μ the atom's atomic weight), we can rewrite Equation 5.4 using 5.1 into

$$L = \frac{hc}{m_p} \times \frac{A g_u}{\lambda \mu} \times \frac{M_{\text{ion}}}{Z(T)} e^{-E_u/kT} \beta_S, \tag{5.5}$$

where we have rearranged and gathered all natural constants in the first term, all transition specific constants in the second term, and finally the variables in the third term. From Equation 5.5, we can now further simplify by considering two extremes for β_S; the optically thin and optically thick regimes. In **Paper III**, we provide so-called line regime plots (LRP) from which one can learn whether a given emission line at a given epoch is in LTE or NLTE, and whether it is optically thick or optically thin. We created such LRPs for 18 MIR lines typically seen in nebular spectra of CCSNe, of which an example is reproduced in Figure 5.2.

Optically Thin LTE

In the regime where the Sobolev optical depth $\tau_S \ll 1$, β_S asymptotes to 1, so that Equation 5.5 simply becomes

$$L = \frac{hc}{m_p} \times \frac{A g_u}{\lambda \mu} \times \frac{M_{\text{ion}}}{Z(T)} e^{-E_u/kT}. \tag{5.6}$$

In this optically thin, LTE regime, the line's luminosity is thus only dependent on the electron temperature T and the mass of the ion, M_{ion}, from which the line originates. In other words, in case one has an estimate for the temperature, one can directly infer the mass of the ion in question in the SN ejecta. Alternatively, for those transitions

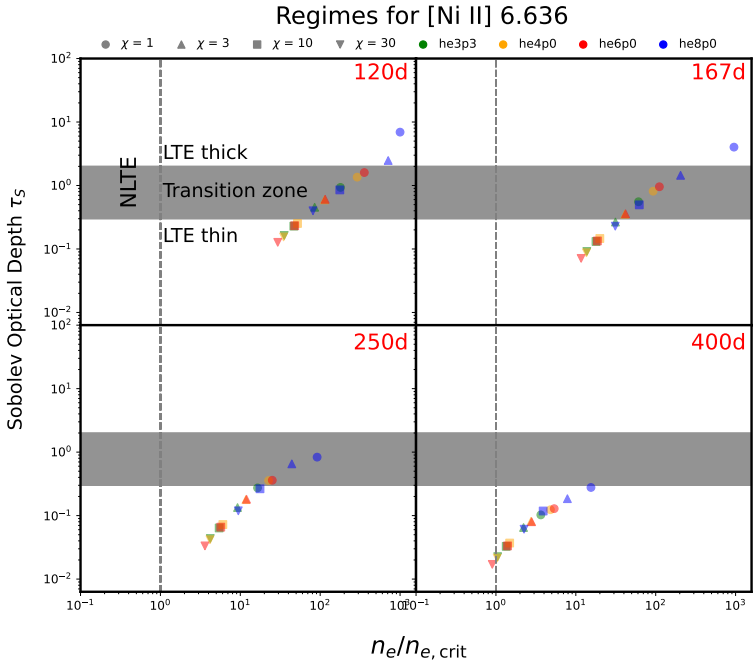

Figure 5.2: Reproduction of the Line Regime Plot (LRP) for [Ni II] 6.636 μm form **Paper III**. Inspired by figures in Jerkstrand et al. (2025), it presents the Sobolev optical depth τ_S and the ratio between current and critical electron densities, $n_e/n_{e,crit}$, for a grid of helium star models of different masses and different Ni-bubble strengths. For visual purposes, $n_e/n_{e,crit} > 1000$ was set to 1000.

where $E_u \ll kT^3$, the temperature dependence of Equation 5.6 becomes weak enough to obtain $M_{\rm ion}$ without a narrow temperature estimate. This is assuming that $Z(T)$ has a weak temperature dependence. In general, ions with few low-lying energy levels (typically light elements with large electron affinity) have temperature dependencies $\lesssim 1\%$ for temperatures relevant in SNe. Ions with many low-lying multiplets (typically heavier elements) may have appreciable temperature dependencies; for example, the difference in $Z(T)$ for Ni I for $T = 3000$ K and $T = 5000$ K is $\sim 15\%$.

In **Paper III**, we identify and study many transitions with $E_u < kT$ in SN 2024aecx.

[3]For SESN ejecta, typical temperatures at 200 d post explosion are $T = 3000 - 5000$ K in the inner zones, i.e. $kT = 0.26 - 0.43$ eV. For weak temperature dependence, one thus ideally has $E_u \lesssim 0.2$ eV, or lines with $\lambda > 6\,\mu$m.

These transitions are typically intra-multiplet transitions in the ground states of ions, showing up at near- and mid infrared wavelengths $3\,\mu m \lesssim \lambda \lesssim 30\,\mu m$. In **Paper II**, we instead study two optically thin lines from excited states ($E_u = 1.26$ and 2.68 eV) in C I. To obtain a mass estimate for these lines, we there used the luminosity of both lines in tandem to obtain the necessary temperature estimate: from Equation 5.6, the luminosity ratio of two LTE, optically thin lines from the same ion becomes

$$\frac{L_1}{L_2} = \frac{A_1 \lambda_2 g_{u,1}}{A_2 \lambda_1 g_{u,2}} e^{-(E_{u,1}-E_{u,2})/kT}, \tag{5.7}$$

so that rearranging for T, we find

$$T = \ln\left(\frac{A_1 \lambda_2 g_{u,1}}{A_2 \lambda_1 g_{u,2}}\right) / \ln\left(\frac{L_1}{L_2}\right) \times \frac{(E_{u,2} - E_{u,1})}{k}. \tag{5.8}$$

The power of isolated, optically thin LTE lines in SN spectra can not be overstated. As we have shown, they allow in many cases to directly obtain ion mass estimates from luminosity measurements which, either assuming it is the dominant ion (which can be informed using spectral models, see Chapter 6) or by combining mass estimates of different ionisation stages of the same atom (as done in e.g. **Paper III** for Ni and Co), yield estimates of the elemental masses in the ejecta. These elemental masses can be directly compared to stellar evolution and explosion models to learn how well these models can reproduce observed SNe, as well as where crucial ingredients are missing. As an example, we show in **Paper III** that the mass of chlorine in SN 2024aecx is a factor a few larger (in line with earlier results for SN 1987A (Aitken et al. 1988) and the SNR Cassiopeia A (XRISM Collaboration et al. 2026)) than what is produced in a grid of helium stars (believed to progenitors of SESNe like SN 2024aecx) by Woosley (2019) and Ertl et al. (2020), suggesting that these models lack some physical process (e.g. shell mergers) that would enhance Cl production.

Optically Thick LTE

Moving on to the optically thick regime ($\tau_S \gg 1$), β_S asymptotes to $1/\tau_S$. In this case, Equation 5.5 is rewritten via Equation 5.3 to

$$L = \frac{8\pi hc}{\lambda^4 t} \frac{V_{\rm emit}}{e^{(E_u - E_l)/kT} - 1}, \tag{5.9}$$

with $V_{\rm emit}$ the emitting volume. This emitting volume is defined as the fraction of a macroscopically mixed (see Section 3.3) sphere filled with material from a particular compositional zone. Defined as $V_{\rm emit} \equiv \frac{4\pi}{3}(vt)^3 \times f$, Equation 5.9 becomes

$$L = \frac{32\pi^2 hc}{3\lambda^4} \times v^3 t^2 \times \frac{f}{e^{(E_u - E_l)/kT} - 1}. \tag{5.10}$$

$$= \frac{16\pi^2}{3c} \times v^3 t^2 f \times \lambda B_\lambda(T) \tag{5.11}$$

Here, v is the expansion velocity of the sphere, f is the so-called filling factor and $B_\lambda(T)$ is the blackbody function. With the time post-explosion typically well constrained and the expansion velocity obtainable directly from the width of the emission line profiles, Equation 5.10 again only has two unknowns: the filling factor f and the temperature T. Temperature dependence is typically stronger than for Equation 5.6; for those lines with $E_u - E_l = \frac{hc}{\lambda} \ll kT$, $L \propto f \times T$, i.e. the temperature dependence is always at least linear.

In many cases, this close to linear dependence is sufficient to be able to obtain useful constraints on the filling factor f of compositional zones. These filling factors can be directly translated to the zone densities, providing useful information to the modeling of the supernova explosion itself. Furthermore, the density is one of the most important variables for NLTE spectral codes, directly influencing the model temperatures and ionisation fractions, as well as line optical depths, so obtaining a zone's filling factor provides a great constraint on modeling the SN spectrum.

An example of an optically thick LTE line is [Ne II] 12.81 μm; in **Paper III** we show that the line is securely in optically thick LTE in helium star explosions until at least t = 275 d post explosion, and we are able to obtain an estimate of $f_{\rm ONeMg}$ (the filling factor of the zone of C-burning ashes) of 0.24 ± 0.07 for SN 2024aecx. [Ne II] 12.81 μm has earlier been identified in e.g. SN 2004et (Kotak et al. 2009) and SN 2024ggi (Dessart et al. 2025). In the modeling paper by Dessart (2025), it was also consistently found to be one of the strongest lines in CCSNe in the MIR range, and it was also suggested to be a diagnostic of ejecta- and consequently progenitor mass. We note that as long as [Ne II] 12.81 μm is optically thick, as is clear from Equation 5.10, this diagnostic is not a direct one. However, in the models of Woosley (2019) and Ertl et al. (2020), $f_{\rm ONeMg}$ is found to increase with ejecta mass, such that $L_{\rm [Ne\,II]\,12.81\,\mu m}$ indirectly traces the ejecta mass. When [Ne II] 12.81 μm is in the optically thin LTE regime, the fact that Ne II is not the

dominant ion ($x_{\mathrm{Ne\,II}} \lesssim 0.2$ for our models in **Paper III**) complicates the extraction of a total Ne mass and consequently of linking it to an ejecta and progenitor mass.

Partially Thick LTE

Of course, not all lines do at all epochs neatly fall into the optically thin or optically thick category. As luminosities of these lines are more difficult to interpret, they are often treated with a grain of salt, or worse, optical thinness is assumed anyway, leading to ion mass underestimates of factor a few (see e.g. the discussion in Section 6 in Jerkstrand et al. 2015c). These lines may carry essential information however, in specific cases. Let us consider such a case.

Starting from Equations 5.5 and 5.1, the luminosity ratio of two emission lines, in LTE, in the same zone (i.e. $T_1 = T_2$, $V_{emit,1} = V_{emit,2}$) is given by

$$\frac{L_1}{L_2} = \frac{A_1 g_1 \lambda_2 \mu_2}{A_2 g_2 \lambda_1 \mu_1} \frac{Z_2(T)}{Z_1(T)} \exp\left(-\frac{E_{u,1} + E_{u,2}}{kT}\right) \frac{M_{\mathrm{ion},1}}{M_{\mathrm{ion},2}} \frac{\tau_2}{\tau_1} \frac{1 - e^{-\tau_1}}{1 - e^{-\tau_2}}. \tag{5.12}$$

While this equation does not deserve any prizes for its beauty, it can be made a lot more neat once one plugs in the expression for $\frac{\tau_2}{\tau_1}$. From Equation 5.3, again for two LTE lines from the same zone, we find

$$\frac{\tau_2}{\tau_1} \equiv R(T) = \frac{A_2 g_{u,2} \lambda_2^3 \mu_1}{A_1 g_{u,1} \lambda_1^3 \mu_2} \frac{Z_1(T)}{Z_2(T)} \frac{M_{\mathrm{ion},2}}{M_{\mathrm{ion},1}} \times \frac{\exp\left(\frac{-E_{l,2}}{kT}\right) - \exp\left(\frac{-E_{u,2}}{kT}\right)}{\exp\left(\frac{-E_{l,1}}{kT}\right) - \exp\left(\frac{-E_{u,1}}{kT}\right)}. \tag{5.13}$$

Plugging in Equation 5.13 into Equation 5.12, many terms cancel to result in

$$\frac{L_1}{L_2} = \left(\frac{\lambda_2}{\lambda_1}\right)^4 \frac{\exp(\Delta E_2/kT) - 1}{\exp(\Delta E_1/kT) - 1} \frac{1 - \exp(-R\tau_2)}{1 - \exp(-\tau_2)}, \tag{5.14}$$

Where have written $\Delta E = E_u - E_l$ and $\tau_1 = R\tau_2$. The behaviour of L_1/L_2 is made most clear with an example. In **Paper III**, we studied the ratio $L_{[\mathrm{Ni\,II}]\,6.636\,\mu\mathrm{m}}/L_{[\mathrm{Co\,II}]\,10.52\,\mu\mathrm{m}}$ as a function of $\tau_{[\mathrm{Ni\,II}]\,6.636\,\mu\mathrm{m}}$, as shown in Figure 5.3.

As both lines have $\Delta E \lesssim kT$, the behaviour of L_1/L_2 is clearly only weakly dependent on temperature. The only remaining dependence is then on $M_{\mathrm{Ni\,II}}/M_{\mathrm{Co\,II}}$ (or Ni/Fe as in the example, as $x_{\mathrm{Ni\,II}}/x_{\mathrm{Co\,II}}$ was well constrained), which is captured in the three subpanels. While the line ratio approaches the same constant for all Ni/Fe values for

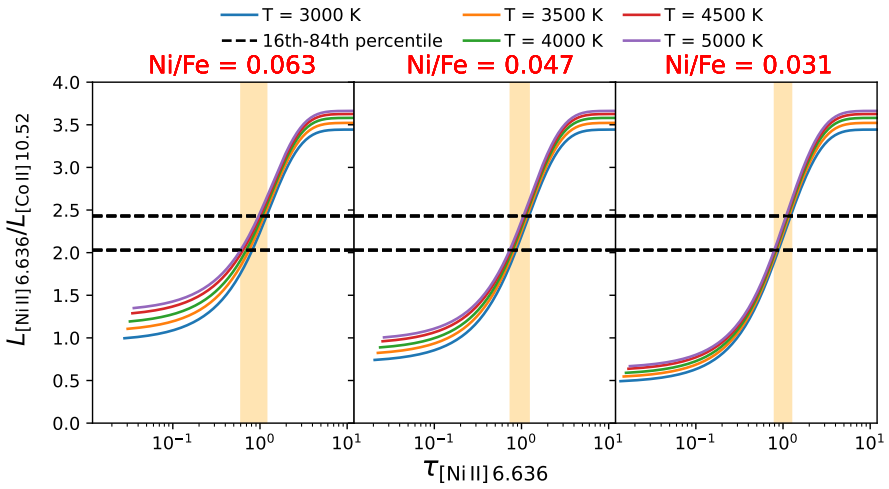

Figure 5.3: A reproduction of Figure 14 from **Paper III**: The theoretical luminosity ratio $L_{[\mathrm{Ni\ II}]\ 6.636\ \mu\mathrm{m}}/L_{[\mathrm{Co\ II}]\ 10.52\ \mu\mathrm{m}}$ as a function of $\tau_{[\mathrm{Ni\,II}]\,6.636\,\mu\mathrm{m}}$, for different temperatures and three cases of the Ni/Fe ratio. The 16th – 84th percentile bounds on the observed $L_{[\mathrm{Ni\ II}]\ 6.636\ \mu\mathrm{m}}/L_{[\mathrm{Co\ II}]\ 10.52\ \mu\mathrm{m}}$ ratio for SN 2024aecx are shown in horizontal, black dashed lines. For all three cases, $\tau_{[\mathrm{Ni\,II}]\,6.636\,\mu\mathrm{m}}$ is tightly constrained by the observed ratio, with the allowed range indicated in orange.

the $\tau_{[\mathrm{Ni\,II}]\,6.636\,\mu\mathrm{m}} \gg 1$ regime (as expected from Equation 5.10), we observe an increase in the $L_{[\mathrm{Ni\,II}]\,6.636\,\mu\mathrm{m}}/L_{[\mathrm{Co\,II}]\,10.52\,\mu\mathrm{m}}$ ratio in the $\tau_{[\mathrm{Ni\,II}]\,6.636\,\mu\mathrm{m}} \ll 1$ regime for increasing Ni/Fe for a given temperature. This fact alone allowed us to put an upper limit on Ni/Fe, as at some point, $L_{[\mathrm{Ni\,II}]\,6.636\,\mu\mathrm{m}}/L_{[\mathrm{Co\,II}]\,10.52\,\mu\mathrm{m}}$ would remain above the observed ratio even when $\tau_{[\mathrm{Ni\,II}]\,6.636\,\mu\mathrm{m}} \ll 1$. What we further obtained was a tight constraint on $\tau_{[\mathrm{Ni\,II}]\,6.636\,\mu\mathrm{m}}$, revealing that this line has an optical depth of ~ 1 and allowing us to thereby still obtain an estimate of $M_{\mathrm{Ni\,II}}$. Lastly, through $\tau_1 = R\tau_2$, we could prove that $\tau_{[\mathrm{Co\,II}]\,10.52\,\mu\mathrm{m}} \gg 1$, so that we could use this line securely in the optically thick regime and obtain the filling factor of the Fe-rich zone.

In summary, the ratio of two lines with optical depths typically close to unity provided us the necessary information for obtaining $M_{\mathrm{Ni\,II}}$, f_{FeHe} and thereby indirectly for obtaining Ni/Fe in SN 2024aecx, making this line ratio a powerful tool, especially for MIR lines with $\Delta E \lesssim kT$.

5.2.2 NLTE

For those cases where the level is not predominantly populated *and* depopulated by collisions (i.e. when $n_e \lesssim n_{e,\mathrm{crit}}$), obtaining the upper level's population is not as straight forward and thus requires detailed NLTE spectral modeling efforts (see Chapter 6). Nonetheless, these lines may in specific cases be used in tandem with other lines to obtain useful constraints analytically.

As an example, we can consider a level that is predominantly populated by thermal collisions. Assuming that these populations predominantly originate from a 'feeder' level, then the rate of population P_{uf} is given by

$$P_{uf} = N_f Q_{uf}(T) \frac{g_u}{g_f} e^{-(E_u - E_f)/kT} n_e. \tag{5.15}$$

Assuming furthermore that only radiative decays and collisional decays to a single lower state l (which may or may not be the same level as f) occur, the rate of depopulation D_{ul} becomes

$$D_{ul} = N_u (A_{ul}\beta_{S,ul} + Q_{ul}(T) n_e). \tag{5.16}$$

In statistical equilibrium, we have $P_{uf} = D_{ul}$, and assuming $n_e \ll n_{e,crit}$ (and thus $Q_{ul}(T)n_e \ll A_{ul}\beta_{S,ul}$), we obtain when combining with Equation 5.4 that the luminosity for such a line is given by

$$L = \frac{hc}{m_p} \times \frac{g_u}{g_f \lambda \mu} \times M_f Q_{uf}(T) e^{-(E_u - E_f)/kT} n_e. \tag{5.17}$$

Thus, the luminosity becomes dependent on M_f, T and n_e. If one has a luminosity ratio for two lines from the same feeder state (i.e. M_f and n_e are the same), one can thus obtain the temperature of the zone where the line is formed. This scenario is most likely to occur in late nebular phases ($t \sim 1000$ days). The reason for this is best understood through an example, e.g. [O I] $\lambda\lambda$6300, 6364 and [O I] λ5577, from the first ($i = 2$) and second ($i = 3$) excited states in O I. The effective collision strength Υ_{32} is larger than Υ_{31} ($i = 1$ being the ground multiplet). It follows then from Equation 5.15 that, as long as $i = 2$ is in LTE, $P_{32} > P_{31}$, so that $i = 3$ has a different feeding state (namely $i = 2$) than the feeding state of $i = 2$ (namely $i = 1$, the ground multiplet). The only way to obtain $P_{32} \ll P_{31}$, i.e. for both to have the ground state as dominant feeding state, would be to

have $N_2 \ll N_2^{LTE}$. At $n_{e,crit} \sim 3 \times 10^6$ cm^{-3}, for the upper level of [O I] $\lambda\lambda$6300, 6364 ($i = 2$) to be out of LTE and thus in the $n_e \ll n_{e,crit}$ regime, we thus need to wait for n_e to decrease below a few times 10^5 cm^{-3}. For reference, the $\chi = 1$ model set in **Paper III** (our models with the least dense oxygen zones) has $n_e \sim 5 \times 10^5 - 3 \times 10^6$ cm^{-3} at 400 d (our latest epoch). This scenario as in O I, with two strong lines from the first and second excited states and $\Upsilon_{32} > \Upsilon_{31}$, is common in multiple other ions with strong nebular lines, e.g. N II and C I.

6 Modeling Supernova Spectra

In this chapter, I discuss how one creates a model spectrum of a SN. Section 6.1 briefly describes the initial modeling efforts that initiated the field. Section 6.2 presents the basic ingredients and assumptions necessary for the spectral modeling code, whereas Section 6.3 discusses `SUMO`, the code used in **Paper I, II and III**, in more detail.

6.1 History

The first efforts to model SN spectra in the nebular phase commenced around 1980. Initially, these efforts were limited to modeling a handful of atoms with one or two ionisation stages each, in a one-zone approach (i.e. the composition throughout the ejecta is assumed to be uniform). Meyerott (1980) modelled late time emission from Fe II and Fe III and obtained relatively good agreement with Type Ia (or, at the time, Type I) nebular spectra. In that same year, Axelrod (1980) modeled nebular phase spectra for Type I SNe using six ions, namely Fe I, Fe II, Fe III, Co I, Co II and Co III. Comparing the models to Type Ia SN 1972E, he provided strong support for ^{56}Ni and ^{56}Co as the main power sources of Type I SNe, while at the same time putting a requirement of 0.3 to 1.0 $M_{\odot}$ of ^{56}Ni in the ejecta and noting that this is "uncomfortably large" for the core collapse model. Chugai (1988b) focused on Type II nebular spectra, modeling only the three lines Lyα, Mg II λ2800 and [O I] λ6300. Because of these relatively simple models, it was initially more common to compare with observed spectra by presenting tabulated line ratios of important emission lines, rather than visually comparing the spectra over the entire wavelength range.

In Fransson & Chevalier (1989) such visual model spectra were indeed produced (see Figure 6.1) by simulating the emission from the explosion of multi-zone helium stars from Woosley & Weaver (1988). While looking somewhat primitive for today's standards (compare to e.g. Figure 4.5), comparison to spectra of the Type Ib SN 1985F (Filippenko

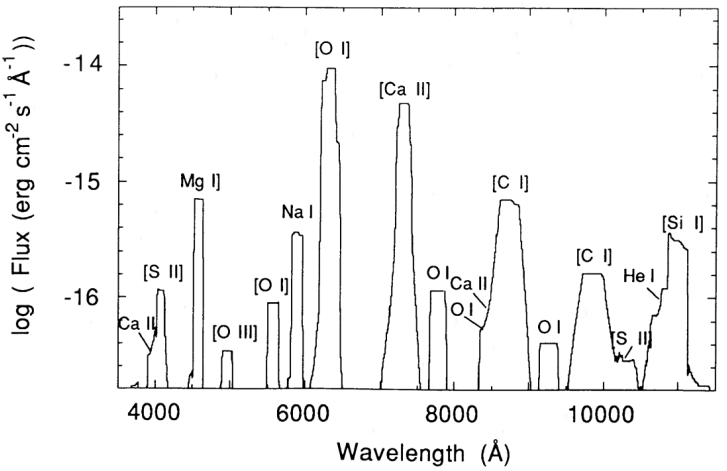

Figure 6.1: Model spectrum for an 8 $M_\odot$ helium core at 300 days after explosion (Fransson & Chevalier 1989). The authors note that the line profiles are too flat topped due to the fact that their stellar models have kept the onion shell structure intact, putting the material of each element at a too narrow velocity range. The code used for spectral modeling in Paper I, `SUMO`, solves this issue through complete macroscopic mixing in the core (see Section 3.3). *Image credit: figure 12 in Fransson & Chevalier (1989).*

& Sargent 1986; Gaskell et al. 1986) allowed them to determine that SNe of low-mass ($M \sim 4\ M_\odot$) helium cores could not reproduce the observed spectra, and that the progenitor must thus have been a high-mass helium core ($M \sim 8\ M_\odot$). Furthermore, it was argued that the ratio between the luminosity of the [Ca II] $\lambda\lambda$7291, 7323 and [O I] $\lambda\lambda$6300, 6364 lines may be used as a diagnostic for the progenitor mass (see Section 4.4.1).

In the following years, the steady increase in computing power allowed the expressed wish from Fransson & Chevalier (1989)[1] to become reality. Today, a handful of NLTE spectral modeling codes are in use and under active development, including but not limited to `SUMO` (Jerkstrand 2011; Jerkstrand et al. 2012, 2014), the 3D code `EXTRASS` (Jerkstrand et al. 2020; van Baal et al. 2023, 2024), `CMFGEN` (Hillier & Miller 1998; Dessart & Hillier 2010; Hillier & Dessart 2012), `JEKYLL` (Ergon et al. 2018; Ergon & Fransson 2022), `ARTIS` (Sim 2007; Kromer & Sim 2009; Shingles et al. 2020) and the code used in Mazzali et al. (2001) and Mazzali et al. (2007). As already mentioned in Section 4.4, these codes are

[1] *"We think that the results here show that it will be feasible in the future to understand the nucleosynthetic process of massive stars from the late spectra".*

being used, among other things, to estimate progenitor masses, explosion morphologies and temperature- and ionisation structures for many different types of SNe. A code comparison paper comparing these as well as other SN radiative transfer codes on a few test cases was published by Blondin et al. (2022).

6.2 Creating a Model Spectrum

Each of the codes mentioned above takes as input a model for the composition, the mass- and the velocity distribution of the star at some time after explosion (as provided in e.g. Woosley (2019)), and outputs an estimate of the spectrum at a requested epoch. Here, a quick overview is given of the main physical processes calculated by the codes on the way from input to output. For a comprehensive overview of which codes use which assumptions and methods to implement these processes, the reader is referred to chapter 5 in Jerkstrand (2017) or to Blondin et al. (2022).

6.2.1 Energy Deposition

The first step is to distribute the radioactive energy from the ^{56}Ni $\rightarrow$ ^{56}Co $\rightarrow$ ^{56}Fe chain that powers the SN during the nebular phase. This comes mostly in the form of $\sim$ MeV gamma-rays ($\sim$ 97%), with some contribution of positrons ($\sim$ 3%; e.g. Jerkstrand 2011). The gamma-rays lose their energy mainly by Compton scattering, which is modeled well with transfer with a simple grey opacity $\kappa_\gamma = 0.03 \times (Y_e/0.5)$ cm^2 g^{-1} (Colgate et al. 1980). Minor channels include pair production (requiring $E > 1.022$ MeV) and photoabsorption (important for $E < 0.1$ MeV, but see Section 6.2.2). The positrons lose their energy through collisions with both free and bound electrons, but at a much higher effective opacity of $\kappa_{e^+} = 10$ cm^2 g^{-1} (Colgate et al. 1980). It is because of this higher opacity that the $\sim$ 3% of energy in positrons is essential for nebular phase modeling: at some point, so many gamma-rays will have escaped already that positrons become the dominant energy source. Under typical conditions, this occurs for SESNe somewhere between 250 to 900 days post-explosion (Jerkstrand 2017).

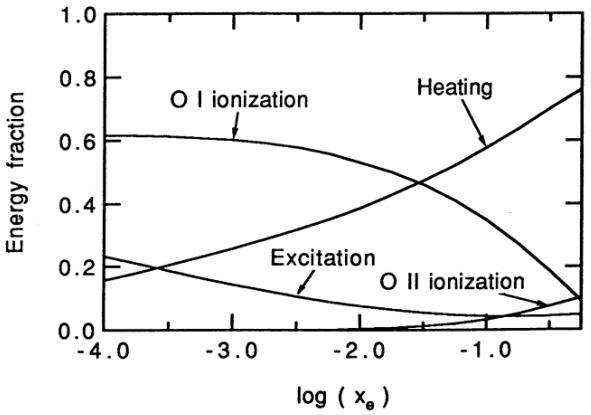

Figure 6.2: Plot showing the part of the energy from non-thermal electrons going into the ionisation, excitation and heating for a pure oxygen nebula. *Image credit: figure 4 in Kozma & Fransson (1992).*

6.2.2 Non-thermal Processes

The downscattered gamma-rays will eventually be photoabsorbed once they obtain energies below $\sim$ 0.1 MeV. The electrons doing the photoabsorbing here will themselves obtain high energies ($\sim$ 0.01 – 1 MeV). They deposit this energy through three channels: ionisation (leading to *secondary* electrons with $E \sim 10 - 100$ eV), excitation, and collisions with free, thermal electrons (known as *heating*). Which part goes through which channel can be determined if the degradation spectrum (the amount of electrons per energy bin) is known. This degredation spectrum can be calculated by solving the Spencer-Fano equation (Spencer & Fano 1954). Methodology to solving the equation is provided in Kozma & Fransson (1992). For typical ejecta, the most important free parameters are the free electron fraction x_e and the chemical composition. As can be seen in Figure 6.2, the majority of the energy of non-thermal electrons goes into ionisation for low x_e, while most goes into heating when $x_e > 0.1$.

6.2.3 Level Populations

The first instinct of many physicists when it comes to determining ionisation and excitation balances will be to turn to the Saha- and Boltzmann equations, which only require the

knowledge of the temperature. However, the low density environment in the nebular phase of an SN means that LTE, which is the key requirement for the Saha and Boltzmann equations to hold, is no longer a valid approximation[2]. Instead, the rates of change $\frac{dn_{ijk}}{dt}$ from every single level k in ionisation state j of atom i to every other level in that atom (and to other atoms i in the case of radioactive decay) need to be determined (see Equation 6.1, which is equation 67 in Jerkstrand (2017)).

$$\frac{dn_{ijk}}{dt} - \frac{n_{ijk}}{\rho}\frac{d\rho}{dt} = \sum_{i'}\sum_{j'}\sum_{k'} n_{i'j'k'} R_{i'j'k',ijk} - n_{ijk}\sum_{i'}\sum_{j'}\sum_{k'} R_{ijk,i'j'k'} \tag{6.1}$$

To calculate $\frac{dn_{ijk}}{dt}$, one needs to know the reaction rates R that contain all possible mechanisms to change level, i.e. excitation, de-excitation, ionisation, recombination and charge transfer. To be able to simulate enough levels for realistic spectra ($\mathcal{O}(10^2)$), simplifying assumptions are a necessity. The two most important of these are a) excited, non-metastable states can only de-excite (the transition rates A are too fast to allow any other process), so $R_{ionisation} = R_{recombination} = R_{excitation} = 0$ and b) ground states experience no ionisation by thermal electrons, nor recombination by 3-body reactions, as the temperature in SNe are too low for this to occur. Furthermore, 'steady state' is assumed, meaning that the time-derivatives in Equation 6.1 are set to 0.

6.2.4 Temperature Structure

Temperature is a key quantity to correctly determine the energy budget within the supernova. It is calculated by solving the first law of thermodynamics (assuming homologous expansion ($R(t) = vt$) and ideal monoatomic gas pressure; see Equation 6.2), which can be done if one knows the heating and cooling rates $H(T)$ and $C(T)$ (Jerkstrand 2011).

$$\frac{dT(t)}{dt} = \frac{H(T) - C(T)}{\frac{3}{2}kn(t)} - \frac{2T(t)}{t} - \frac{T(t)}{1 + x_e(t)}\frac{dx_e(t)}{dt} \tag{6.2}$$

Of these, the heating in the SN is typically dominated by non-thermal processes (see Section 6.2.2), while cooling occurs mostly through collisional excitation and then line emission[3]. These rates are dependent on the level populations, once more showing the cou-

[2]To clarify, it is treating the full ion as being in LTE that is no longer valid; as discussed in Chapter 5, individual levels in the ion may still be in LTE with the ground multiplet, even in the nebular phase.

[3]Once temperatures are low enough to form molecules, they have been shown to strongly increase cooling (Liu & Dalgarno 1995; Liljegren et al. 2020).

pling involved in producing a final spectrum. Work by de Kool et al. (1998) and Fransson & Chevalier (1989) has shown that the *thermal equilibrium approximation*, $H(T) = C(T)$, holds for up to $\sim$ 600 – 800 days post explosion, at least for models of SN 1987A. Finding the temperature at which this equation holds is the value that the code will try to converge upon.

6.2.5 Radiative Transfer

For the spectrum to reach the observer, the emitted photons first have to travel through the supernova and across the universe into the instrument, while avoiding being diverted or destroyed on the way. This journey is governed by radiative transfer. The classical way of calculating this is by solving the transfer equation (See Equation 6.3) iteratively, which says that the intensity of a beam of radiation I_ν along a path s will gain intensity through emission (η_ν, e.g. photons from de-exciting electrons), loses it through absorption ($\chi_{\nu,a}$), and redistributes it through scattering ($\chi_{\nu,s}$).

$$\left[\frac{1}{c}\frac{\partial}{\partial t} + \frac{\partial}{\partial s}\right] I_\nu(\mathbf{x}, \mathbf{n}, t) = \eta_\nu(\mathbf{x}, \mathbf{n}, t) - (\chi_{\nu,s}(\mathbf{x}, \mathbf{n}, t) + \chi_{\nu,a}(\mathbf{x}, \mathbf{n}, t))I_\nu(\mathbf{x}, \mathbf{n}, t) \tag{6.3}$$

This way requires solving large systems of coupled equations, and becomes intractably large when going to more than one dimension (Hillier & Dessart 2012). Another way to do radiative transfer trying to circumvent this problem is via the Monte Carlo approach. In this approach, instead of solving a transfer equation, large numbers of 'photon packets' are followed on their journey through the ejecta. Whether they interact along the way is determined by drawing random numbers, with interactions of higher optical depth having a higher probability of interaction. The Monte Carlo approach has become more popular in recent years (see e.g. Blondin et al. 2022), as the increase in computing power made simulating large enough amounts of photon packets more feasible. In **Paper II**, we create a lightweight radiative transfer code (dubbed CaNARY) using such a Monte Carlo approach. This code solves for the radiative transfer of six spectral lines in the Ca NIR triplet wavelength range, with the goal of obtaining estimates of the [C I] λ8727 luminosity from Ca NIR profiles in observed SNe.

6.3 SUMO

As all the spectral models in **Papers I, II and III** were created using the SUMO code (Jerkstrand 2011; Jerkstrand et al. 2012, 2014), it warrants its own section. SUMO is a Monte Carlo radiative transfer code operating in NLTE. The major assumptions on which the code is built are spherical symmetry (i.e. the code is in 1D), the Sobolev approximation, and instant photon travel between points. The Sobolev approximation (Sobolev 1957) in practice means that a photon only interacts with a line once in a specific point on its way out of the nebula. If it passes through, it never faces this line again. This assumption is valid in SNe, as the velocity gradient of the material in the SN is much larger than the thermal line width of the line. Whereas many codes use this approximation to construct effective expansion opacity for photons, SUMO stands out as it treats the transfer line by line. Furthermore, it is one of only a few codes that has a full non-LTE treatment of excitation and ionisation structure.

SUMO starts a run by depositing the radioactive energy into the nebula. It considers energy in the form of gamma-rays, positrons, electrons and X-rays as emitted by ^{56}Ni, ^{56}Co, ^{57}Co and ^{44}Ti. The deposition of energy through gamma-rays and positrons is treated with grey-opacities. Once the energy input has been deposited, the code solves for the physical conditions in the nebula through an iterative scheme using the Newton-Raphson method (see e.g. Press et al. 1992). As initial conditions for excitation and ionisation structure, LTE solutions through the Saha and Boltzmann equations are used. Each iteration involves executing the following routines:

1. suse, which calculates temperatures, excitation structure of the atoms and emissivities, keeping ionisation structure and radiative terms fixed.

2. sumo, which runs a Monte Carlo simulation of the photons making up the radiation field, keeping temperatures, excitation and ionisation structure fixed.

3. suib, which calculates the ionisation structure, keeping temperatures, excitation structure and radiative terms fixed.

This loop is continued until the calculated relative step is less than 1% for all routines.

7 The Role of Supernovae in Galactic Chemical Evolution

Throughout the universe's evolution, the initial H, He and Li present right after the Big Bang have been slowly transforming into all other elements in the periodic table through a multitude of nucleosynthesis sites. In this Chapter, I will briefly zoom in on the role played in this process by SNe in particular.

It was in the now seminal work of Burbidge et al. (1957) that the relative abundances of the elements observed in the universe were attributed to nucleosynthesis in stars throughout the universe's history, rather than to a primordial state of the universe (Alpher et al. 1948; Mayer & Teller 1949). Already then it was recognised that SNe contribute significantly to this nucleosynthesis, despite only the Type I and Type II distinction being established and the power source being thought to be ^{254}Cf rather than ^{56}Ni. Early efforts to understand the relative contributions of different nucleosynthesis sites include Truran & Cameron (1971), who through, as they put it, some 'extremely speculative assumptions', could among other things set a lower limit on stars that experience CCSNe of ~ 4 $M_{\odot}$, as well as predict a supernova rate of about one in every 25 years in the MW. These early efforts were hampered by a lack of per element nucleosynthesis models, so that for example all elements from C to Fe were considered as a single nucleosynthesis product (see Figure 7.1). With the arrival of extensive nucleosynthesis model grids for SNe (Woosley & Weaver 1995), Timmes et al. (1995) were for the first time able to reproduce observed elemental abundances for almost all elements up to Ca within a factor of two. Elements up to Zn were reproduced within a factor a few, owing to larger uncertainties in the mostly explosive nature of the nucleosynthesis of these elements. Another important result was the determination of the ratio of the Type Ia to CCSN rates, which was found to be between 1/6 and 1/5. This result has been recovered by more recent GCE models of e.g.

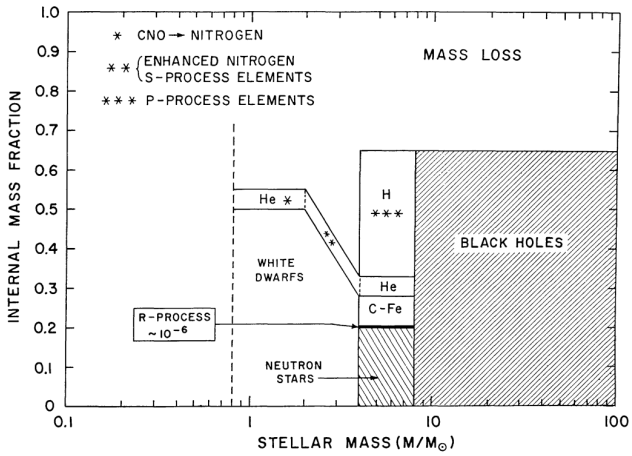

Figure 7.1: A figure showcasing the nucleosynthesis assumptions for stars of different masses in an early GCE model. *Image credit: figure 1 in Truran & Cameron (1971).*

Sukhbold et al. (2016), with a somewhat larger fraction of $\sim 2/5$ found in volume-limited observational studies (Ma et al. 2025).

The current state of the field of galactic chemical evolution calculations is the work by Kobayashi et al. (2020). Here, the authors model the elements from carbon to uranium, investigating the relative contributions from AGB stars, CCSNe, Type Ia SNe and neutron star mergers. Their figure 39 is reproduced here as Figure 7.2. Already at first sight, it is clear that SNe are one of the most prominent sites for nucleosynthesis in the universe. While this may be expected for the elements up to the iron peak, which are produced through 'simple' fusion in their cores (and eventually through explosive nucleosynthesis, see Section 3.2), it is found that even the heavier elements outside of the three s-process peaks (elements surrounding Sr, La and Pb) are primarily made by CCSNe; the weak s-process elements (Cu up to Rb) are produced in the convective He-burning core and the convective C-burning shell (Pignatari et al. 2010; Käppeler et al. 2011), while heavier r-process elements are formed in hypernovae (CCSNe with high explosion energies of $E \gtrsim 10^{52}$ erg, observed as Type Ic-BL SNe) or magneto-rotational SNe (rapidly rotating progenitors with strong magnetic fields, potentially related to hypernovae) (Cescutti et al. 2015; Haynes & Kobayashi 2019; Yong et al. 2021). The latter finding is a debated one; BH-NS and NS-NS mergers have been identified as a site for r-process nucleosynthesis

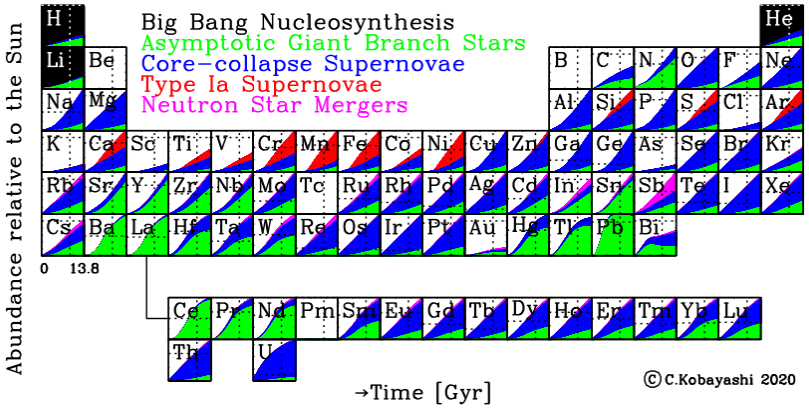

Figure 7.2: Modeled contributions of the different enrichment processes to observed elemental abundances. The names of the different processes are given in the top center of the figure. The solar values (time as a vertical dotted line, abundance as in Asplund et al. (2009) as a horizontal dotted line) are indicated for each element. Note that the yields from ECSNe and MRSNe are included in the yields of Core-collapse Supernovae. *Image credit: figure 39 in Kobayashi et al. (2020).*

(Lattimer & Schramm 1974; Rosswog et al. 1999), with multiple works claiming them to be the main source of r-process elements Côté et al. (2019); Wanajo et al. (2021); Fraser & Schönrich (2022). Multiple works stress however that the timescales of these merger appear too slow to explain the observed temporal evolution of abundance patterns (e.g. Argast et al. 2004; Cescutti et al. 2015), so that HNe/MRSNe may be required to explain the early r-process synthesis. A recent search for r-process signatures in a JWST spectrum of the Type Ic-BL SN 2024abup by Shrestha et al. (2026) found that all potential r-process spectral signatures can be just as well explained by lighter elements, further questioning dominance of HNe/MRSNe in the production of these elements. It is important to realise that beyond Zn, the abundances of the elements drop multiple orders of magnitude (information that is not extractable from Figure 7.2), so that they are not expected to dominate spectra of CCSNe, in contrast with spectra of KNe from neutron star mergers (Abbott et al. 2017).

Focusing then on the elements lighter than Zn, an interesting observation is that the intermediate-mass odd-Z elements (Cl, K, Sc and V), whose production is found to be dominated by CCSNe, are all underproduced in the Kobayashi et al. (2020) model. This

finding has been made in multiple other works as well, e.g. Timmes et al. (1995); Prantzos et al. (2018); XRISM Collaboration et al. (2026). The question is then whether this underproduction is due to a missing ingredient in CCSN models, or whether it is in fact another nucleosynthesis site whose models produce too little of these elements. A study of observed CCSN yields of these elements could answer this question, but unfortunately these elements have no strong spectral signatures in optical wavelengths. Fortunately, Cl I has a strong transition within its ground multiplet at 11.3 μm. This transition was observed in SN 1987A, and under an assumption of optically thin LTE, Aitken et al. (1988) obtained an estimate of $M_{\rm Cl\,I} = 7.4 \times 10^{-4}\ M_\odot$. [Cl I] 11.33 μm was also observed in SN 2004et (Jerkstrand et al. 2012), but no mass estimate was made. In both cases, there is an important caveat; as both are Type II SNe, [Cl I] 11.33 μm potentially faces contamination from the hydrogen transition H9 – 7 at 11.31 μm, so that the true Cl I mass may be overestimated. In **Paper III**, we study this line for the first time in a SESN (Type Ic SN 2024aecx), where no H contamination can be present, and we obtain an estimate of $M_{\rm Cl\,I} = 5.1^{+2.0}_{-1.6} \times 10^{-4}\ M_\odot$. This estimate and the one for SN 1987A may then be compared to Cl yields in e.g. the He-star model grid by Woosley (2019) + Ertl et al. (2020), which have been used as explosion models in **Papers I, II and III**, of 0.4 – 1.7 $\times 10^{-4}\ M_\odot$. This combined with the recent finding of a Cl/S ratio consistent with solar abundances for the SNR Cassiopeia A (XRISM Collaboration et al. 2026) suggests that it indeed are CCSNe that dominate the odd-Z element production, and that there thus are missing ingredients in stellar evolution models. A promising resolution is that O-C shell mergers are more prominent than currently thought, as they are found to increase Cl and other odd-Z element production by up to an order of magnitude (Rauscher et al. 2002; Ritter et al. 2018; Roberti et al. 2025; Issa et al. 2026).

Turning our attention to carbon, we see that CCSNe are responsible for roughly half of the carbon in the universe according to GCE models. However, in **Paper II** we find that for the majority of an observed sample of SESNe, `SUMO` models using the stellar evolution models by Woosley (2019); Ertl et al. (2020) as inputs overproduce C emission. This finding suggests that carbon masses in stellar evolution models, and thus the predicted part of C in the universe produced by CCSNe, might be too high. Part of the explanation can be sought in the relatively large He/C layers in the stellar evolution models (see Section 2.1.2), as we find hints in **Paper II** from the [C I] $\lambda\lambda$9824, 9850 line profiles that this zone is smaller in observed SNe. Alternatively, temperatures in the C-rich layers in

our SUMO models may have been too high, leading to stronger emission, but we show that low CO formation alone can not explain these too large temperatures.

For Nitrogen, AGB stars are found to be responsible for three quarters of today's observed abundaces in GCE models, with SNe providing the remainder. As discussed in **Paper I**, the mass of N produced per SN is relatively constant, meaning that lower mass progenitors have a comparatively larger mass of nitrogen enriched ejecta. The total abundance of N in GCE models is well produced, but great difficulty remains in reproducing the observed ^{14}N to ^{15}N ratio, with models producing a ratio roughly ten times larger than in the sun (Kobayashi et al. 2020). While we did not study the production of N in great detail in **Paper I**, constraints on nitrogen masses in the ejecta may be derived from [N II] $\lambda\lambda$6548, 6583. Treating it as an optically thin, LTE line (see Chapter 5), which according to our SUMO models should be applicable up to a few hundred days, one could set a lower limit on the temperature (using e.g. [N II] λ5754) to obtain an upper limit on the ejecta mass.

One thing that becomes clear from the discussion in this chapter is that, while GCE models have come a long way in explaining much of the evolution of elemental abundances, the role of supernovae in these models is mostly based on results from grids of stellar evolution models, rather than on observed abundances in SN ejecta. This provides a clear motivation for continued nebular phase observations of SNe which, as presented throughout this thesis and in **Papers I, II and III**, hold quantitative information on the nucleosynthesis in supernovae.

8 Paper Summary

8.1 Paper I: Nebular Nitrogen Line Emission in Stripped-Envelope Supernovae - a New Progenitor Mass Diagnostic

In **Paper I** (Barmentloo et al. 2024), we investigate the diagnostic potential of the nebular spectral line [N II] $\lambda\lambda$6548, 6583. This line has been observed in multiple Type IIb and Ib SNe, but had up until ten years ago mostly been interpreted as Hα emission due to the coincidental wavelengths. This posed a puzzle to researchers, as Type IIb and Ib SNe are believed to be almost entirely stripped of their hydrogen envelopes. Jerkstrand et al. (2015a) showed through `SUMO` spectral models that, indeed, hydrogen envelopes of $\sim 0.1\ M_{\odot}$ can not explain the observed late-time emission, whereas instead the previously not included spectral line [N II] $\lambda\lambda$6548, 6583 can obtain sufficient luminosity to match observations. Dessart et al. (2021) identified that, for a grid of SESN nebular models at a single epoch, the [N II] $\lambda\lambda$6548, 6583 strength relative to the total optical spectrum decreases with increasing progenitor mass. This trend with progenitor mass motivated the study undertaken in **Paper I**. Here, we set out to study how this trend evolves with time, with the goal of identifying the observing strategy yielding the most diagnostic power. Furthermore, we wanted to compare these model trends with a sample of observed SESNe, to look for any differences in [N II] $\lambda\lambda$6548, 6583 emission between Type IIb, Ib and Ic SNe.

To study the evolution of nitrogen emission through time, we created a grid of `SUMO` spectral models at 50 d intervals between 150 and 400 days post explosion, for five different masses of helium star progenitors from the Woosley (2019) + Ertl et al. (2020) explosion models. 2D hydrodynamical simulations were performed by our collaborators to obtain an

estimate of the extent of inmixing of the nitrogen-rich zones into the macroscopically mixed cores of the progenitors. While the He/N zones, holding the majority of nitrogen, were found to remain unmixed, the deeper lying He/C zones, with a non-negligible nitrogen contribution, were found to be partially mixed in with the radioactive power source ^{56}Ni. With this mixing parametrised in our `SUMO` models, the relation between [N II] $\lambda\lambda$6548, 6583 strength (quantified with a diagnostic $f_{[\mathrm{N\,II}]}$) and progenitor mass could be accurately quantified. Furthermore, nitrogen strength relative to the optical spectrum was found to monotonically increase with time, so that late epochs have the most diagnostic power. Also, before $\sim$ 150 d post explosion, the diagnostic power vanishes, mostly due to blending with other, comparatively strong lines.

Next, a sample of 43 SESNe with 131 nebular phase spectra was obtained through an archival search in WISeREP (Yaron & Gal-Yam 2012). When comparing the evolution of $f_{[\mathrm{N\,II}]}$ for this sample with the model grid, the observational tracks were found to evolve in a mostly similar fashion. Separating by SN type, Type IIb SNe mostly prefer tracks of low-mass progenitors, with Type Ib and Ic SNe almost exclusively following high-mass tracks. The resulting progenitor mass estimates were found to be mostly consistent with earlier literature estimates from different methodologies, although we find the $f_{[\mathrm{N\,II}]}$ diagnostic to lose power above $M_{\mathrm{preSN}} \gtrsim 5\ M_{\odot}$, as [N II] $\lambda\lambda$6548, 6583 strengths then diminish to be too weak to be distinguished. Interestingly, no Type Ic SNe show obvious signatures of [N II] $\lambda\lambda$6548, 6583 emission, consistent with the common assumption that these objects have no He-layers, as it is in these He-layers that the nitrogen is located.

In conclusion, we showcased that the relative strength of [N II] $\lambda\lambda$6548, 6583 has diagnostic potential for SN progenitor mass, especially for lower mass helium star progenitors and at late ($t \gtrsim$ 250d) epochs, with multiple epochs providing increasingly stronger constraints. This diagnostic may be used in tandem with other progenitor mass diagnostics (e.g. the [O I] $\lambda\lambda$6300, 6364; Jerkstrand et al. 2014) to thoroughly constrain SESN progenitor masses with methods independent of light curve modeling.

8.2 Paper II: Formation and Diagnostic Use of Carbon Lines in Stripped-Envelope Supernovae

In **Paper II** (Barmentloo & Jerkstrand 2026), we continue our detailed studies of individual elements in SN spectra, this time focusing on carbon. Despite being the 4th most abundant element in the universe, it remains as of today unknown what the main production site of carbon is, with both SNe and stellar winds from AGB stars contributing significantly. Expectations from SN models exist, but an observational study of carbon production in SNe has been lacking. Furthermore, a comparatively large uncertainty on the reaction rate of $^{12}\mathrm{C}(\alpha,\gamma)^{16}\mathrm{O}$ results in large uncertainties on carbon production in stellar evolution models. This rate sets the abundance of C left at the end of He-burning, in turn influencing the compactness and thereby whether and how the star explodes. Obtaining observational estimates on carbon masses in SNe can in turn also help in constraining this rate, providing a benchmark for future stellar evolution codes to reproduce.

To learn more about carbon production in SNe, we take a similar approach as in **Paper I**; first, we created a grid of `SUMO` models mostly similar to **Paper I**, but this time we also include molecule formation, as molecules through their cooling effect in primarily carbon-enriched zones are expected to have a signficant impact on carbon emission. From this model grid, we identify two carbon lines which can be expected to be observable in nebular SN spectra; [C I] λ8727 and [C I] $\lambda\lambda$9824, 9850. Both being optically thin, mostly LTE lines, we show how the relative strength of these lines may be used to obtain a carbon temperature estimate, in turn yielding a direct measurement of the neutral carbon mass. The `SUMO` models also show that the ionisation fraction of C I remains relatively constant for different epochs and progenitor masses, allowing for a relatively well constrained estimate on the total carbon mass.

We then apply these results to the same sample of SESNe as in **Paper I**. We show how obtaining the carbon mass is complicated by two things. First, there is a lack of observations of [C I] $\lambda\lambda$9824, 9850, as its wavelength regime is often not covered in optical spectrographs. Second [C I] λ8727 is usually blended with the Ca II NIR triplet, complicating extraction of its luminosity. To this end, we develop the Monte Carlo scattering code CaNARY, which solely focuses on the spectral formation of the Ca II NIR triplet + [C I] λ8727 region, and allows for the estimation of the [C I] λ8727 luminosity from a

blended line profile. With the luminosities for [C I] λ8727 and [C I] $\lambda\lambda$9824, 9850 (for those spectra that do cover the wavelength region) obtained, we find that our model spectra in a majority of cases overproduce the observed carbon emission. While potentially indicative of too large carbon masses in the adopted explosion models, our results are convoluted by LTE departure of [C I] λ8727. Despite this, we do find some SNe with upper limits of 0.05 $M_{\odot}$ on the carbon mass, lower than any models in our grid. Lastly, we identify a comparison between the width of [C I] $\lambda\lambda$9824, 9850 and [O I] $\lambda\lambda$6300, 6364 as a tool for estimating the extent of the He/C zone. The mass of this zone, as well as its carbon abundance, varies appreciably in different stellar evolution models, and we find indications that this zone is more massive in our model grid than in the observed SNe.

Our results showcase the potential, as well as the challenges of using nebular spectra to measure the carbon content of SNe. [C I] $\lambda\lambda$9824, 9850 is identified as the most useful of the carbon lines, but there is a lack of observations, especially at late (t $\gtrsim$ 300d) times. Therefore, we encourage observers to target [C I] $\lambda\lambda$9824, 9850 in future observing campaigns.

8.3 Paper III: A Framework for Analysing Nebular-Phase JWST Supernova Spectra with Application to Type Ic SN 2024aecx

Paper III builds on some of the analytical work in **Paper II**, hoping to avoid the difficulties identified with lines such as [C I] λ8727, that fall out of LTE in the studied epochs. This is done by shifting focus to the IR wavelengths, where SN spectra are dominated by ground-state transitions with lower critical electron densities. These lines are therefore excellent probes of ionic masses and emitting volumes. The IR spectral window has with the launch of the JWST been reopened after a hiatus of a dozen years with the end of operations of the Infrared Spectrograph on the Spitzer Space Telescope. With the first few JWST nebular spectra of CCSNe coming in and (hopefully) many more to come in the following years, our goal with **Paper III** was to provide the community with an easy to use framework for extracting as much information as possible from a JWST nebular spectrum. To showcase the framework, we apply it to a single, 167 d spectrum of the nearby Type Ic SN 2024aecx.

The main component of the framework is to learn whether a spectral line, for a given epoch, is a) in LTE with respect to the ground state and b) is optically thick or thin. To determine if LTE conditions are applicable for a spectral line, one needs to know if collisions dominate over radiative processes for both the population and depopulation of the transition's upper level. In the literature, this is often estimated by checking if the local electron density n_e is larger than the critical electron density $n_{e,crit}$ (see Section 5.1.1). Whereas previous works often only consider the competition between the collisional and radiative depopulation through the transition itself to calculate $n_{e,crit}$, we expand on this calculation by including all collisional and radiative depopulations out of the level, as well as populations from both lower- and higher-lying levels. We then compare these $n_{e,crit}$ values with n_e values from a grid of `SUMO` models with a range of progenitor masses and epochs. These models are also used to obtain the Sobolev optical depths τ_S (see Section 5.1.2) of the lines. We combine these optical depths with the ratio $n_e/n_{e,crit}$ in so-called line regime plots, which may directly be employed by the community to estimate the regimes for spectral lines for their SN of interest.

With these estimates in place, we find that the majority of lines in the spectral range observed by JWST are, in SESNe, confidently in the optically thin LTE regime up to 200 – 300 days post explosion, allowing for the derivation of ionic masses and thus study of the SN nucleosynthesis. Lines like [Ne II] 12.81 μm are instead in the optically thick LTE regime, so that they probe the emitting volume and thereby the explosion physics. Applying this framework to SN 2024aecx, we find that the plethora of Ni and Co lines allows for estimating the total masses of these elements. To do so, we present a novel methodology using the luminosity ratio of [Ni II] 6.636 μm and [Co II] 10.52 μm to determine the optical depths of these lines directly from the spectrum, revealing that in SN 2024aecx, [Co II] 10.52 μm is firmly optically thick. This allowed us to estimate the filling factor of the zone with Si burning ashes, which we find to be consistent with a weak Ni-bubble effect (see Section 3.4), having important consequences for the spectral modeling of SESNe. Further results include a chlorine mass in SN 2024aecx comparable to the one found for SN 1987A, but about three to ten times larger than found in our model grid. This finding provides further evidence that the long observed mismatch between observed and modeled yields of intermediate odd-Z elements (see Section 7) is due to missing ingredients in the stellar evolution modeling.

Many more interesting results were found for SN 2024aecx, showcasing how much

researchers can learn about SNe from a single JWST spectrum. We recommend epochs of $t \sim 150$ – 250 d as optimal for JWST spectra, as they best strike the balance between secure LTE approximations and negligible line blending.

9 Closing Words

Before sending you, reader, on to the papers, I would like to take a short moment to look at potential future directions for the work presented in them.

Up until recently, the SN world has, for the most part been one of a classificatory character. Much progress has been made in our understanding of how many different supernova types there are, how these types typically evolve and behave, and for many classes the field has even succeeded in finding consensus on their progenitors. This is an achievement that can not be understated, especially when one remembers that much of this has been learned from observing unresolved specs of light tens of millions of light years away.

However, advances in both stellar evolution and spectral modeling have started to allow us to also study SNe, and especially their nucleosynthesis, more quantitatively. From comparisons to model spectra, it has now been possible to obtain quantitative estimates of e.g. the oxygen mass present in the ejecta, one which in turn has been related to the progenitor mass, providing quantitative distinctions between the different SN types. It is my hope that the methodologies presented in these three papers may help advance this quantitative study of SNe, even if only marginally.

What I believe is the way forward for the SN field in the coming years, is to start building a sample of SNe to which all the nebular diagnostics in the field are applied, so that we may have, for example, a few dozen SNe for which we know from nebular spectra the oxygen, nitrogen, carbon, chlorine, argon, nickel and iron masses, as well as the progenitor mass. While the first three may be obtained from optical spectra, JWST spectra are indispensable for obtaining the latter, making it likely that we will see a lot of progress in this regard in the coming years. While we have attempted to obtain some of these masses for a sample in **Paper I** and **Paper II**, this sample was in no way optimised for obtaining these quantities. Now that our work has laid out the most

optimal epochs for obtaining these estimates, I hope that future observing campaigns may use these recommendations and obtain such an optimised sample. While a sample is needed, I believe that there is still a large role here for the, in the SN-world beloved, single-object papers; as we have found in each of the papers, none of these diagnostics come without caveats, and thoroughly considering these for each individual object simply requires time!

Concerning work on the diagnostics themselves, a clear improvement for our understanding of their applicability would be to test them against spectral model grids based on a different grid of explosion models. While the work in **Papers I, II and III** could not have been done without the explosion models presented by Woosley (2019) and Ertl et al. (2020), they are not the only models out there, and clear differences exist in e.g. the carbon nucleosynthesis (see section 6.1 in **Paper II** and Farmer et al. (2021)). A related future study would be to investigate if the diagnostics obtained are also applicable to other SN types. In the works presented in this thesis, the only spectral models simulated were those of SESNe. Yet, it is plausible that, due to lower expansion velocities and thus typically larger densities, transitions in Type II SNe may leave LTE later than their stripped siblings, making them potentially even better targets for LTE analysis of JWST spectra. Finally, studies of how these diagnostics are influenced by viewing angle effects will be essential for understanding the inherent scatter of the model tracks to which the diagnostics are calibrated, and consequently what sample size of 'extremely-well studied' SNe is necessary to draw statistically significant conclusions.

With this said, I leave you now to read the papers in their entirety. I hope that they may please you, and that at least some of the enthusiasm with which I have worked on them these past four years slips through the cracks of scientific writing. **Enjoy!**

Acknowledgements

And now for the most difficult part, to properly thank each and everyone that has meant something to me during this four-year journey. Due to the large amount of amazing people I have met and worked with during this time, I think that to really give each person the praise they deserve, all the trees in my home country of the Netherlands would have to be cut for all the pages I would write! To leave some trees still standing, I will therefore focus on a few people in particular. To all other lovely people that I met in the astronomy department, I hope that you all know what you mean to me, and I am very much looking forward to seeing you as much as possible in the coming years, wherever you all may be[1]

To start, I want to thank my supervisor, **Anders**. From the very beginning of this journey, I have felt a sense of security in having you as my supervisor; whenever we had our weekly meetings, I always felt that you were fully present and tried to help me as good as you could. Whenever I knocked on your door with a question, you would take the time to help me forward. In particular, I was always amazed by your way of looking at the bigger picture when it comes to science; instead of focusing only on the next paper or deadline, you multiple times discussed your views on what we should try to aspire as scientists, or how you believe that we actually learn something in our research. These conversations inspired me greatly, and I will surely miss them! Also on a personal level I felt comfortable with you, always starting our meetings with a chat about things other than work and there was always plenty of room for the odd little joke. In summary, it would have been very difficult for me to find a better supervisor than you; thanks a lot for being there!

Next, I thank my co-supervisor, **Jesper**. I am still extremely thankful that you gave me, a theoretical astronomer, the opportunity of a lifetime to go observing at some of the world's best telescopes at the La Silla observatory in Chile. It was a childhood dream come

[1]Please do not make my future train journeys too far!

true, and it taught me valuable lessons on the interface between theory and observation, and on how both can be made most useful to the other, lessons you also taught me in office. Furthermore, I much appreciate your great eye for detail when it comes to reading through paper/thesis drafts; it never ceases to amaze me how you can distinguish between all the different LaTeX commands on a written paper.

I also would like to thank my mentor **Matthew**, especially for the half-yearly progress meetings where I felt free to discuss whatever feelings, fears or thoughts regarding the PhD and the future came up. You always took them seriously, and helped me go through any issues in an open, philosophical manner.

Of course, a 'thank you' is not complete without thanking the three people who I have probably spent the most awake hours in the same room with in the last three years, my μπαχουρι-office mates **Anna, Bart and Yang**. I honestly do not think that I could have made it through the PhD without your constant help in both science and life. Hopefully the daily dose of my loud music when the headphones stopped working was not too disturbing!

Bart, our journey started even before I arrived in Stockholm, when I saw your face during my zoom-interview. When I got the question 'what is your favorite type of supernova', meant as a question to make me feel at ease, and I answered that 'I only know one type...', you must've wondered what questions I would ask you when I'd eventually be sitting in the same office. You were however always patient with the hundreds of questions I asked you and always made time to help, a kindness that is a rare quality you have. It was also great to have you as a fellow dutch-buddy in lunch table discussions, even if you were not on my side when it came to my daily choice of lunch... Bart, I want to thank you for all our time together, and hope we meet many times more!

Anna, my loveliest office mate, I am super thankful that whenever I did not know how to do something 'that observers do', I could turn my chair, say your name, and that a face would appear from behind a big black screen happy to answer. Besides science we talked about many other fun and random things[2], and I always felt safe with you to share my thoughts and feelings. Perhaps most importantly of all, I could always rely on you at work parties to join in whenever I wanted to do a crazy dance. All the best the coming years in California, hope we meet again soon!

Yang, you felt like a younger brother in office. Coming in a little over a year after I

[2]and often about your 'visitor'.

did, it has been amazing to see you grow as a PhD from quietely sitting in the back to taking a leading role in the scientific discussions. Your patience, calmness and unexpected jokes always made it a pleasure to chat with you. I will miss the countless candy you brought from the other side of the world, the way too many far away games we played, and battling each morning on who is first in office (Bart and Anna never were in the match!). I wish you good luck with the final year of the PhD and will definitely come up to the 6th floor to play some more games together!

Alex, I think it is safe to say that you have been my closest buddy during the PhD. Starting our journeys practically on the same day, we have spent so much time of amazing fun together. Going to concerts, picking mushrooms, some cold swims, sunny bikerides, training for and finishing Vasaloppet, and of course countless amazing dinners! I was even there when you met your girlfriend, lovely Johanna! Your unstoppable enthusiasm and welcoming attitude inspired me to try to be more like that myself, and your honesty has helped me through some of the more difficult moments of these years. Even in astronomy, you importantly introduced me to PAH, teaching me that, no Stan, you are not looking at a supernova spectrum, but at a galaxy... I wish you all the best, whatever the uncertain future holds, but I do hope to be at least a small part of that future. Ti voglio bene amico! P.S. thanks again for letting me and Elsa crash at your place when I forgot my keys at the restaurant!

Etienne, your theory of boxes tells me you would not be one for enjoying a long paragraph of praise, so good luck. I was so glad when I heard the news that you got a position in Stockholm. Even though more than a year had passed since meeting you at a conference on Corsica and even though we had hardly spoken in the meantime, I was sure that many fun moments lay ahead. And so they did! Discussing the most random of fun facts, tasting your fermented 'creations' and even attempting to make a cheese together (R.I.P. Jean Pierre)! I always felt comfortable talking about whatever with you, as I knew you would listen without judgment. Soon moving from Stockholm once more, the thing I will miss most of all is the way you pronounce 'Holland' (or 'Haaland', or 'Åland', or 'Hollande', I still have no clue).

Priscila, I still remember one of our first encounters: you were cheering as Argentina kicked the Netherlands out of the world cup. A year later we spent 3 weeks together observing in Chile, and I cherish many of the conversations and (sometimes heated) discussions we had while admiring that stunning place. Your bravery in standing up for

what you think is right, both in the academic world and the real world, is something that keeps amazing me, and I hope to become as brave as you one day! I knew I could always turn to you for an honest opinion or advice and want to thank you for the countless times you helped me out. Yours truly!

This brings me to my lovely family, my mom, my dad and my sister, as well as my two grandmothers. **Pap** en **Mam**, jullie zijn een groot deel van de reden dat ik dit werk nu mag schrijven. Toen jullie me voor het eerst als vierjarig jochie op de camping in Kroatië de 'tafels tot dertien' lieten maken is er een interesse voor rekenen losgekomen die nooit meer is verdwenen. In plaats van die in te dammen of te beperken stonden jullie altijd klaar om mij aan te moedigen met wat ik ook wilde doen, ook al was het niet altijd het makkelijkste om te doen. Ook toen de interesse voor rekenen na een vrijdagavond bij de kleine sterrenwacht in Bussloo omsloeg in een interesse in sterrenkunde, gingen jullie iedere vrijdagavond dat ik wilde weer met me mee om naar urenlange praatjes te luisteren. Jullie ongekende toewijding tijdens werk (ook al is het niet altijd even leuk) heeft mij altijd geinspireerd, en ik weet zeker dat ik het zonder die inspiratie niet zo ver had geschopt. Die inspiratie brachten jullie ook over op **Joyce**, mijn allerliefste zussie. Ik ben heel dankbaar dat wij niet als vechtende, maar als liefhebbende en samenwerkende broer en zus zijn opgegroeid. We zijn altijd een goed team en als jij mee was naar een spannende verjaardag of ander evenement voelde ik me altijd op mijn gemak! Hoe veel jij denkt aan hoe anderen zich voelen is een eigenschap die niet altijd even makkelijk is, maar tegelijkertijd één waar heel veel mensen jaloers op mogen zijn. Ook je dapperheid om dingen te doen die je eigenlijk heel spannend vindt bewonder ik en maakt mij trots jouw grote broer te mogen zijn! Ook **Oma Barmentloo** en **Oma Hennekes** wil ik heel erg bedanken. Jullie luisterden altijd geïnteresseerd als ik iets te vertellen had, en het maakte niet uit of het iets moeilijks of saais was. Jullie waren, samen met **Opa Barmentloo** en **Opa Hennekes**, en zijn altijd super lief voor mij en Joyce en deden altijd leuke en avontuurlijke dingen met ons om ons te inspireren. Ik ben zo trots dat jullie helemaal naar Stockholm zijn gekomen om mij op te zoeken, en het laat nog maar eens zien wat een lieve en toegewijde oma's jullie zijn. Lieve familie, ik hou van jullie allemaal!

Finally, I want to thank **Elsa**, the love of my life, without whom I never would have been able to write this thesis. Ja du älskling, du trodde väl inte att jag skulle glömma dig! Hela den här doktorandresan började med vår bilresa från Nederländerna till Stockholm, och även om det kändes som ett stort och ovisst äventyr, så kände jag mig lugn i att du

var vid min sida. Du har under alla dessa år alltid varit mitt största stöd, även i stunder där du själv inte mådde lika bra. Varje dag fanns du där och frågade hur det hade varit på jobbet, och om jag var stressad över någon deadline eller kommande presentation kunde du alltid lugna ner mig med några fina ord och en varm kram. Du fick mig även att inse att jag inte *är* mitt jobb, och att jag är mer en *bara* ett mattesnille, en insikt som har gjort mitt liv så otroligt mycket roligare och mera avslappnat. Älskade **Elsa**, du får mig varje dag att känna mig som en bättre version av mig själv, och jag vill tacka dig hemskt mycket för allt du är och allt du har gjort för mig. Jag älskar dig!

Bibliography

Abbott, B. P., Abbott, R., Abbott, T. D., et al. 2017, ApJ, 848, L12

Abbott, D. C.& Lucy, L. B. 1985, ApJ, 288, 679

Adelberger, E. G., Austin, S. M., Bahcall, J. N., et al. 1998, Reviews of Modern Physics, 70, 1265

Aitken, D. K., Smith, C. H., James, S. D., et al. 1988, MNRAS, 235, 19P

Alpher, R. A., Herman, R.,& Gamow, G. A. 1948, Physical Review, 74, 1198

Anderson, J. P., Covarrubias, R. A., James, P. A., Hamuy, M.,& Habergham, S. M. 2010, MNRAS, 407, 2660

Anderson, J. P., James, P. A., Habergham, S. M., Galbany, L.,& Kuncarayakti, H. 2015, PASA, 32, e019

Arcavi, I., Gal-Yam, A., Yaron, O., et al. 2011, ApJ, 742, L18

Argast, D., Samland, M., Thielemann, F.-K.,& Qian, Y.-Z. 2004, A&A, 416, 997

Arnett, D. 1996, Supernovae and Nucleosynthesis: An Investigation of the History of Matter from the Big Bang to the Present

Arnett, W. D. 1980, ApJ, 237, 541

Arnett, W. D. 1982, ApJ, 253, 785

Asplund, M., Grevesse, N., Sauval, A. J.,& Scott, P. 2009, ARA&A, 47, 481

Axelrod, T. S. 1980, PhD thesis, University of California, Santa Cruz

Baade, W. 1945, ApJ, 102, 309

Baade, W.& Zwicky, F. 1934, Proceedings of the National Academy of Science, 20, 254

Banerjee, D. P. K., Joshi, V., Evans, A., et al. 2018, MNRAS, 481, 806

Barbarino, C., Sollerman, J., Taddia, F., et al. 2021, A&A, 651, A81

Barbon, R., Ciatti, F.,& Rosino, L. 1979, A&A, 72, 287

Barmentloo, S.& Jerkstrand, A. 2026, MNRAS, 545, staf2033

Barmentloo, S., Jerkstrand, A., Iwamoto, K., et al. 2024, MNRAS, 533, 1251

Baron, E., Cooperstein, J.,& Kahana, S. 1985, Phys. Rev. Lett., 55, 126

Beals, C. S. 1930, JRASC, 24, 277

Beals, C. S. 1951, MNRAS, 111, 202

Bersten, M. C.& Mazzali, P. A. 2017, in Handbook of Supernovae, ed. A. W. Alsabti & P. Murdin, 723

Bertulani, C. A.& Kajino, T. 2016, Progress in Particle and Nuclear Physics, 89, 56

Bethe, H. A. 1990, Reviews of Modern Physics, 62, 801

Björklund, R., Sundqvist, J. O., Puls, J.,& Najarro, F. 2021, A&A, 648, A36

Blinnikov, S. I., Nadyozhin, D. K., Woosley, S. E.,& Sorokina, E. I. 2002, in Nuclear Astrophysics, ed. W. Hillebrandt & E. Müller, 144–147

Blondin, J. M., Mezzacappa, A.,& DeMarino, C. 2003, ApJ, 584, 971

Blondin, S., Blinnikov, S., Callan, F. P., et al. 2022, A&A, 668, A163

Boissier, S.& Prantzos, N. 2009, A&A, 503, 137

Borst, L. B. 1950, Physical Review, 78, 807
Brennan, S. J., Sollerman, J., Irani, I., et al. 2024, A&A, 684, L18
Bruch, R. J., Gal-Yam, A., Yaron, O., et al. 2023, ApJ, 952, 119
Burbidge, E. M., Burbidge, G. R., Fowler, W. A.,& Hoyle, F. 1957, Reviews of Modern Physics, 29, 547
Burbidge, G. R., Hoyle, F., Burbidge, E. M., Christy, R. F.,& Fowler, W. A. 1956, Physical Review, 103, 1145
Burrows, A., Hayes, J.,& Fryxell, B. A. 1995, ApJ, 450, 830
Burrows, A.& Vartanyan, D. 2021, Nature, 589, 29
Cano, Z. 2013, MNRAS, 434, 1098
Carruthers, G. R. 1968, ApJ, 151, 269
Catchpole, R. M., Whitelock, P. A., Feast, M. W., et al. 1988, MNRAS, 231, 75P
Caughlan, G. R.& Fowler, W. A. 1962, ApJ, 136, 453
Cescutti, G., Romano, D., Matteucci, F., Chiappini, C.,& Hirschi, R. 2015, A&A, 577, A139
Chandrasekhar, S. 1931, ApJ, 74, 81
Chieffi, A.& Limongi, M. 2020, ApJ, 890, 43
Chugai, N. N. 1988a, Astronomicheskij Tsirkulyar, 1533, 7
Chugai, N. N. 1988b, Ap&SS, 146, 375
Claeys, J. S. W., de Mink, S. E., Pols, O. R., Eldridge, J. J.,& Baes, M. 2011, A&A, 528, A131
Colgate, S. A.& McKee, C. 1969, ApJ, 157, 623
Colgate, S. A., Petschek, A. G.,& Kriese, J. T. 1980, ApJ, 237, L81
Conti, P. S. 1975, Memoires of the Societe Royale des Sciences de Liege, 9, 193
Côté, B., Eichler, M., Arcones, A., et al. 2019, ApJ, 875, 106
de Kool, M., Li, H.,& McCray, R. 1998, ApJ, 503, 857
deBoer, R. J., Görres, J., Wiescher, M., et al. 2017, Reviews of Modern Physics, 89, 035007
Dessart, L. 2025, A&A, 703, A287
Dessart, L.& Hillier, D. J. 2010, MNRAS, 405, 2141
Dessart, L.& Hillier, D. J. 2020, A&A, 643, L13
Dessart, L., Hillier, D. J., Sukhbold, T., Woosley, S. E.,& Janka, H. T. 2021, A&A, 656, A61
Dessart, L., Hillier, D. J.,& Wilk, K. D. 2018, A&A, 619, A30
Dessart, L., Hillier, D. J., Woosley, S., et al. 2016, MNRAS, 458, 1618
Dessart, L., Hillier, D. J., Woosley, S. E.,& Kuncarayakti, H. 2023, A&A, 677, A7
Dessart, L., Kotak, R., Jacobson-Galán, W., et al. 2025, A&A, 704, L6
Dessart, L., Yoon, S.-C., Aguilera-Dena, D. R.,& Langer, N. 2020, A&A, 642, A106
Deutsch, A. J. 1956, ApJ, 123, 210
Drout, M. R., Milisavljevic, D., Parrent, J., et al. 2016, ApJ, 821, 57
Drout, M. R., Soderberg, A. M., Gal-Yam, A., et al. 2011, ApJ, 741, 97
Ebisuzaki, T., Shigeyama, T.,& Nomoto, K. 1989, ApJ, 344, L65
Ekström, S. 2021, Frontiers in Astronomy and Space Sciences, 8, 53
El Eid, M. F., The, L. S.,& Meyer, B. S. 2009, Space Sci. Rev., 147, 1
Elias, J. H., Matthews, K., Neugebauer, G.,& Persson, S. E. 1985, ApJ, 296, 379
Ensman, L.& Burrows, A. 1992, ApJ, 393, 742
Ergon, M.& Fransson, C. 2022, A&A, 666, A104
Ergon, M., Fransson, C., Jerkstrand, A., et al. 2018, A&A, 620, A156
Ergon, M., Jerkstrand, A., Sollerman, J., et al. 2015, A&A, 580, A142
Ertl, T., Woosley, S. E., Sukhbold, T.,& Janka, H. T. 2020, ApJ, 890, 51
Fang, Q., Maeda, K., Kuncarayakti, H.,& Nagao, T. 2024, Nature Astronomy, 8, 111
Farmer, R., Laplace, E., de Mink, S. E.,& Justham, S. 2021, ApJ, 923, 214

Fernández, R., Müller, B., Foglizzo, T.,& Janka, H.-T. 2014, MNRAS, 440, 2763
Filippenko, A. V. 1997, ARA&A, 35, 309
Filippenko, A. V., Matheson, T.,& Ho, L. C. 1993, ApJ, 415, L103
Filippenko, A. V.& Sargent, W. L. W. 1986, AJ, 91, 691
Fransson, C.& Chevalier, R. A. 1989, ApJ, 343, 323
Fraser, J.& Schönrich, R. 2022, MNRAS, 509, 6008
Fraser, M., Stritzinger, M. D., Brennan, S. J., et al. 2021, arXiv e-prints, arXiv:2108.07278
Fremling, C., Sollerman, J., Taddia, F., et al. 2014, A&A, 565, A114
Frentz, B., Aprahamian, A., Boeltzig, A., et al. 2022, , 106, 065803
Gabler, M., Wongwathanarat, A.,& Janka, H.-T. 2021, MNRAS, 502, 3264
Gal-Yam, A. 2017, in Handbook of Supernovae, ed. A. W. Alsabti & P. Murdin, 195
Gal-Yam, A., Bruch, R., Schulze, S., et al. 2022, Nature, 601, 201
Gardner, J. P., Mather, J. C., Abbott, R., et al. 2023, PASP, 135, 068001
Gaskell, C. M., Cappellaro, E., Dinerstein, H. L., et al. 1986, ApJ, 306, L77
Gilkis, A.& Arcavi, I. 2022, MNRAS, 511, 691
Gkini, A., Lunnan, R., Schulze, S., et al. 2024, A&A, 685, A20
Hachisu, I., Matsuda, T., Nomoto, K.,& Shigeyama, T. 1991, ApJ, 368, L27
Hammer, N. J., Janka, H. T.,& Müller, E. 2010, ApJ, 714, 1371
Haynes, C. J.& Kobayashi, C. 2019, MNRAS, 483, 5123
Heger, A., Fryer, C. L., Woosley, S. E., Langer, N.,& Hartmann, D. H. 2003, ApJ, 591, 288
Hendrick, S. P., Reynolds, S. P.,& Borkowski, K. J. 2005, ApJ, 622, L117
Herant, M.& Benz, W. 1991, ApJ, 370, L81
Herant, M., Benz, W., Hix, W. R., Fryer, C. L.,& Colgate, S. A. 1994, ApJ, 435, 339
Hillier, D. J. 1991, A&A, 247, 455
Hillier, D. J.& Dessart, L. 2012, MNRAS, 424, 252
Hillier, D. J.& Miller, D. L. 1998, ApJ, 496, 407
Ho, A. Y. Q., Goldstein, D. A., Schulze, S., et al. 2019, ApJ, 887, 169
Issa, J., Herwig, F., Mojzsis, S. J.,& Pignatari, M. 2026, ApJ, 997, 314
Iwamoto, K., Young, T. R., Nakasato, N., et al. 1997, ApJ, 477, 865
Jacobson-Galán, W. V., Dessart, L.,& Vartanyan, D. 2026, ApJ, 1006, 66
Janka, H.-T. 2012, Annual Review of Nuclear and Particle Science, 62, 407
Janka, H. T., Langanke, K., Marek, A., Martínez-Pinedo, G.,& Müller, B. 2007, , 442, 38
Jerkstrand, A. 2011, PhD thesis, Stockholm University
Jerkstrand, A. 2017, in Handbook of Supernovae, ed. A. W. Alsabti & P. Murdin, 795
Jerkstrand, A., Ergon, M., Smartt, S. J., et al. 2015a, A&A, 573, A12
Jerkstrand, A., Ergon, M., Smartt, S. J., et al. 2015b, A&A, 573, A12
Jerkstrand, A., Fransson, C.,& Kozma, C. 2011, A&A, 530, A45
Jerkstrand, A., Fransson, C., Maguire, K., et al. 2012, A&A, 546, A28
Jerkstrand, A., Pognan, Q., Banerjee, S., et al. 2025, arXiv e-prints, arXiv:2510.12410
Jerkstrand, A., Smartt, S. J., Fraser, M., et al. 2014, MNRAS, 439, 3694
Jerkstrand, A., Smartt, S. J., Sollerman, J., et al. 2015c, MNRAS, 448, 2482
Jerkstrand, A., Wongwathanarat, A., Janka, H. T., et al. 2020, MNRAS, 494, 2471
Jermyn, A. S., Bauer, E. B., Schwab, J., et al. 2023, ApJS, 265, 15
Käppeler, F., Gallino, R., Bisterzo, S.,& Aoki, W. 2011, Reviews of Modern Physics, 83, 157
Karamehmetoglu, E., Sollerman, J., Taddia, F., et al. 2023, A&A, 678, A87
Khatami, D. K.& Kasen, D. N. 2019, ApJ, 878, 56
Kippenhahn, R.& Weigert, A. 1967, , 65, 251

Kitaura, F. S., Janka, H. T.,& Hillebrandt, W. 2006, A&A, 450, 345
Kobayashi, C., Karakas, A. I.,& Lugaro, M. 2020, ApJ, 900, 179
Kobulnicky, H. A., Kiminki, D. C., Lundquist, M. J., et al. 2014, ApJS, 213, 34
Kotak, R., Meikle, W. P. S., Farrah, D., et al. 2009, ApJ, 704, 306
Kotok, É. V. 1967, Soviet Ast., 10, 806
Kozma, C.& Fransson, C. 1992, ApJ, 390, 602
Kromer, M.& Sim, S. A. 2009, MNRAS, 398, 1809
Kumagai, S., Shigeyama, T., Nomoto, K., et al. 1989, ApJ, 345, 412
Langer, N. 2012, ARA&A, 50, 107
Laplace, E., Justham, S., Renzo, M., et al. 2021, A&A, 656, A58
Lattimer, J. M.& Schramm, D. N. 1974, ApJ, 192, L145
Lauterborn, D. 1970, A&A, 7, 150
Lazarus, P., Tauris, T. M., Knispel, B., et al. 2014, MNRAS, 437, 1485
LeBlanc, F. 2010, An Introduction to Stellar Astrophysics
Li, H., McCray, R.,& Sunyaev, R. A. 1993, ApJ, 419, 824
Li, W., Leaman, J., Chornock, R., et al. 2011, MNRAS, 412, 1441
Liljegren, S., Jerkstrand, A., Barklem, P. S., et al. 2023, A&A, 674, A184
Liljegren, S., Jerkstrand, A.,& Grumer, J. 2020, A&A, 642, A135
Liu, W.& Dalgarno, A. 1995, ApJ, 454, 472
Liu, W., Dalgarno, A.,& Lepp, S. 1992, ApJ, 396, 679
Liu, Y.-Q., Modjaz, M., Bianco, F. B.,& Graur, O. 2016, ApJ, 827, 90
Lucy, L. B., Danziger, I. J., Gouiffes, C.,& Bouchet, P. 1989, in IAU Colloquium 120: Structure and Dynamics of the Interstellar Medium, ed. G. Tenorio-Tagle, M. Moles, & J. Melnick, Vol. 350, 164
Lucy, L. B.& Solomon, P. M. 1970, ApJ, 159, 879
Lundmark, K. 1925, MNRAS, 85, 865
Lyman, J. D., Bersier, D., James, P. A., et al. 2016, MNRAS, 457, 328
Ma, X., Wang, X., Mo, J., et al. 2025, A&A, 698, A305
Maeda, K., Kawabata, K., Mazzali, P. A., et al. 2008, Science, 319, 1220
Maeda, K., Tanaka, M., Nomoto, K., et al. 2007, ApJ, 666, 1069
Martins, F., Schaerer, D., Hillier, D. J., et al. 2005, A&A, 441, 735
Mason, B. D., Gies, D. R., Hartkopf, W. I., et al. 1998, AJ, 115, 821
Mason, B. D., Hartkopf, W. I., Gies, D. R., Henry, T. J.,& Helsel, J. W. 2009, AJ, 137, 3358
Matsuura, M. 2017, in Handbook of Supernovae, ed. A. W. Alsabti & P. Murdin, 2125
Mayer, M. G.& Teller, E. 1949, Physical Review, 76, 1226
Mazzali, P. A., Kawabata, K. S., Maeda, K., et al. 2007, ApJ, 670, 592
Mazzali, P. A., Maurer, I., Valenti, S., Kotak, R.,& Hunter, D. 2010, MNRAS, 408, 87
Mazzali, P. A., Nomoto, K., Patat, F.,& Maeda, K. 2001, ApJ, 559, 1047
McCrea, W. H. 1929, Zeitschrift fur Physik, 57, 367
Meakin, C. A.& Arnett, D. 2006, ApJ, 637, L53
Meikle, W. P. S., Allen, D. A., Spyromilio, J.,& Varani, G. F. 1989, MNRAS, 238, 193
Mennekens, N.& Vanbeveren, D. 2014, A&A, 564, A134
Meyerott, R. E. 1980, ApJ, 239, 257
Minkowski, R. 1939, ApJ, 89, 156
Minkowski, R. 1941, PASP, 53, 224
Modjaz, M., Kirshner, R. P., Blondin, S., Challis, P.,& Matheson, T. 2008, ApJ, 687, L9
Moe, M.& Di Stefano, R. 2017, ApJS, 230, 15
Moffat, A. F. J. 2008, in Clumping in Hot-Star Winds, ed. W.-R. Hamann, A. Feldmeier, & L. M.

Oskinova, 17
Morales-Garoffolo, A., Elias-Rosa, N., Bersten, M., et al. 2015, MNRAS, 454, 95
Morton, D. C. 1967, ApJ, 147, 1017
Nagasawa, M., Nakamura, T.,& Miyama, S. M. 1988, Publ. Astron. Soc. Jpn, 40, 691
Nelson, C. A.& Eggleton, P. P. 2001, ApJ, 552, 664
Nomoto, K.& Hashimoto, M. 1988, , 163, 13
Nomoto, K., Suzuki, T., Shigeyama, T., et al. 1993, Nature, 364, 507
Nomoto, K. I., Iwamoto, K.,& Suzuki, T. 1995, , 256, 173
Ono, M., Nagataki, S., Ferrand, G., et al. 2020, ApJ, 888, 111
Osterbrock, D. E.& Ferland, G. J. 2006, Astrophysics of gaseous nebulae and active galactic nuclei
Paczyński, B. 1971, ARA&A, 9, 183
Pastorello, A., Quimby, R. M., Smartt, S. J., et al. 2008, MNRAS, 389, 131
Pastorello, A., Smartt, S. J., Mattila, S., et al. 2007, Nature, 447, 829
Pastorello, A., Valenti, S., Zampieri, L., et al. 2009, MNRAS, 394, 2266
Paxton, B., Bildsten, L., Dotter, A., et al. 2011, ApJS, 192, 3
Paxton, B., Cantiello, M., Arras, P., et al. 2013, ApJS, 208, 4
Paxton, B., Marchant, P., Schwab, J., et al. 2015, ApJS, 220, 15
Paxton, B., Schwab, J., Bauer, E. B., et al. 2018, ApJS, 234, 34
Paxton, B., Smolec, R., Schwab, J., et al. 2019, ApJS, 243, 10
Pepper, B. T., Istrate, A. G., Romero, A. D.,& Kepler, S. O. 2022, MNRAS, 513, 1499
Perley, D. A., Sollerman, J., Schulze, S., et al. 2022, ApJ, 927, 180
Petrović, J. 2020, Serbian Astronomical Journal, 201, 1
Petrovic, J., Langer, N.,& van der Hucht, K. A. 2005, A&A, 435, 1013
Pignatari, M., Gallino, R., Heil, M., et al. 2010, ApJ, 710, 1557
Podsiadlowski, P., Hsu, J. J. L., Joss, P. C.,& Ross, R. R. 1993, Nature, 364, 509
Podsiadlowski, P., Joss, P. C.,& Hsu, J. J. L. 1992, ApJ, 391, 246
Prantzos, N., Abia, C., Limongi, M., Chieffi, A.,& Cristallo, S. 2018, MNRAS, 476, 3432
Prentice, S. J., Ashall, C., James, P. A., et al. 2019a, MNRAS, 485, 1559
Prentice, S. J., Ashall, C., James, P. A., et al. 2019b, MNRAS, 485, 1559
Prentice, S. J., Mazzali, P. A., Pian, E., et al. 2016, MNRAS, 458, 2973
Press, W. H., Teukolsky, S. A., Vetterling, W. T.,& Flannery, B. P. 1992, Numerical recipes in FORTRAN. The art of scientific computing
Prieto, J. L., Stanek, K. Z.,& Beacom, J. F. 2008, ApJ, 673, 999
Puls, J., Najarro, F., Sundqvist, J. O.,& Sen, K. 2020, A&A, 642, A172
Rank, D. M., Pinto, P. A., Woosley, S. E., et al. 1988, Nature, 331, 505
Rauscher, T., Heger, A., Hoffman, R. D.,& Woosley, S. E. 2002, ApJ, 576, 323
Rayleigh, L. 1882, Proceedings of the London Mathematical Society, s1-14, 170
Richardson, D., Branch, D.,& Baron, E. 2006, AJ, 131, 2233
Ritter, C., Andrassy, R., Côté, B., et al. 2018, MNRAS, 474, L1
Roberti, L., Pignatari, M., Brinkman, H. E., et al. 2025, arXiv e-prints, arXiv:2504.18867
Rosswog, S., Liebendörfer, M., Thielemann, F.-K., et al. 1999, A&A, 341, 499
Sana, H. 2017, in The Lives and Death-Throes of Massive Stars, ed. J. J. Eldridge, J. C. Bray, L. A. S. McClelland, & L. Xiao, Vol. 329, 110–117
Sana, H., de Mink, S. E., de Koter, A., et al. 2012, Science, 337, 444
Sander, A., Hamann, W. R.,& Todt, H. 2012, A&A, 540, A144
Schlegel, E. M. 1990, MNRAS, 244, 269
Schmidt, B. P., Kirshner, R. P., Eastman, R. G., et al. 1993, Nature, 364, 600

Schneider, F. R. N., Podsiadlowski, P.,& Müller, B. 2021, A&A, 645, A5
Schröder, U., Becker, H. W., Bogaert, G., et al. 1987, Nucl. Phys. A, 467, 240
Schulze, S., Gal-Yam, A., Dessart, L., et al. 2025, Nature, 644, 634
Schuster, A. 1905, ApJ, 21, 1
Schwarzschild, K. 1906, Nachrichten von der Königlichen Gesellschaft der Wissenschaften zu Göttingen. Math.-phys. Klasse, 195, 41
Schweyer, T., Sollerman, J., Jerkstrand, A., et al. 2023, arXiv e-prints, arXiv:2303.14146
Shigeyama, T., Nomoto, K., Tsujimoto, T.,& Hashimoto, M.-A. 1990, ApJ, 361, L23
Shigeyama, T., Suzuki, T., Kumagai, S., et al. 1994, ApJ, 420, 341
Shingles, L. J., Sim, S. A., Kromer, M., et al. 2020, MNRAS, 492, 2029
Shrestha, M., Kwok, L. A., Sand, D. J., et al. 2026, arXiv e-prints, arXiv:2606.28561
Sim, S. A. 2007, MNRAS, 375, 154
Simotas, K., Bildsten, L.,& Prust, L. J. 2025, ApJ, 994, 23
Smith, N. 2014, ARA&A, 52, 487
Smith, N., Li, W., Filippenko, A. V.,& Chornock, R. 2011, MNRAS, 412, 1522
Sobolev, V. V. 1957, Soviet Ast., 1, 678
Spencer, L. V.& Fano, U. 1954, Physical Review, 93, 1172
Spyromilio, J., Meikle, W. P. S., Learner, R. C. M.,& Allen, D. A. 1988, Nature, 334, 327
Stoner, E. 1930, The London, 9, 944
Stritzinger, M., Mazzali, P., Phillips, M. M., et al. 2009, ApJ, 696, 713
Sukhbold, T., Ertl, T., Woosley, S. E., Brown, J. M.,& Janka, H.-T. 2016, ApJ, 821, 38
Taam, R. E.& Sandquist, E. L. 2000, ARA&A, 38, 113
Taddia, F., Sollerman, J., Leloudas, G., et al. 2015, A&A, 574, A60
Taddia, F., Stritzinger, M. D., Bersten, M., et al. 2018, A&A, 609, A136
Taylor, G. 1950, Proceedings of the Royal Society of London Series A, 201, 192
Timmes, F. X., Woosley, S. E.,& Weaver, T. A. 1995, ApJS, 98, 617
Timmes, F. X., Woosley, S. E.,& Weaver, T. A. 1996, ApJ, 457, 834
Tokovinin, A. 2021, Universe, 7, 352
Truran, J. W., Arnett, W. D.,& Cameron, A. G. W. 1967, Canadian Journal of Physics, 45, 2315
Truran, J. W.& Cameron, A. G. W. 1971, Ap&SS, 14, 179
Underhill, A. B. 1962, ApJ, 136, 14
Uomoto, A. 1986, ApJ, 310, L35
Uomoto, A.& Kirshner, R. P. 1985, A&A, 149, L7
Valenti, S., Fraser, M., Benetti, S., et al. 2011, MNRAS, 416, 3138
Valenti, S., Howell, D. A., Stritzinger, M. D., et al. 2016, MNRAS, 459, 3939
van Baal, B. F. A., Jerkstrand, A., Wongwathanarat, A.,& Janka, H.-T. 2023, MNRAS, 523, 954
van Baal, B. F. A., Jerkstrand, A., Wongwathanarat, A.,& Janka, H.-T. 2024, MNRAS, 532, 4106
Van Dyk, S. D., Zheng, W., Fox, O. D., et al. 2014, AJ, 147, 37
Vink, J. S. 2017, A&A, 607, L8
Vink, J. S. 2022, ARA&A, 60, 203
Vink, J. S., de Koter, A.,& Lamers, H. J. G. L. M. 2001, A&A, 369, 574
Vinkó, J., Szalai, T.,& Könyves-Tóth, R. 2023, Universe, 9, 244
Wanajo, S., Hirai, Y.,& Prantzos, N. 2021, MNRAS, 505, 5862
Wang, C.-Y. 2005, ApJ, 626, 183
Wheeler, J. C., Harkness, R. P., Barker, E. S., Cochran, A. L.,& Wills, D. 1987, ApJ, 313, L69
Wheeler, J. C.& Levreault, R. 1985, ApJ, 294, L17
Whitelock, P. A., Catchpole, R. M., Menzies, J. W., et al. 1989, MNRAS, 240, 7P

Wongwathanarat, A., Müller, E.,& Janka, H. T. 2015, A&A, 577, A48
Wooden, D. H., Rank, D. M., Bregman, J. D., et al. 1993, ApJS, 88, 477
Woosley, S. E. 2019, ApJ, 878, 49
Woosley, S. E., Arnett, W. D.,& Clayton, D. D. 1973, ApJS, 26, 231
Woosley, S. E., Eastman, R. G., Weaver, T. A.,& Pinto, P. A. 1994, ApJ, 429, 300
Woosley, S. E.& Heger, A. 2015, ApJ, 810, 34
Woosley, S. E., Heger, A.,& Weaver, T. A. 2002, Reviews of Modern Physics, 74, 1015
Woosley, S. E.& Weaver, T. A. 1988, , 163, 79
Woosley, S. E.& Weaver, T. A. 1995, ApJS, 101, 181
XRISM Collaboration, Marc, A., Awaki, H., Ballhausen, R., et al. 2026, Nature Astronomy, 10, 144
Yaron, O.& Gal-Yam, A. 2012, PASP, 124, 668
Yong, D., Kobayashi, C., Da Costa, G. S., et al. 2021, Nature, 595, 223
Yoon, S.-C. 2017, MNRAS, 470, 3970
Yoon, S.-C., Dessart, L.,& Clocchiatti, A. 2017, ApJ, 840, 10
Yoon, S. C., Woosley, S. E.,& Langer, N. 2010, ApJ, 725, 940
Zapartas, E., Renzo, M., Fragos, T., et al. 2021, A&A, 656, L19
Zwicky, F. 1962, in IAU Symposium, Vol. 15, Problems of Extra-Galactic Research, ed. G. C. McVittie, 347
Zwicky, F. 1964, Annales d'Astrophysique, 27, 300